UNIVERSITÀ DEGLI STUDI DI PARMA

Dottorato di ricerca in Scienza e Tecnologia dei Materiali Innovativi
Ciclo XXVI

Development of Semiconductor Compound Materials & Devices for Radiation Detection Applications

Coordinatore:
Prof. Enrico Dalcanale

Tutor:
Dott. Andrea Zappettini

Dottorando: Giacomo Benassi

Contents

Acknowledgements

First of all I would like to thank to my supervisor Andrea Zappettini for his patience, support, intellectual direction and encouragement throughout my studies.
Thanks also to Nicola Zambelli for his support during the PHD thesis, I have never known a better partner than him.
I would also like to thank the other members of my research group: Dr. Davide Calestani, Dr. Marco Villani, Laura Marchini, Dr. Nicola Coppedè, Massimiliano Zanichelli, Daniele Zanaga, Giovanni Piacentini, Nicola Castagnetti, Maurizio Culiolo, Sathish Chander and Dr. Lucio Zanotti. The research group has been really like a family during this PHD period.
I would also like to thank Dr. Irfan Kuvvetli that was the first person who believed in our capabilities.
Thanks to Tecnopolo for the use of their facilities, in particular for the use "rotating shafts" machine.
I would also like to express my gratitude to all the person of IMEM institute that have shared this time with me: Matteo Bronzoni, Davide Delmonte, Francesco Pattini, Elisa Bonnini, Enzo Rotunno, Stefano Rampino, Marco Negri, Edi Giglioli and Paolo Fedeli.
I would like to thank the following people for the use of their facilities and generous time and effort: Ezio Caroli, Natalia Auricchio, Maura Pavesi, Massimigliano Zannichelli, Enos Gombia, Enzo Rotunno, Laura Lazzarini, Francesco Pattini, Filippo Fabbri.
I would like to thank my parents Anna and Marco, my brothers Pippo and Giovanni and my sister Agnese for their support and encouragement throughout my studies.
Finally thanks to 45 that is still an important part of my life, even if the sky is falling down I know that we'll be safe and sound.

Publications

[I] "Oriented orthorhombic Lead Oxide film grown by vapour phase deposition for X-ray detector applications", G. Benassi, N. Zambelli, M. Villani, D. Calestani, M. Pavesi, A. Zappettini, L. Zanotti, and C. Paorici, **Cryst. Res. Technol. 48, No. 4, 245–250 (2013)**.

[II] "Defect Characterization in Fully Encapsulated CdZnTe", A. Cavallini, B. Fraboni, A. Castaldini, L. Marchini, N. Zambelli, G. Benassi, and A. Zappettini, **IEEE Trans. Nucl. Sci., VOL. 60, NO. 4, (2013)**.

[III] "Electroless gold contact deposition on CdZnTe detectors by scanning pipette technique", N Zambelli, L Marchini, G Benassi, D Calestani, E Caroli and A Zappettini, **JINST 7 P08022, (2012)**.

[IV] "Modification of the Luminescence Properties of CZT Crystals Around Tellurium Inclusions", N. Zambelli, L. Marchini, G. Benassi, D. Calestani, A. Zappettini, **IEEE Trans. Nucl. Sci. , VOL. 59, NO. 4, (2012)**.

[V] "Luminescence properties of CZT crystals in the presence of tellurium inclusions", N. Zambelli, N. Armani, L. Marchini, G. Benassi, D. Calestani, A. Zappettini, **IEEE Nuclear Science Symposium and Medical Imaging Conference (NSS/MIC), (2011)**.

[VI] "Growth and Characterization of CZT Crystals by the Vertical Bridgman Method for X-Ray Detector Applications", Andrea Zappettini, Laura Marchini, Mingzheng Zha, Giacomo Benassi, Nicola Zambelli, Davide Calestani, Lucio Zanotti, Enos Gombia, Roberto Mosca, Massimiliano Zanichelli, Maura Pavesi, Natalia Auricchio, and Ezio Caroli, **IEEE Trans. Nucl. Sci. , VOL. 58, NO. 5, (2011)**.

[VII] "Development status of a CZT spectrometer prototype with 3D spatial resolution for hard x-ray astronomy", N. Auricchio, E. Caroli, A. Basili, G. Benassi, C. Budtz Jørgensen, R. M. Curado da Silva, S. Del Sordo, I. Kuvvetli, L. Milano, F. Moscatelli, J. B. Stephen, M. Zanichelli, A. Zappettini, **Proc. SPIE 8453, High Energy, Optical, and Infrared Detectors for Astronomy V, 84530S, (2012)**.

[VIII] "Luminescence properties of CZT crystals in the presence of tellurium inclusions", N. Zambelli,N. Armani, L. Marchini, G. Benassi, D. Calestani,A. Zappettini , **Proc. Nuclear Science Symposium and Medical Imaging Conference (NSS/ MIC), 4668, (2011)**.

Chapter 1

Introduction

Nowadays radiation detectors are widely used in a large number of application fields: medical imaging, environmental monitoring, homeland security and astrophysics. Several detector technologies based on solid-state materials, due to their intrinsic high stopping power, have been developed during last 60 years. Today, Scintillator and Semiconductor materials represent the main technologies for ionizing radiation detectors. This because scintillator and semiconductor technologies allow the measure of the incident photons energy (with a certain energy resolution) and are, therefore, spectroscopic. Due to the direct conversion of X and gamma photons into electrical signal, semiconductor based detectors can achieve better energy resolutions in comparison with scintillator detectors. Semiconductors exhibit also an excellent mechanical rigidity that allows the fabrication of compact and stable systems. Moreover using semiconductor materials, higher spatial resolution can be achieved in imaging detectors. Due to these unique properties, semiconductors represent the more advance technology for radiation detection of X and γ photons in the energy range 1 KeV–10 MeV.

Semiconductor materials for radiation detection has been developed since 1945 when Van Heerden [1] demonstrated that silver chloride crystals, when cooled to low temperatures, were capable of detect γ-rays, α-particles and β-particles.

The subsequent development was focused on the elemental semiconductors; in particular on Si and Ge. Unfortunately these semiconductors, due to the low band-gap energy, cannot be used at room temperature. This because of the large number of free carriers that are thermally generated at Room Temperature in the material.

These materials required, therefore, expensive and bulky cooling systems that limited the possible applications of these detectors in comparison with scintillator detectors (that can operate at RT). On the contrary Si and, in particular, Ge based detectors can achieve the highest energy resolution at cryogenic temperatures.

To overcome this intrinsic limit of Si and Ge, compound semiconductors with high band-gap energy were proposed for room temperature applications. Therefore wide band-gap semiconductor can be obtained offering the ability to operate in a wide range of thermal and radiation environments, whilst still maintaining sub-keV spectral resolution at high X and gamma photons energy.

During last 40 years several compound semiconductors have been proposed for room temper-

ature radiation detectors and strong efforts have been done in order to increase the quality of these materials. In addition to the band gap value other properties are required for radiation detectors: high effective atomic number and high density to provide sufficient stopping power, high resistivity, good transport properties of carriers and good material uniformity in order to achieve spatial and spectral response. Some of the compound semiconductor materials which fulfil some of these requirements are: GaAs, CdZnTe, CdTe, HgI2, PbI2, TlBr and PbO[2] .
In general a "magic material" which fulfils perfectly all the properties required for radiation detection applications does not exist. Therefore, for each specific application, some materials can be more performing than another, depending on the properties required. For this reason the research in these compound semiconductors is still on going.
In particular this work was focused on two compound semiconductors: PbO that represents a new and not well-explored material and, CdZnTe that represents almost a standard material for radiation detectors. For this reason with CZT material nowadays high performance detectors with high spatial and energetic resolutions can be fabricated.

This thesis includes some efforts and results, reached at IMEM-CNR during the last three years, on both materials and devices for radiation detection applications.

- The first part of the thesis treats some basic concept of radiation detection. In particular the radiation concept, interactions radiation-matter and some medical applications of radiation are introduced in Chapter 2. The physics of semiconductor radiation detectors is presented in Chapter 3.

- The second part of the thesis treats the research on a new material: PbO. In particular Chapter 4 presents the growth of polycrystalline and single crystal samples of β-PbO performed at IMEM-CNR using vapour approach. The samples were characterized with several techniques including: Photoluminescence, I-V characteristic, X-ray diffraction, TEM diffraction and Spectral Photoconductivity. This chapter presents also a diagnostic technique based on X-ray induce current developed at IMEM-CNR by the author of this thesis. By means of the described technique it was possible to measure the transport properties on PbO and CZT samples. All measurements, sample preparation, instrumentation development and data analysis was carried out at IMEM institute by the undersigned except for the TEM diffraction that was carried out at IMEM by Dott. L. Lazzarini and E. Rotunno and the Spectral Photoconductivity that was carried out at Physics Department of Parma by the undersigned.

- In the third part of the work the research on CZT detectors is presented. The first part Chapter 5 treats the preparation and characterization of CZT detector fabricated using the material grown at IMEM-CNR institute. This part describes all the detector fabrication processes carried out at IMEM by undersigned, these processes include: Cutting, polishing, contact deposition and passivation. The undersigned was also involved in some parts of the

growth of CZT ingots. The quality of CZT detectors can be evaluated by means of some characterizations including: I-V characteristic, resistivity measurement, transport properties measurement and spectroscopic performance. These characterizations are important in order to evaluate the quality of CZT material and the quality of the detector preparation process. All these detector fabrication steps and characterizations were carried out at IMEM institute by the undersigned except for the spectroscopic measurements that were carried out by the undersigned at INAF-IASF institute of Bologna under the supervision of Dott. E. Caroli. The transport properties measurements with alpha particles were carried out at the Physics department of Parma by the undersigned. The PICTS measurements were carried out at University of Bologna by proff.ssa A. Cavallini using samples prepared by the undersigned. The last part of the chapter 5 encloses the results reached in the preparation and characterization of four CZT detectors developed in range of "3D CZT High Resolution Detectors" project leaded by Doc. Carl Budtz-Jorgensen and Doc. Irfan Kuvvetli, from National Space Institute of Technical University of Denmark (DTU Space Center). The aim of this project was to demonstrate that the good energy resolution of a new CZT drift strips detector can be combined with 3D sensing capabilities, very important features for X and gamma ray detectors for high energy astrophysics missions. IMEM institute was involved in some important parts of the project such as detector preparation, detector characterization and data analysis. This part presents all the steps of detector fabrication process and all the developments that were done in all single step of detectors preparation. For this project a new passivation process was developed at IMEM by the undersigned in collaboration with F. Pattini. In the final part of the Chapter 5 the detector characterization performed at European Synchrotron Radiation Facility (ESRF) in Grenoble is presented. All the detector preparation processes were carried out in IMEM by the author of this thesis in collaboration with Nicola Zambelli.

Part I

Basic Concepts of Radiation Detectors

Chapter 2

Radiation

2.1 Introduction

The concept of radiation, the interactions radiation-matter and some medical applications of radiation will be discussed in this chapter. These concepts are treated in many excellent textbooks[3] to which the reader is referred. These concepts are very important in order to understand how a radiation detector works and which materials are more interesting than other for radiation detector applications. Also some use of radiation in medical applications will be described at the end of this chapter. Medical uses of radiation is one of the most important application filed for radiation detector and, therefore, it is important to understand which types of radiation and energy are involved in these applications.

2.2 Radiation

Radiation is a physical process in which energy travels through vacuum or media in the form of energetic particles (beta particles, alpha particles, protons or neutrons) or as electromagnetic waves (ultraviolet light, visible light, microwaves, X and γ rays..). The Radiation can be classified in two types according to the energy involved in the process:

1. **Ionizing radiation** is the radiation that, due to the interaction with matter, can remove tightly bound electrons from the atomic shells. The result of the interaction is a ionized atom and a free electron. Ionizing radiation includes beta particles, protons, alpha particles, gamma rays, X-rays and neutrons.

2. **Non-ionizing radiation** is the radiation whose energy is not enough to ionize atoms and includes radio waves, microwaves, infrared and visible light.

The word "radiation" is often colloquially used in reference to ionizing radiation and also in this thesis this definition of radiation will be used. Radiation detectors are, therefore, devices that can detect this radiation. Not all ionizing radiations will be discussed in this work, the further discussion will be focused only on α-particles, X and γ rays.
The alpha particles are a charge heavy particles that are emitted from nuclei due to nuclear instability. Alpha particle is constituted by 2 protons and two neutrons like the nucleus of

the He and represents the largest and most massive type of radiation. The important feature of this particles, from detector characterization point of view, is the mono energetic behavior. Alpha particles have a characteristic value of energy in the range $4 \div 6$ MeV according to the radionuclide.
X and γ rays are both electromagnetic radiations with a wavelength in the range from 10 to 0.1 pm and energies in the range few KeV to thousands of MeV. The only difference between X and γ rays is the origin of the radiation itself. X-rays are originated by moving electrons or by electrons in the atomic shells (X-ray tube, Synchrotron), gamma rays are originated from the unstable nuclei. For this reason X-rays are characterized by a wide range of energy and γ rays have only specific values of energy according to the decay chain of the radionuclide. As will be discussed later also the X-rays generated in the atomic shells (called characteristic x-ray) have a well defined characteristic energy and they can be used to identify the chemical composition of a material.

2.3 Interaction of Alpha Particles with Matter

Alpha particles are heavy positive charge particles and therefore they inter- act primarily with the atomic bounded electrons through Coulomb forces. The interaction with nuclei is also possible but it occurs rarely and the interactions with electrons remain the significant contribution in the response of the detector. The maximum energy that can be transferred to an electron during the collision is proportional to the ratio between the mass of the alpha particle and the electron mass. Due to the low value of the latter (1/500 of the particle energy) alpha particle can interact with a large number of electrons, decreasing its velocity continuously, until it is stopped. The energy transferred may be sufficient to raise the target electrons in a higher energy shell (excitation process) or to remove completely electrons from the atom (ionization process). The linear stopping power for alpha particle S in a medium is defined as the rate of differential energy loss per unit path length:

$$S = -\frac{dE_\alpha}{dx} \rightarrow -\frac{dE_\alpha}{dx} = \frac{4\pi e^4 z^2}{m_0 v^2} NB \tag{2.1}$$

The second part of the formula 2.1 is called "Bethe" formula and is the classical expression to calculate the linear stopping power for a charged particle (with charge ze , velocity v) in a medium. N is the density of the absorber and B is a coefficient that depends on the atomic number of the absorber and on velocity of the charged particle. In general, due to the strong interaction with matter, the mean free path of the alpha particles in high density matter is very low (a few micrometers in solids).

2.4 Interaction of X and γ Rays with Matter

X and γ rays are both constituted by photons and, therefore, they interact with the matter in the same identical way. Due to the zero mass and neutral charge of the photons the interaction can be considered weaker in comparison with charged particles-matter interactions. Therefore X and

γ rays can travel a considerable distance inside the matter before interacting and the absorption becomes a process that involve the volume of the material. Due to interactions radiation-matter the intensity of beam of X and γ photons that pass through an absorbing medium will be attenuated. This attenuation follows an exponential attenuation law (Beer's law):

$$I = I_0 exp^{-\delta x} \tag{2.2}$$

where I_0 is the intensity of a incident mono-energetic γ-ray beam and I is the intensity of transmitted beam.
The linear attenuation coefficient δ, as will be discussed later in details, depends on the gamma-ray energy, the atomic number(s) and the density of the absorber medium.
Another important quantity is the mean free path λ that represents the average distance traveled inside the medium by the radiation:

$$\lambda = \frac{\int_0^\infty x exp^{-\mu x} dx}{\int_0^\infty exp^{-\mu x} dx} = \frac{1}{\mu} \tag{2.3}$$

With the mean free path it is possible to calculate the interaction volume of the absorbing material and calculate, for example, the theoretical efficiency of the detector.
Sometimes it is convenient to use the mass attenuation coefficient μ/ρ that is independent of the density of the material. This quantity is useful when the relation between attenuation and atomic number is compared for different absorbing materials. The value of μ/ρ is directly related with the total cross-section σ_T calculated for single atom:

$$\mu/\rho = \sigma_T \frac{N_A}{uA} \tag{2.4}$$

where N_A is the Avogadro number, u is the atomic mass unit and A is the relative atomic mass of the absorbing material. The total cross-section can be written as sum over contributions of the principal radiation-matter interactions: Photoelectric effect, Compton scattering and Pair Production.

$$\sigma_T = \sigma_{photoelectric} + \sigma_{Compton} + \sigma_{pair} \tag{2.5}$$

Each cross-section depends on photons energy and absorbing material in a different way. All these interactions are competitive processes: depending on the energy of the photon one interaction can be more probable than another. In the further discussion all these interactions will be described in details and in particular a relation between cross section and atomic number will be formulated. This relation is important for simulating the response of the detector and for selecting an efficient absorbing material.

2.4.1 Rayleight Scattering

This interaction is not considered in the linear attenuation coefficient because no energy is deposited inside the material in this elastic scattering. In this process only the path of the photon is deflected by an angle that depends on the energy of the photon and the atomic number of

the material. No energy is deposited inside the material and no signal is collected due to this interaction in the detector. For this reason this effect will not be considered in the thesis.

2.4.2 Photoelectric Absorption

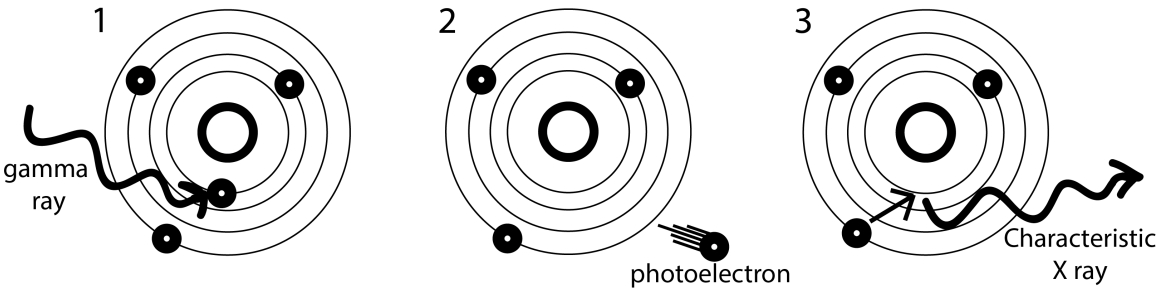

Figure 2.1: *Photoelectric interaction. 1) γ ray interacts with one electron of the atomic shell, 2) the photon disappears and high energy photoelectron is emitted, 3) the vacancy is filled by outer electron and characteristic X-ray is emitted*

In the photoelectric interaction the energy of the incident gamma photon ($E_\gamma = h\nu$) is totally absorbed by one atom and the incident photon disappears. The absorbing atom remains in a unstable state and it will reach the equilibrium ejecting one shell electron (normally from K shell). This ejected electron, called "photoelectron", will have a nonzero kinetic (E_e) energy due to the conservation of total energy:

$$E_e = h\nu - E_b \tag{2.6}$$

E_b is the binding energy of the electron and depends on the type of atomic shell. This ejection process creates an ionized atom with a vacancy that will be quickly filled through the capture of free electron or, more probable, filled by an outer shell electron. In the second case the rearrangement will produce also a secondary particle: characteristic X-ray photon or an electron with a characteristic energy (Auger emission). As shown in fig.2.2 in high Z materials (typically used

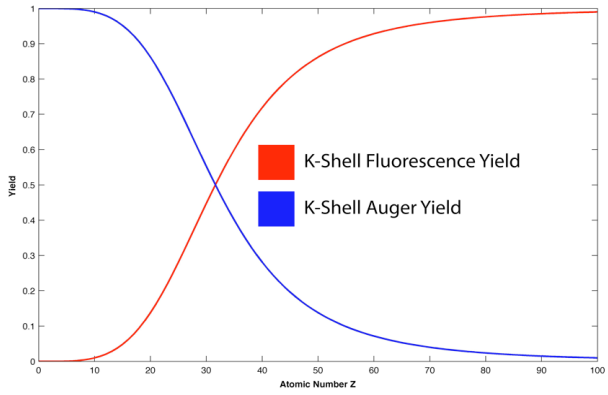

Figure 2.2: *Auger and X-ray yield for K shell as function of the atomic number Z*

in radiation detection) the characteristic X-ray emission is more probable than Auger emission.

In general the photoelectric effect produces two entities that will interact with matter: one high energetic photoelectron and one characteristic X photon. The photoelectron, after ejection, will lose all kinetic energy via coulomb interactions with the absorbing medium (in the same way of alpha particles). These collisions will create high number of free carriers inside the material due to the ionization of the atoms. For the characteristic X photon the possibilities are different: it can escape from the material and it can be absorbed via photoelectric interaction. Only in the case that also the characteristic X-photon energy is totally absorbed, all the energy of the incident gamma photon is deposited in the material. But, due to the low energy of these secondary radiations, most of the time the characteristic X-photons are also absorbed in the material. The Photoelectric is therefore the ideal absorption process for a detector because all the energy of the incident gamma photon is deposited in the material. The photoelectron cross-section can be expressed as function of the atomic number of the absorbing material and the energy of the incident photon:

$$\sigma_{photoelectric} \simeq A \cdot \frac{Z^n}{E_\gamma^{3.5}} \tag{2.7}$$

Where A is a constant and the exponent n can vary between 4 and 5. At low incident photon energy and at high atomic number the Photoelectric effect is the dominant absorption process.

2.4.3 Compton Scattering

Compton scattering involves one incident gamma photon and one electron of the atomic shells. In this scattering the gamma photon is deflected trough at an angle θ with respect to its original direction losing part of its energy that is transferred to the recoil electron. The amount of this energy depends on the deflection angle and it can vary from zero to a large fraction of the gamma-ray energy. The kinetic energy of the electron can be calculated using the conservation energy relation:

$$E_e = E_\gamma - E' \tag{2.8}$$

where E_e is the value of energy of the recoil electron, E_γ the value of energy of the incident photon. E' is the energy of the scattered gamma photon and it can be calculated with:

$$E' = \frac{E_\gamma}{1 + \frac{E_\gamma}{m_0 c^2}(1 - cos\theta)} \tag{2.9}$$

θ is the scattering angle and m_0c^2 (0.511 MeV) the rest-mass energy of electron. For $\theta = 0$, $E' = E_\gamma$ and no energy is transferred to electron. On the contrary E_e becomes maximum when $\theta = \pi$:

$$E_e = E_\gamma - \frac{E_\gamma}{1 + \frac{E_\gamma}{m_o c^2}} \tag{2.10}$$

After the scattering process, the recoil electron will deposit its energy to the absorbing material via coulomb interactions. Also the scattered photon will interact with the material (via photoelectric or Compton) or it will escape without interactions. It is important to note that in the Compton scattering only a fraction of the incident gamma photon energy is deposited in the medium also at $\theta = \pi$. Only in the case that also the scattered photon is absorbed by the

material the energy of the incident photon can be traced back but this is normally difficult due to the high energy of the scattered photon.
The differential Compton cross-section is described, for single free electron, by the Klein-Nishina equation:

$$\frac{d\sigma_{KN}}{d\Omega} = \frac{r_0^2}{2}\left(\frac{E'}{E_\gamma}\right)^2\left(\frac{E'}{E_\gamma} + \frac{E_\gamma}{E'} - sen^2\theta\right) \tag{2.11}$$

where $r_0 = 2,8{\cdot}10^{-15}m$ is the classic radius of electron. The polar plot of differential cross-section

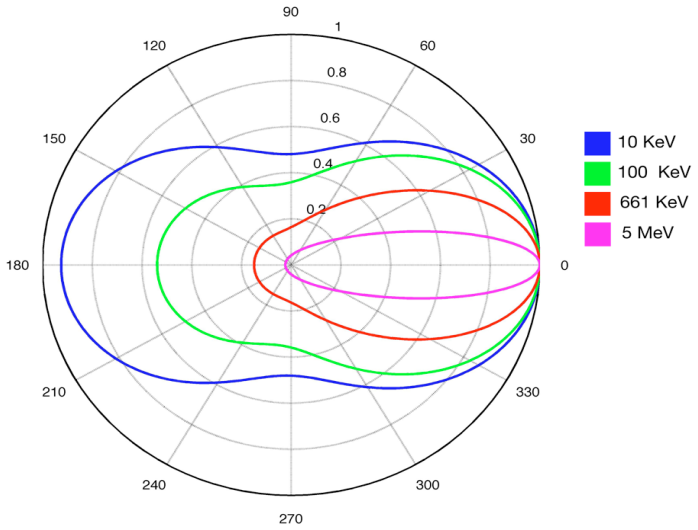

Figure 2.3: *Polar plot of the differential Klein-Nishina cross-section for different energies*

for different energies is shown in fig 2.3. As the photon energy increases, and eventually becomes comparable with the rest mass energy of the particle, the Klein-Nishina formula predicts that forward scattering of photons becomes increasingly favored with respect to backward scattering. Integrating the 2.11 over all solid angle $d\Omega$, it is possible also to obtain the Compton total cross-section :

$$\sigma_e = 2\pi r_0^2\left\{\frac{1+\epsilon}{\epsilon}\left[\frac{2+2\epsilon}{1+2\epsilon} - \frac{ln(1+2\epsilon)}{\epsilon}\right] + \frac{ln(1+2\epsilon)}{2\epsilon} - \frac{1+3\epsilon}{(1+2\epsilon)^2}\right\} \tag{2.12}$$

$\epsilon = {}^{E_\gamma}/_{m_0c^2}$. The total cross-section for a single electron depends only on the photon energy and it is independent on the atomic number, this because the cross section is calculated considering a single free electron. If also the number of electrons is considered the total cross-section for one atom can be expressed:

$$\sigma_{Compton} = Z\sigma_e \tag{2.13}$$

The total Compton cross-section is proportional to the number of electrons in the absorbing medium so it is proportional to the atomic number Z.

2.4.4 Pair Production

If a gamma photon with energy larger than 1.022 MeV passes near the nucleus it can generate a positron and electron pair. This process is a simple conversion energy/mass and is called pair production and no excitation of the nucleus is present in this interaction. If the energy of the incident photon exceeds the creation energy (1.02 MeV) this excess will be converted in kinetic energy equally shared between the electron and positron:

$$E_{e^+} = E_{e^-} = \frac{E_\gamma - 1.022}{2} \tag{2.14}$$

E_{e^+} and E_{e^-} are the kinetic energies of electron and positron respectively and E_γ is the energy of the incident photon. Afterwards the positron will annihilate with an electron producing two photons of identical energy 511 KeV (rest mass of electron). As discussed before the electron will lose the kinetic energy via Coulomb interactions with matter. On the contrary, for the two generated photons, the probability of absorption is low due the high energy. The pair production cross section function of the atomic number can be approximated as:

$$\sigma_{pair} \propto Z^2 \tag{2.15}$$

In general the pair production is the dominant process at high photon energies as shown in fig.2.4.

2.4.5 Total Cross-Section

As discussed before all the interaction processes contribute to the total absorption coefficient of the material. The cross-sections of single processes are photon energy and Z dependent. As shown in fig.2.4 the photoelectric absorption is the dominant mechanism in the low energy range while the pair production is dominant at high energy ($>$ several MeV). Finally it is important to consider that in the low energy range the materials show different absorption peaks in correspondence to the atomic shell energies. As shown in fig.2.4 and fig.2.5 this effect can produce an enhance of the absorption, in some cases, by factor a 10 that must be taken into account.

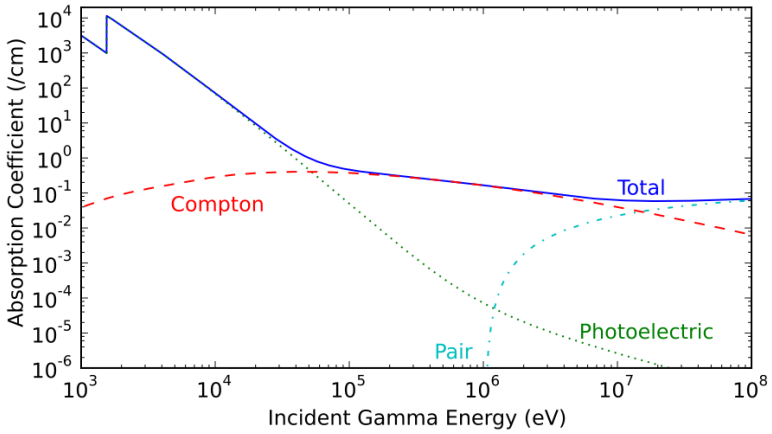

Figure 2.4: *Plot of the gamma macroscopic total cross section of Aluminum Z=13 as function of gamma energy.*[4]

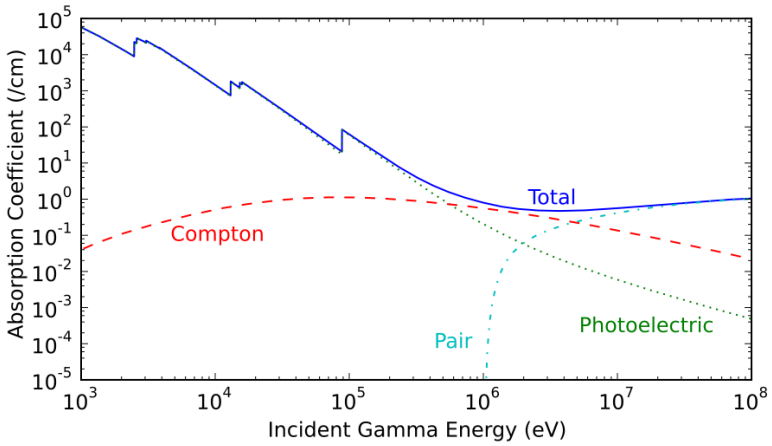

Figure 2.5: *Plot of the gamma macroscopic total cross section of Lead Z=82 as function of gamma energy.*[4]

2.5 Medical Uses of Radiation

Ionizing radiations have different uses in medical applications and it is useful to separate two types of use: diagnosis and therapy. Both of them are intended to benefit the patients compared to the damage that they can cause. This is the general principle "justification of a practice" used in radiological protection and it can be applied for all types of medical and industrial applications. The main difference in these two type of applications is the amount of energy deposited inside the patients that is called "dose". For diagnosis the radiation is used to collect information about the body of the patient and, therefore, low dose is required. On the contrary much higher dose is required for therapy to treat malignant diseases or malfunctioning organs. From the point of view of radiation detectors the most interesting medical use is diagnosis.

With diagnostic radiology is called the technique where a X-ray beam is used for examining the patient: it was the first medical use of X-ray and it was discovered by Röntgen. X rays penetrate flesh and bone in a different way due to their different chemical composition and density. These differences in the attenuation of the beam are collected by a film or a flat panel detector producing images of the internal structure of the body. In conventional X-ray examination only single parts of the body are examined (most frequently chest, limbs and teeth) and 2D images are collected by the projection of the body part to the plane of the film (or flat panel detector). To overcome this limitation Computer Tomography (CT) was proposed. In this technique a fan-shaped beam of X-rays is rotated around the patient and registered on the opposite side by a row of detectors. In this way it is possible to collect the image of a slice or section of the body. Than all the sections are meshed together by a computer reconstructing all the patient body in 3 dimensions.
The use of pharmaceuticals labelled with radionuclides for diagnosis instead of X-rays is called nuclear medicine. In these techniques there is not a beam that passes through the body but the radiations are generated inside the body by radionuclides. These substances, that are administrated by injection, ingestion or inhalation, are designed to be preferentially taken up by the tissue or organ of interest. The diagnostic technique using radionuclides is called Emission Tomography (ET) and that can be divided in two main techniques: the Single Photon Emission Computed Tomography (SPECT) and the Positron Emission Tomography (PET). SPECT technique use radiopharmaceuticals labeled with a single-photon emitter, a radioisotope that emits one gamma-ray photon each radioactive decay event as shown in table 2.1. In the PET technique the radionuclide decays emitting a positron that, annihilating with one electron, produces 2 photons of 511 KeV moving in opposite directions. Collecting the two photons with a ring-shape

Type of technique	Source of radiation	type of radiation	energy (KeV)
Mammography	X-ray tube	X photons	17÷25
Radiography	X-ray tube	X photons	40÷60
CT	X-ray tube	X photons	60÷70
SPECT			
	Technetium-99m	gamma photon	140
	Iodine-131	gamma photon	159
	Indium-111	gamma photon	171 or 245
PET			
	FDG (Fluorine-18)	2 gamma photons	511

Table 2.1: *Ionizing radiations used for diagnostic medical applications.*

detector and measuring the difference in the two times of flight, it is possible to reconstruct the position of the emitting radionuclide inside the body.
The medical uses of radiation are very important for diagnosis, in particular both X and γ-rays can be used. As shown in table2.1 X-ray typical energies are in the range $10 \div 100$ KeV, gamma rays are in the range $100 \div 511$ KeV.

Chapter 3

Semiconductor Radiation Detectors

3.1 Introduction

Nowadays several technologies to detect ionizing radiation (in particular X and γ rays) are available. In general two families of detector can be distinguished:

1. **Spectroscopic detectors**. All the energy deposited by X and γ photons is converted into electrical signal that is directly proportional to the energy deposited by photons. Measuring these signals it is possible to reconstruct the energy of the gamma photon.

2. **Non Spectroscopic detectors**. In these types of detector all information of the energy of the photons is lost. With these technologies it is possible only to measure the count rate of the incident photons.

Due to their intrinsic advantages, the first class of detector represent a more interesting technology for radiation detection. Therefore the further discussion will be focused only on the first class of detectors.

3.2 Spectroscopic Detector Technologies

In chapter 2 all the possible gamma interactions with matter are discussed. As a consequence of these interactions, energy is released inside the detector. In order to reconstruct the "true" energy of incident photons, it is very important that all the photon energy is deposited inside the detection volume. Only in this case the amplitude of the signal is directly proportional to the incident photon energy.
In principle this can be achieved using a detector with a volume large enough to absorb every secondary products of interaction (like Compton scattered photons, photoelectrons, characteristic X-rays and annihilation photons). In the real case of a detector with finite dimensions (limited also by technological issues) this condition is not always respected and therefore it is impossible to collect all the secondary products (also because of the high mean free path of the high energy photons). In order to reduce this loss of energy it is important to increase the Photoelectric interaction probability with respect to Compton scattering and pair production probabilities. This because the characteristic X-rays and photoelectrons have high probability to be absorbed

inside the detector due to the short mean free path (that is in the range $50 \div 100$ μm).
Reassuming, a good spectroscopic X-rays and γ-rays detector must carry out some rules:

- It must have a reasonable high Photoelectric interaction probability.
- It must be an efficient detector for secondary electrons and characteristic X-rays.
- Electrodes must collect all the generated carriers.

These conditions are satisfied only considering the following properties of the absorbing material:

- The stopping power is proportional to the density of the material. For this reason the most attractive technologies are based on solid state absorbing media (scintillators and semiconductors) instead of gas or liquid based detectors.
- The atomic number of the atoms inside the material should be as large as possible in order to increase the photoelectric absorption probability ($\sigma_{photoelectric} \propto Z^5$, $\sigma_{Compton} \propto Z$ and $\sigma_{pair} \propto Z^2$).
- The transport properties of the material must be good enough to allow the collection of the generated carriers in a reasonable time.

3.2.1 Scintillators

Scintillators are materials that produce sparks of light when ionizing radiations interact with them. The amount of light produced by the interaction with photons is proportional to the energy deposited inside the scintillator. This because when a ionizing radiation passes thought the crystal and interacts with it, several electron-hole pairs are created with a number proportional to the energy deposited. These carriers can recombine via emission of a photon in the UV-visible part of the electromagnetic spectrum. These recombination processes are assisted by activation centres (impurity atoms in the crystal) that create energy levels inside the band-gap close to the valence and conduction bands. By capturing electrons, holes and excitons (electron-hole bounded system) generated by the ionizing radiation these levels can be excited. The transition of the impurity atoms to the ground state (de-exitation) results in emission of a photon in the UV-visible range in a very short time ($10^{-8}\ s$). The light emitted by a scintillator is primarily due to the impurity atoms. This means that only a part of the deposited energy is converted into light and the scintillator efficiency depends on the number of activator centres inside the material.
The light generated can be converted into electrical signal by a photomultiplier tube or a photodiode directly coupled with the scintillator crystal. Typical scintillators materials are: NaI, CsI, Gd_2O_2S, $Bi_4Ge_3O_{12}$ (BGO), Lu_2SiO_5 (LSO) and BaF_2[5][6]. The main disadvantages of this technology are the low efficiency (limited by the number of impurity centres) and also the low energy resolution. The two-step conversion process of the gamma photon energy limits this energy resolution. Moreover the emission of light is not directional and this decreases both the efficiency and the spatial resolution that it is possible to achieve in the imaging detectors based on scintillator.

3.2.2 Semiconductors

Semiconductors are very attractive materials for detectors and nowadays are widely used in a large number of application fields. From the point of view of radiation detection the main advantage of this class of material is the so called "one-step" generation of carriers. Unlike scintillators, in semiconductors the energy deposited by photons is directly converted into free carriers (electron-hole pairs) without any other intermediate mechanisms (for example light generation). This intrinsic property of semiconductor materials offers the possibility to achieve higher energy resolution than scintillator detectors. Moreover semiconductors have other interesting properties that can be summarized as:

1. Semiconductors are high density materials (at least with respect to gas) with an excellent mechanical rigidity: this allows the fabrication of compact and stable systems.

2. By doping it is possible to modify the properties of the semiconductor obtaining a material with very few free carriers (resistivity $> 10^7 \Omega cm$).

3. The choice of the proper compound allows optimizing the energy gap value and, therefore, the energy for creating electron-hole pairs (ϵ_i ionizing en- ergy) as well intrinsic carrier concentration.

4. Several high quality semiconductors based on high-Z atoms are available today on the market.

5. Electrons and holes can move almost freely inside the semiconductor.

6. Semiconductor technology allows the fabrication of imaging detectors with high spatial resolution. This resolution is limited only by interaction volume of the incident photon with detector and by the process used for deposing electrodes.

Tuning these properties two different classes of semiconductor detectors can be fabricated:

- **High Energy Resolution Detectors**. Decreasing the band-gap energy it is possible to achieve very high-energy resolution due to the reduction in ionizing energy (as will be discussed later). Moreover lower band-gap energy ($< 1.4\, eV$) means higher thermally generated carrier density. The result is that for these detectors is necessary to operate at cryogenic temperature. The typical material used for these applications are Ge ($0.67\, eV$) and Si ($1.2\, eV$), Ge detectors in particular requires liquid nitrogen cooling system.

- **Room Temperature Detectors**. These detectors are based on semiconductor with band-gap energy $> 1.4\, eV$: GaAs (1.42 eV), CdTe (1.52 eV), CdZnTe (1.57 eV), TlBr (2.68 eV), PbI2 (2.32 eV), HgI2 (2.15 eV), AlSb (1.6 eV) and AlN (with 6,8 eV bang gap this compound is also solar blind). Due to the possibility to operate at room temperature, reducing the cost and the size of the detector system, these materials are now very attractive for radiation detection applications. Despite this, the energy resolution of these detectors is less compared with Ge and Si based detectors.

The most important physical properties of semiconductor materials for radiation detection are summarized in table of fig.3.1.

Parameter	Si	4H-SiC	InP	GaAs	Ge	$Cd_{0.35}Mn_{0.55}Te$	$Cd_{0.7}Zn_{0.3}Se$
Density ($g\,cm^{-3}$)	2.33	3.21	4.78	5.32	5.33	5.8	5.5
Average atomic number(s)	14	10	32	31.5	32	49	38
Band gap (eV)	1.12	3.26	1.35	1.43	0.67	1.73	2.0
Pair creation energy (eV)	3.62	7.8	4.2	4.2	2.96	2.12	6.0
Electron mobility ($cm^2\,V^{-1}\,s$)	1400	1000	4600	8000	3900		
Hole mobility ($cm^2\,V^{-1}\,s$)	1900	115	150	400	1900		10
Electron lifetime (s)	$>10^{-3}$	5×10^{-7}	1.5×10^{-9}	10^{-8}	$>10^{-3}$		
Hole lifetime (s)	10^{-3}	7×10^{-7}	$<10^{-7}$	10^{-7}	2×10^{-3}	10^{-7}	10^{-7}
Electron $\mu\tau$ product ($cm^2\,V^{-1}$)	>1	4×10^{-4}	5×10^{-6}	8×10^{-5}	>1	$>10^{-6}$	$\sim10^{-4}$
Hole $\mu\tau$ product ($cm^2\,V^{-1}$)	~1	8×10^{-5}	$<1.5\times10^{-5}$	4×10^{-6}	>1		10^{-6}
Crystal structure	Cubic	Hexagonal	Cubic (ZB)	Cubic (ZB)	Cubic	Hexagonal	Hexagonal
Lattice constant (Å)	5.43095	3.079 (a) 5.048 (c)	5.8686	5.6533	5.64613		
Knoop hardness ($kg\,mm^{-2}$)	1150	2540	460	750	692		
Melting point (°C)	1412	2827	1060	1238	958	1080	1320
Dielectric constant	11.7	9.7	12.4	12.8	16		
Resistivity (Ω/cm)	$<10^4$	$>10^5$	10^6	10^7	50	10^{10}	10^{10}
$1/e$ abs. Depth (mm) at 10 keV	0.127	0.128	0.020	0.051	0.050	0.019	0.019
at 100 keV	23.30	17.90	1.597	3.46	3.51	1.5	1.5
Typ. FWHM ΔE (keV) at 60 keV	0.4	2.7	12	0.7	0.3	21	1.8
Intrinsic. FWHM ΔE (keV) at 60 keV (Fano noise)	0.415	0.642	0.443	0.439	0.250	0.530	0.530
Typical thickness (mm)	0.3	0.3	0.2	0.2	20	0.5	0.1

Parameter	$Cd_{0.9}Zn_{0.1}Te$	CdSe	CdTe	PbI_2	HgI_2	TlBr
Density ($g\,cm^{-3}$)	5.78	5.81	5.85	6.2	6.4	7.56
Average atomic number(s)	49.1	41	50	63	62	58
Band gap (eV)	1.572	1.73	1.44	2.32	2.15	2.68
Pair creation energy (eV)	4.64	5.5	4.43	4.9	4.2	6.5
Electron mobility ($cm^2\,V^{-1}\,s$)	1000	840	1100	8	100	30
Hole mobility ($cm^2\,V^{-1}\,s$)	120	75	100	2	4	4
Electron lifetime (s)	3×10^{-6}	10^{-7}	3×10^{-6}	10^{-6}	3×10^{-6}	2.5×10^{-6}
Hole lifetime (s)	1×10^{-6}	10^{-6}	2×10^{-6}	3×10^{-7}	1×10^{-5}	3.7×10^{-5}
Electron $\mu\tau$ product ($cm^2\,V^{-1}$)	4×10^{-3}	6.3×10^{-5}	3×10^{-3}	1×10^{-5}	3×10^{-4}	5×10^{-4}
Hole $\mu\tau$ product ($cm^2\,V^{-1}$)	1.2×10^{-4}	7.5×10^{-5}	2×10^{-4}	3×10^{-7}	4×10^{-5}	2×10^{-6}
Crystal structure	Cubic (ZB)	Wurtzite	Cubic (ZB)	Hexagonal	Tetragonal	Cubic (CsCl)
Lattice constant (Å)		4.2999 (a) 7.0109 (c)	6.48		4.37 (a) 12.44 (c)	3.47
Knoop hardness ($kg\,mm^{-2}$)	?	90–130	60	<10	<10	12
Melting point (°C)	1092–1295	1239	1092	408	259	460
Dielectric constant	10	10.2	10.9		8.8	29.8
Resistivity (Ω/cm)	3×10^{10}	10^9	10^9	10^{13}	10^{13}	10^{12}
$1/e$ abs. Depth (mm) at 10 keV	0.011	0.019	0.011	0.011	0.011	0.011
at 100 keV	1.01	1.5	1.01	0.453	0.46	0.32
Typ. FWHM ΔE (keV) at 60 keV	1.5	8.5	1.1	1.83	3.5	7.9
Intrinsic. FWHM ΔE (keV) at 60 keV (Fano noise)	0.393	0.506	0.300	0.441	0.409	0.550
Typical thickness (mm)	2	0.5	2	0.1	10	1

Figure 3.1: *Comparison of properties of different semiconductor materials used for radiation detection* [2]

3.3 Physics of Semiconductor Radiation Detectors

In the following section the physical process of signal creation inside semiconductor detectors will be discussed, this part is well treated in the textbook of Gerhard Lutz [8]. As discussed in chapter 2, the X and γ photons can interact with matter deposing all or a part of their energy. In semiconductor materials this energy is able to ionize the solid creating a large number of electron-hole pairs (depending on the ϵ_i). These carriers during the drift inside the detector will induce signal to the electrodes and a readout electronic chain will collect this signal.

3.3.1 Generation of Charge Carriers

In semi-insulating semiconductors (high resistivity materials) the density of free carriers is low enough to allow the detection of carriers generated by X and γ photons even at low photon energies. The energy for creating free carriers ϵ_i is called ionizing energy and represents the mean energy for creating one electron-hole pair. It is directly proportional to the band gap value E_g following the Klein law[9] and, in the first approximation, it can be considered as: $\epsilon_i \simeq 3E_g$. According to this law the number of electron-hole pairs can be expressed as ratio between the incident photon energy and ϵ_i:

$$N \propto \frac{E_0}{\epsilon_i} \tag{3.1}$$

This ionizing energy is very small compared with the typical energy deposited in the material by a X and γ photons. This means that each photons can ionizing a large number of electron-hole pairs creating a "cloud of charge" inside the detector.

3.3.2 Charge Collection and Measurement

At this point it is useful to describe the structure of a semiconductor detector. The simplest detector (also called "planar detector") consist of a slab of semiconductor material (with the properties described in the previous section) with two metal layers deposited on two opposite surfaces in contact with the semiconductor (the role of contacts will be discussed later). To bias the device a voltage difference is maintained across the two surfaces for example one is connected to ground an the other is connected to a positive pole of a dc power supply.

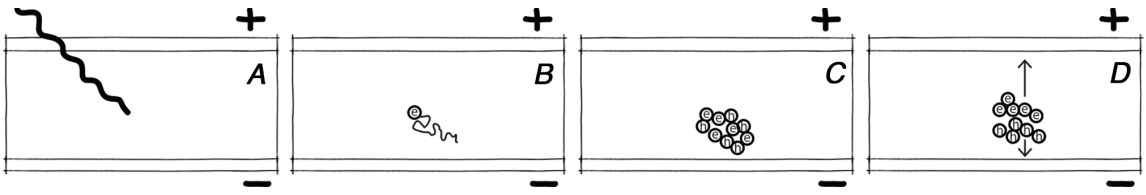

Figure 3.2: *Signal creation steps: A) photon interact with the detector, B) the photoelectron generated loses its energy by collision with lattice, C) cloud of electron-hole pairs is created, D) the carriers are separated by the applied bias and start to drift to the electrodes.*

Now suppose an incident gamma photon interacts with one atom of the detector (fig. 3.2 A). If the photon interacts via Photoelectric process, one high energetic electron will escape from the atom and, colliding with the lattice (fig. 3.2 B) it will create a large number of electron-hole pairs

(fig. 3.2 C). The γ-ray interactions produce electrons and hole whose distribution is elongated along the path of the photoelectron. These distributions are called "clouds" of charge. The e-h pairs will be separated by the applied bias and they will start drifting to electrodes (fig. 3.2 D). The electrons will drift in the direction of the positive contact (anode) and the holes will drift in the direction of the opposite electrode (cathode). As discussed before equilibrium carrier concentration in the semiconductor is very small and photo-generated carriers will drift, if the electric field is constant in the detector, with a constant velocity $v = \mu E$.

The clouds of e-h pairs generated by the photon-matter interaction have not uniform charge density since e-h pairs production increases towards the end of the track of the photoelectron (e.g. for 100 KeV photoelectron, 30% of e-h are generated in the last $7\mu m$ of the total path that is around $47\mu m$[10]). Moreover the characteristic K X-rays (e.g. 25 KeV in CdZnTe) generated in the first interactions increase the size of the clouds since they have a mean free path of around $85\mu m$. If the effect of the non uniform charge density can be neglected the clouds can be approximated as Gaussian distribution with a σ spatial dimension. σ includes all the e-h pairs generated by photoelectron and characteristic X-rays.

Due to the effect of thermal diffusion of carriers, the space distribution of these clouds is not fixed in time, in particular the cloud dimensions will increase with time. This effect represents an intrinsic limit for imaging applications. This because in the case of imaging detectors (strips and pixels) several independent electrodes with dimensions comparable with those of the cloud are used. In particular, when the size of the cloud is comparable with the electrodes dimensions, there is a phenomenon called "charge sharing". In this process the charge is shared between two different electrodes decreasing or compromising the energy and the spatial resolutions of the detector.

The final dimensions of the clouds after the drift along the detector is an important parameters that must be calculated for a fixed energy. For simplicity only the one-dimensional diffusion will be treated. First of all it is possible to calculate the drift time t of the charges (assuming a constant electric field):

$$t = \frac{z}{v} = \frac{z}{\mu E} = \frac{zd}{\mu V_b} \tag{3.2}$$

where z is the interaction depth, d is the thickness and V_b is the voltage across the device. The longest drifting time is when the interaction depth is exactly d.

During this drift time the distribution of charge will change due to the thermal diffusion of the carriers as mentioned before.

The diffusion length can be calculated using the Fick's laws of diffusion:

$$\sigma = \sqrt{2Dt} \tag{3.3}$$

where D is the diffusion coefficient that is linked to mobility by the Einstein relation:

$$D = \frac{kT}{e}\mu \tag{3.4}$$

Using 3.2 with d as value of interaction depth, the 3.3 becomes:

$$\sigma = \sqrt{2\frac{kT}{e}\frac{d^2}{V_b}} \tag{3.5}$$

Using this relation the dimensions of the charge cloud can be evaluated starting from its initial dimensions. Consider now the case of a CdTe based detector and a 100 KeV photon that interacts with the detector. It is reasonable to consider that the initial cloud has dimension of around $\sigma = 70\,\mu m$ (that can be calculated considering the photoelectron and characteristic X-ray mean free path). Considering all other parameters $d = 5\,mm$, $T = 300\,K$, $V_b = 400\,V$ and $D_{CdTe} = 0,0026\,m^2/s$ the transverse diffusion can be calculated. The result is $\sigma \simeq 190\,\mu m$ that is more than double the initial cloud dimension.
In order to limit this effect special detector with a special electric field can be designed. In these devices the lateral electric field (generated by non-collecting electrodes) is strong enough to compress the charge cloud and guide it to the collecting electrode. In this way a strong reduction in the charge sharing can be obtained and a better spatial resolution can be achieved. This type of detector will be discussed in chapter 6.

3.3.3 The Effect of Trapping on Charge Collection Efficiency

In the real world semiconductor crystals are not perfect and normally they contain different type of defects like vacancies, impurities, grain boundaries, dislocation etc.. These defects can introduce energy levels inside the energy gap, creating traps or recombination centres for carriers. Due to these levels electrons and holes are characterized by a well defined lifetime τ that depends on the amount of these levels in the energy gap and on the nature of the carriers (τ_e and τ_h). These constants represent the mean time in which carriers move inside the material before trapping or recombination.
A general cloud of charge Q_o , for example, will decay (due to traps) in time following an exponential law governed by the life time constant:

$$Q(t) = Q_o e^{-\frac{t}{\tau}} \tag{3.6}$$

It is possible to express the decay in form of a length by replacing t in the previous formula with x (assuming that the carriers will drift with constant velocity $v_s = \mu E$):

$$t = \frac{x}{v_s} = \frac{x}{\mu E} \tag{3.7}$$

replacing the 3.7 inside 3.6 the decay of the charge can be now expressed as function of depth x:

$$Q(x) = Q_o e^{-\frac{x}{L}} \tag{3.8}$$

$L = \mu\tau E$ represents the mean drift length for a single charge and it is an important parameter for detectors. In order to collect all the carriers the detector thickness must be higher than L calculated with the operative bias of the detector.

We can consider now the case of simple planar geometry. The charge Q_0 , once generated, will induce a signal in the electrode during its drift. The contribution of induced signal dQ_i for a traveling charge $Q(x)$ at distance dx can be expressed as:

$$dQ_i = Q(x)\frac{dx}{d} \tag{3.9}$$

The total induced charge to the electrode is simply the integral of 3.9:

$$Q_i = \frac{1}{d}\int_0^d dQ_i = \frac{1}{d^2}\int_0^d Q_o e^{-\frac{x}{L}}dx \tag{3.10}$$

$$Q_i = Q_o\frac{L}{d}(1 - e^{-\frac{d}{L}}) \tag{3.11}$$

As shown in fig.3.1 the $\mu\tau$ product can be different for holes and electrons. Therefore for a cloud of charge (electron-hole pairs) created in a generic position z inside the detector volume, and considering the contribution of both electrons and holes in the induce signal, equation 3.11 becomes:

$$\frac{Q_i}{Q_o} = \frac{L_e}{d}[1 - exp(\frac{d-z}{L_e})] + \frac{L_h}{d}[1 - exp(\frac{z}{L_h})] \tag{3.12}$$

where $L_e = \mu_e\tau_e E$ and $L_h = \mu_h\tau_h E$. The ratio Q_i/Q_o represents the "charge collection efficiency" (CCE) and expresses the efficiency in the collection of carriers. The perfect detector should have CCE equal to one. The expression 3.12 is called Hecht equation [11] and expresses the variation in the induced charge due to trapping process. Theoretically it must be take into account also the opposite process of de-trapping of the carriers that woks in opposite direction to the trapping process. Normally the de-trapping process can be neglected because it is slowest than the typical collecting time of carriers. Using 3.12 is possible to extrapolate $L_e = \mu_e\tau_e E$ and $L_h = \mu_h\tau_h E$ from a CCE measurement. CCE depends on transport properties of carriers and on applied electric field $E = \frac{V}{d}$. Therefore transport properties can be extracted by the measure of CCE as function of applied voltage. We'll came back on this type of measurement also later (chapter 5)

3.3.4 Ramo-Shockley Theorem

As discussed in chapter 2, the interactions between radiation and matter generate a large number of electron-holes pairs. This moving charge q will drift under the electric field inducing, along its trajectory, a charge Q on the electrodes. The charge Q will be amplified and converted in a voltage by a charge sensing amplifier. The output voltage signal will be proportional to the energy deposited by the photon.

In order to calculate Q, prior Ramo-Shockley theorem, one had to calculate the instantaneous electric field for each point of the trajectory of q, than calculate the charge Q integrating the normal electric field over the surface surrounding the electrode. The goal of Ramo-Shockley theorem is to simplify this procedure for calculating the induce charge in presence of a complex system like detector. Shockley (1938) [12] and Ramo (1939) [13] found independently a method to calculate induced charge on any number of electrodes for any type of geometry of electrodes. The first results were found for a system composed by several electrodes mounted inside a vacuum

tube. Later it was proven that the Ramo-Shockley theorem is valid also in system with the presence of stationary spatial charges[14].
Consider therefore a general system constitute by: a well defined number of electrodes with surface S_i biased with constant voltages, a moving charge q and a spatial static charge ρ. For this general system the Ramo-Schockley theorem states that the charge Q and the induced current i on one electrode by moving charge q are:

$$Q = -q\varphi_0(\mathbf{z}) \tag{3.13}$$

$$i = q\bar{v} \cdot \bar{E}_0(z) \tag{3.14}$$

where q is the value of the charge $(\pm e)$,$\bar{v}$ is the instantaneous velocity of the charge, $\varphi_0(\mathbf{z})$ and $E_0(\mathbf{z})$ are called respect weighting potential and weighting field. These last two quantities represent the potential and field calculated in the system for instantaneous position of q (z) under these conditions:

- The selected electrode (only one) rise at unit potential.
- All other electrodes are grounded.
- All static charges are removed ($\rho(\mathbf{r}) = 0$)

The charge induced to the selected electrode is independent of space charge $\rho(\mathbf{r})$ and of the applied bias on the electrodes. The proof of the theorem is outside the scope of this work but it is possible to find it in the original works and in a very good review by Zong He [15].

3.3.4.1 Planar geometry

It is possible now to apply the Ramo-Shockley theorem to calculate the induced charge in the simplest case of two planar electrodes (planar detector). When a gamma ray is absorbed (photo-electric) a large number of e-h pairs are created. Due to the bias (V) the electrons start to drift in the direction of the anode and the hole in the opposite direction: no trapping is considered now. The output signal will be therefore the sum of these two contributions (electrons and holes). The first step is to calculate the weighting potential in the system considering, for example, the anode like readout electrode. In this configuration the weighting potential can be easily calculated, it varies linearly in z from the value 0 (cathode surface $z = 0$) to 1 (anode surface $z = 1$) as shown in fig.3.3 (red line). Hence:

$$\varphi_0(z) = z \qquad 0 \leq z \leq 1 \tag{3.15}$$

Using 3.13 it is possible to calculate the total induced charge to the anode for a generic point of interaction Z as:

$$\Delta Q = -(ne)(\varphi(0) - \varphi(Z)) - (-ne)(\varphi(1) - (Z)) \tag{3.16}$$

where n is the number of e-h pairs (no trapping means $n_e = n_h$). The first part of 3.13 is the hole contribution and the second one is the contribution of electrons. If no trapping is considered the total induced signal will be simply:

$$\Delta Q = ne \tag{3.17}$$

The result is consistent: the signal induced on anode is proportional to the number of e-h pairs generated (proportional to $h\nu$).
At this point it is necessary to introduce also the trapping effect in particular for holes. This because in CZT, for example, the mean free path of holes ($\mu_h \tau_h E$) is typically less than the detector thickness.
In order to understand the effect of trapping, consider now the extreme case in which all the generated holes are trapped immediately after generation. The induced charge in this case is only due to by electrons, the 3.16 becomes:

$$\Delta Q \simeq ne(1 - Z) \tag{3.18}$$

In this extreme case the signal is induced only by electrons and it depends on the interaction position. This means that the signal can not be the same for two identical photons absorbed in two different positions of detector.
In real semiconductor materials, for example CZT, there is always a contribution of holes in the induced signal. The point is that this signal is very low compared to those of electrons. The result is that for a planar detector with strong trapping of holes, the induced signal depends on interaction position that is random. This effect can strongly compromise the energy resolution of the detector.
In order to eliminate this problem a different approach must be considered, in particular different weighting potential must be designed. The idea is to use a weighting potential in which the induced signal of holes is eliminated and the signal induced by electron is position indipendent. This type of weighting potential is shown in fig.3.3. This technique is called "single polarity charge sensing" and can be achieve with special electrode geometries: small pixel[16], stripes and coplanar grids[17][18].

3.3.5 Energy Resolution

The energy resolution of a detector is the ability to resolve fine details of the incident radiation spectra. Consider now a mono energetic source of radiation that interacts via photoelectric absorption in the detector. The response of the device will be a distribution centered around an average pulse amplitude (H_0) with a Y number of counts as shown in fig.3.4. The energy resolution of the detector is connected to the full width half maximum (FWHM) of this distribution calculated removing an eventual background from the peak. The formal definition of energy resolution R is the ratio between FWHM and the value of the position of the peak H_0.

$$R = \frac{FWHM}{H_0} \tag{3.19}$$

The distribution should have a Gaussian shape because the total number of charge carriers generated N is normally very high. The FWHM of any Gaussian can be calculated through the relation $FWHM = 2.35\sigma$. Is important now to understand which parameters can change the width of the peak of Gaussian distribution.
The minimum energy difference detectable is limited by the statistic fluctuations in the created

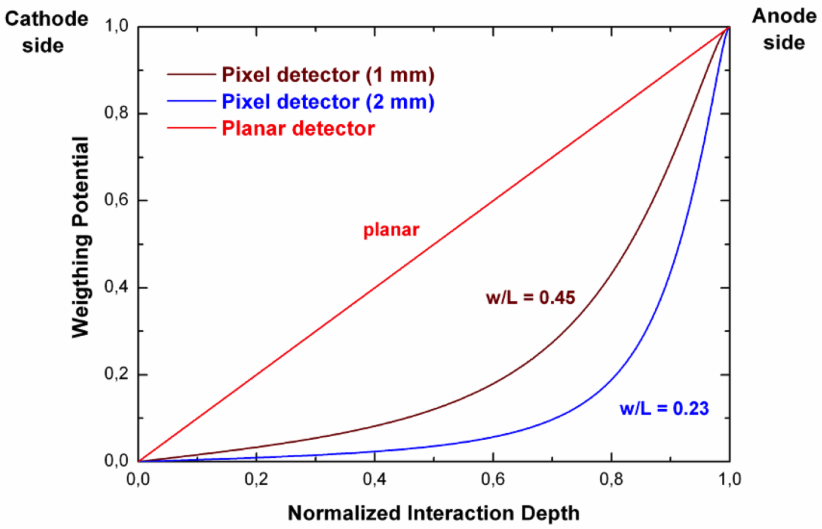

Figure 3.3: *Comparison between the weighting potential for pixel detectors and a planar detector as a function of the normalized interaction depth. w/L is the ratio between the pixel size and detector thickness.* [19]

charge. The energy resolution calculated considering only statistical fluctuations represents the maximum level of resolution that is possible to achieve. The energy can be absorbed in different way by the detector lattice, like by creation of phonons or by creation of free carriers. According to the law of energy conservation the sum of the total excitation and ionization energy must be equal to the initial energy deposited inside the detector.

$$E_0 = N_x E_x + N_i E_i \tag{3.20}$$

where N_x and N_i are respectively the number of excitations and ionizations and E_x and E_i are the energies relative at single excitation and ionization. In the case of semiconductors E_i is connected to band gap energy E_g. For single event of interaction, considering no fluctuations in the value of the initial energy of the photon E_0, and assuming a Gaussian statistic, the 3.20 becomes:

$$E_x \sigma_x = E_i \sigma_i \tag{3.21}$$

where $\sigma_x = \sqrt{N_x}$ and $\sigma_i = \sqrt{N_i}$. Averaging over many events, the variance in the energy allocated in this two types of process must be equal because there is no fluctuation in E_0 . Obviously for detectors only the events of ionization (that create free carriers) will be important. The fluctuation in the ionization σ_i is the important parameter to determinate the energy resolution of the device:

$$\sigma_i = \frac{E_x}{E_i} \sigma_x \tag{3.22}$$

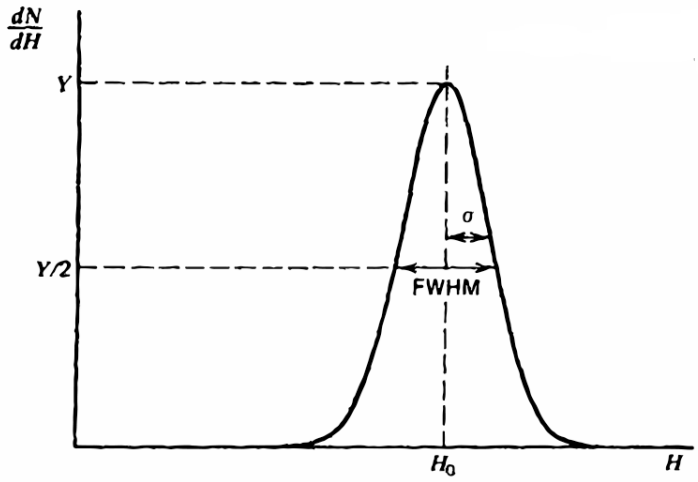

Figure 3.4: *Energy resolution for a peak with a Gaussina shape. [3]*

Using 3.20 and 3.21 σ_i becomes:

$$\sigma_i = \frac{E_x}{E_i}\sqrt{\frac{E_0}{E_x} - \frac{E_i}{E_x}N_i} \tag{3.23}$$

N_i is the number of e-h pair created and it can be calculate using the ionizing energy (Klein rule) $N_i = \frac{E_0}{\epsilon_i}$. Using this relation the σ_i becomes:

$$\sigma_i = \sqrt{\frac{E_0}{\epsilon_i}}\sqrt{\frac{E_x}{E_i}(\frac{\epsilon_i}{E_i} - 1)} \tag{3.24}$$

The second part of 3.24 is called Fano Factor F. Finally the result is that the variance in the number of e-h pair created is not simply the root of the number of pair created (Poisson statistic) but there is a correction constant that considers also the energy loss in the excitation process. Will exist therefore, for every type of semiconductor detector, a maximum value of resolution limited by statistic fluctuations:

$$R = \frac{FWHM}{H_0} = 2.35\frac{\sqrt{N}}{N} = \frac{2.35}{\sqrt{N}} = 2.35\sqrt{\frac{F}{N}} \tag{3.25}$$

Knowing the Fano Factor it is possible to calculate, for every incident energy, the maximum achievable resolution of the detector.
In general also other sources of fluctuation can contribute to decrease the resolution of the detector. In general the resolution is limited by all the fluctuation in the signal measured by detector. In general the total FWHM will be the convolution of all the fluctuations present in the system:

$$(FWHM)^2_{measured} = (FWHM)^2_{statistical} + (FWHM)^2_{dark} + (FWHM)^2_{noise} + (FWHM)^2_{trapping} + ... \tag{3.26}$$

To increase the energy resolution of the detector is important to reduce the contribution of all fluctuations. Unfortunately the Fano factor is a statistic parameter and, for this reason, the only way to decrease it is to change the material (ϵ_i and E_x).
As discussed in 2.3.3. also the trapping can decrese the amplitude in the induced signal. The incomplete collection of all charge can enlarge the low energy part of the peak. This effect ($FWHM_{trapping}$) can be decresed using material with good transport properties.
The most important source of fluctuation is the electronic noise. This noise is directly connected to the electronic read-out chain. The contribution of this noise ($FWHM_{noise}$) is always larger than the contribution of the statistical fluctuation. $FWHM_{noise}$ can be easily evaluated by measuring the FWHM of the read-out system with a signal input. This procedure will be discussed later.
In the next section the contribution of the dark current in the signal fluctuation ($FWHM_{dark}$) will be discussed.

3.3.6 Dark Current and Role of Contacts

The dark current in the detectors should ideally contribute less to total noise than noise contribution from the system electronics. Being a source of fluctuation in the signal, dark current can decrease the energy resolution of detector. Dark current depends on material resistivity, temperature, operative bias, quality of surfaces and electrical contacts. Some considerations about origin of dark current should be mentioned:

- Resistivity of the material depends on band gap energy but also on material quality (for example the doping of the material)
- Temperature increases the number of free carriers thermally generated, so that operating temperature of the detector must be correctly considered.
- For a material with poor transport properties high bias must be applied to the detector in order to collect all the generated carriers. But high voltage difference generally increases detector dark current.
- Most of semiconductors suffer the problem of surfaces, in particular the resistivity of the surfaces is usually lower than the resistivity of bulk. In the detector there are therefore two resistors in parallel: one is the resistance of the bulk, the second is the resistance of the surface. The total dark current is due to the lowest resistance that normally is due to surface. In order to reduce this effect surfaces must be treated with “passivation processes”(examples of similar processes will be shown later).

Also metal-semiconductor contact can paly an important role for decreasing the dark current of the device. In general two different types of contacts can be obtained in a metal-semiconductor interface: ohmic contact, injecting and blocking contact. Depending on metal work function and the type of semiconductor conductivity (p or n) a contact showing rectifying properties can be obtained (also known as Schottky barrier). In particular a blocking contacts can be formed if the metal-vacuum work function is higher than the semiconductor-vacuum electron

affinity. In this type of contacts the current flow through contacts is not depended on material resistivity but depends on the height of the barrier at metal-semiconductor interface. In fig.3.5 a IV characteristics CdZnTe detector with both Schottky type contacts (blue line) and ideal ohmic contacts (red line) are shown. The characteristic with ideal ohmic contact is calculated using the resistivity of the material, the dimension of the contacts and the thickness of the detector. As shown in figure 3.5 with Schottky contacts a strong reduction of the dark current can be achieved. The main problem is that not for all semiconductors is trivial to obtain such type of contacts.

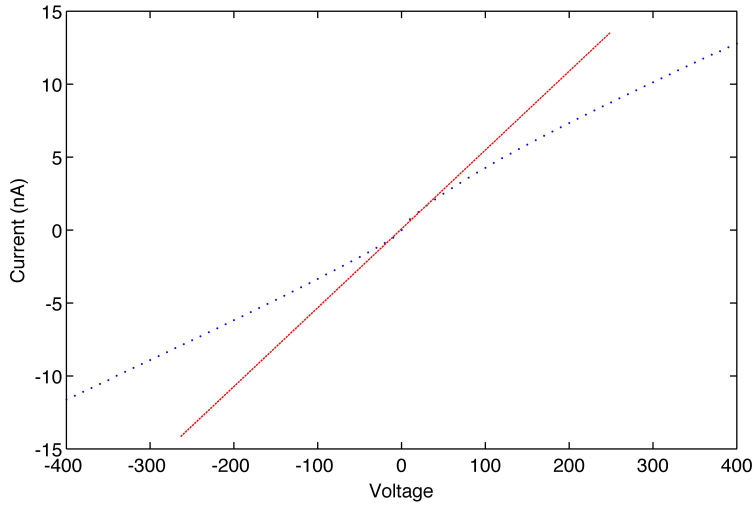

Figure 3.5: *(blue dotted line) IV characteristic of a CZT detector with two gold contacts that show a two diode back-to-back characteristic. (red line) IV characteristic calculated for the same CZT detector with two ideal ohmic contacts.*

Moreover also the device preparation and the deposition technique can affect the characteristic of the contacts in a strong way. In general for each material a development in contact preparation for semiconductor radiation detector was done and still remain in some cases an open challenge. In general for radiation detectors, at low photon fluxes, Schottky type contacts are preferred in order to decrease the dark current. In chapter 5 contacts preparation of CZT based detector will be discussed.

3.3.7 Detection Efficiency

In general detection efficiency is the ratio between the number of photons actually counted out and the total number of photons received by the sample. It is very difficult to evaluate precisely the efficiency of a radiation detector and standards are needed in order to measure this quantity. In general two classes of efficiency can be distinguished: absolute and intrinsic efficiency.

- The absolute efficiency is defined as the ratio between the number of recorded pulses and the number of photons emitted by the radiation source. This quantity depends on the efficiency of the detector and on the counting geometry. Both the geometry and the energies at which it is measured must be specified when absolute efficiency is quoted.

- The intrinsic efficiency is defined as the ratio between the number of recorded pulses and the number of photons that affect the detector. This quantity depends on detector material, energy of incident photons and the dimension of the detector in the direction of the incident radiation.

3.3.8 Peak-to-Compton Ratio

Compton scattering is the most important interaction in a semiconductor crystal for gamma rays with energies between hundreds of keV to few MeV depending on material. For Compton scattered photons that escape the crystal no signal is detected. But recoil electrons deposit energy and produce counts in the energy region below the full energy peak of the incident photon. This Compton continuous background, which is in addition to the background from ambient sources, increases the minimum detectable activity of any photons with peaks in that region. Thus, in samples with multiple sources, the additional background due to Compton scattering of the higher energy photons occurs over all the lower energy regions. In general, a detector with a higher peak-to-Compton ratio will have higher line-to-background ratios and better counting statistics for complex spectra. This is very important for environmental monitoring. The peak-to-Compton value depends on several detector properties: contact geometry, detector efficiency and detector resolution. It increases with detector active volume and decreases with increase in the energy FWHM.

3.3.9 Response Function of Semiconductor Detector

At the end of this chapter it is useful to analyse the typical pulse spectra of a semiconductor detector: in this case a CZT based detector is considered.
All the possible interactions between photons and matter are discussed in chapter 2 and the characteristics of a typical semiconductor detector are discussed in chapter 3. With these information a general pulse spectrum can be formulated.
As shown in figure 3.6 in the real detector several interactions can contribute to the total pulse spectrum. The response of the detector is formulated under the following conditions:

- Incident photon energy lower than 1.02 MeV and, therefore, pair production effect is neglected.
- The surrounding materials (shielding box) must be consider because they can influence the response of the detector.
- The volume of the detector is not enough for absorbing all the secondary scattered photons (due to Compton interactions).

Following the labels of fig.3.6, the general response of semiconductor detector can be summarized as follow:

1) Peak 1 is due by surrounding materials. If the photon doesn't interact with the detector it can interact with other materials surrounding the detector. In the case of photoelectric

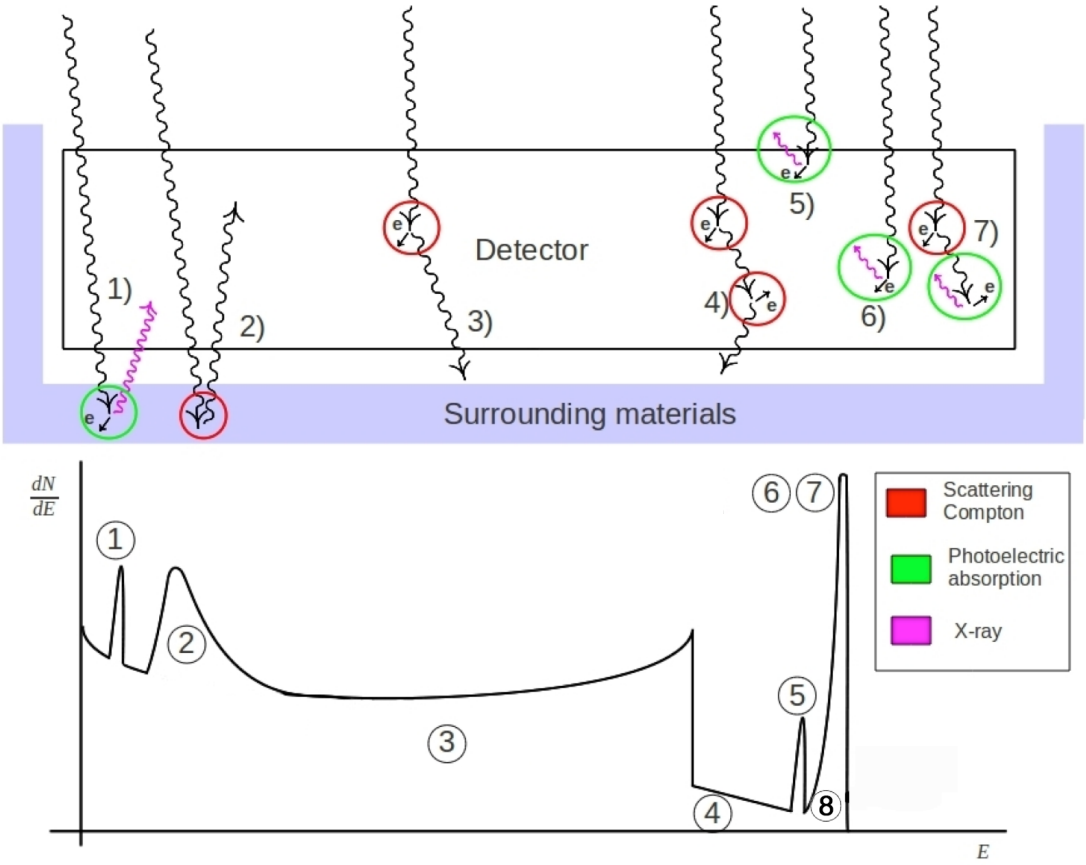

Figure 3.6: *(top) All possible sources of signal in a real semiconductor detector. (bottom) The pulse spectrum of the semiconductor detector.*

interaction with the surrounding materials a characteristic X-ray photon of the single material can be detected by the detector. Normally one characteristic peak can be detected at low energy in the response function (in general there is only one type of high density material sourronding the detector).

2) Also the peak 2 is due to the surrounding materials. In this case is the scattered gamma-ray that interacts with detector. In the cases 1 and 2 the source of radiation is the surrounding materials.

3) The Compton continuum is due to the Compton scattering in which only a fraction of the energy is deposited inside the material.

4) In the real case also in energy gap between the Compton edge and the photo-peak some events can be detected. These events are due by multiple Compton interactions. In this types of event the scattered photon can interact again with the detector. If also the second interaction is Compton a signal in position 4 can be detected.

5) After the emission of a photoelectron the atom researchs the equilibrium by the emission

of a characteristic X-ray photon. If the Photoelectric effect happens near the surface this secondary radiation can escape from the detector. These events appear with less energy than the photo-peak, this energy difference is equal to the escaped X-ray energy.

6) Photoelectric absorption without characteristic X-ray escape. These events form the photo-peak that appears at the same energy of the incident photons.

7) Also multiple interactions can deposit all the incident photon energy. In this example the first interaction is Compton and the second is a photoelectric absorption. The result is that all the incident photon energy is deposited inside the detector.

8) Also the trapping of carriers has an effect in the response of the detector. The main effect is the broadening in the low energy part of the photo-peak as will be shown in CdZnTe detector chapter.

Chapter 4

Lead Oxide

4.1 Introduction

In chapter 3, we discussed the physical properties that make a semiconductor an optimal material for x-ray direct conversion. Lead Oxide fulfils most of these properties and in particular:

- High Z (82 for Pb),
- Extremely high density (9.8 g/cm3)
- High resistivity ($> 10^{12} \Omega cm$ [8])
- Favourable band-gap (> 1.4 eV).

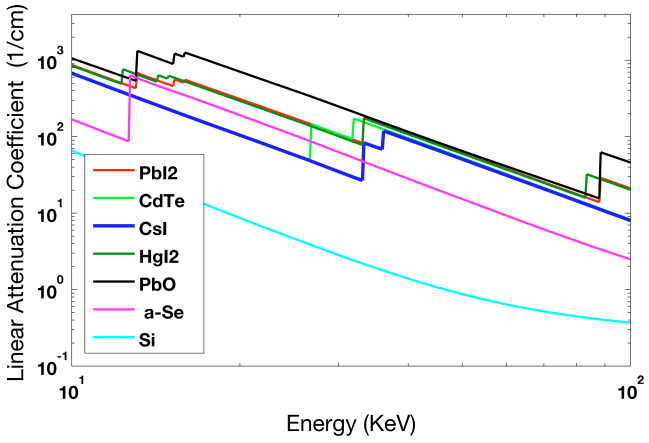

Figure 4.1: *X and γ linear attenuation for several compounds in the range $10 \div 100$ KeV.*

Figure 4.1 shows the linear attenuation coefficient for different materials. It is possible to note that PbO shows the higher stopping power (due to the high density and high atomic number) and the absence of any absorption edges in the typical energy range of medical applications (10–100 keV). This means that PbO is virtually a very interesting material in particular for medical applications (for example flat panel detectors).

Despite these interesting properties, the phase diagram of PbO is very complicate and characterized by several compounds with different stoichiometry (PbO_2, Pb_2O_3, Pb_3O_4[20]) as shown in fig.4.2. Moreover, also for Pb(II)O, two different phases are possible: tetragonal (α—PbO or

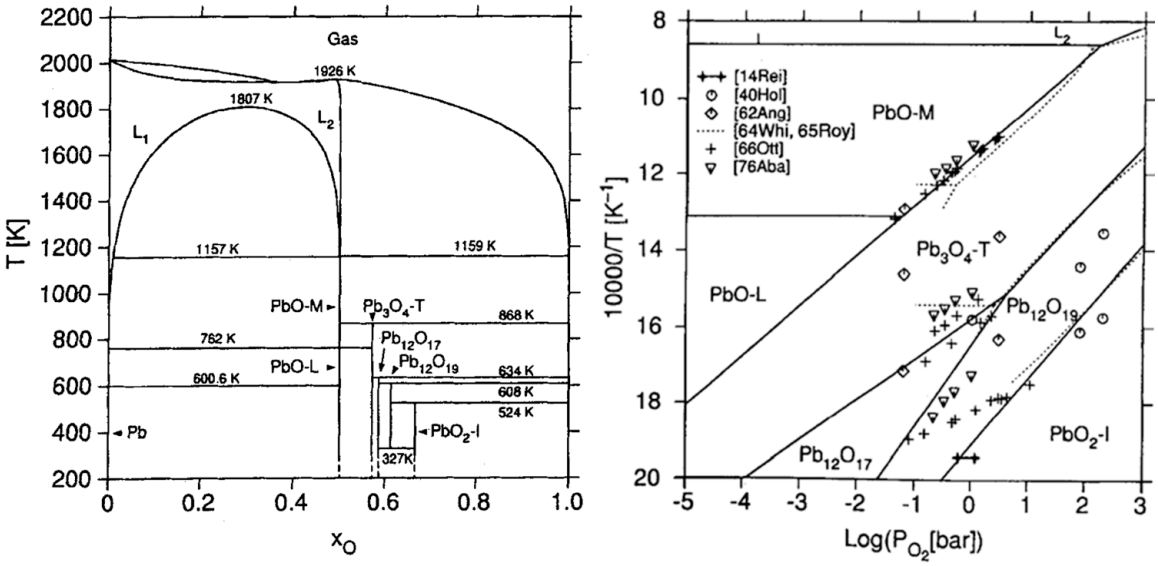

Figure 4.2: *Left) Phase diagram of Pb and O at 1 bar. Right) Calculated and measured field of stability of lead oxides as function of oxygen pressure.*[20]

Litharge) and orthorhombic (β-PbO or Massicot).

In the past attention was focused on the tetragonal phase of PbO due to the lower band gap value (1.9 eV [7]) and, as a consequence, lower energy for electron-hole pairs creation [10]. However, at low temperature where the tetragonal phase is the stable one, the orthorhombic metastable phase is also formed, according to the Ostwald step-rule. As a result it is very difficult to grow PbO films with only the tetragonal phase [7]. On the other hand β—PbO is the stable phase for temperature above 489°C, so that above this temperature it is expected that PbO films present only the orthorhombic phase. The drawback is that β-PbO has higher energy gap value (2.7 eV) and energy for electron-hole pairs creation (8 eV [10]), and this can decrease the signal-to-noise ratio compared with the α—PbO.

Another problem of Lead Oxide (both phases) is related to the transport properties, in particular the $\mu\tau$ product of carriers are not still well defined, and in any case, the reported values are quite low. In literature some values of $\mu\tau$ can be found but some sort of uncertainty still remains. For example John C. Schottmiller in 1966 with photocurrent measurements, assuming one carrier transport, [21] found the values of $\mu\tau$ for tetragonal and orthorhombic respectively $\mu\tau = 4 \cdot 10^{-7} cm^2/V$ and $\mu\tau = 1 \cdot 10^{-9} cm^2/V$, without any specification about the type of carrier. R. Keezer in 1968 [22] using the same technique (assuming again single carrier transport) found considerably higher value of $\mu\tau$, in particular he found for tetragonal phase a $\mu\tau = 10 cm^2/V$ and $\mu\tau = 4 \cdot 10^{-4} cm^2/V$ for orthorhombic one. More recently (2005) M. Simon [23]found for PbO polycrystalline film with a mix of both phases (more amount of α—PbO) a $\mu\tau = 4.4 \cdot 10^{-7} cm^2/V$ when irradiating the negatively biased electrode with X-rays. Values of the same order of magnitude were found in a separate experiment with blue light excitation for both electrons and holes.

It is clear that the real transport properties cannot be extracted from literature. The main problem is that each measurement was not done in the same conditions, in particular no measurements are available in literature on good single phase single crystal PbO samples. Without any clear information on the transport properties of both carriers, PbO cannot be considered seriously as radiation detector materials.

The aim of this work was to grow single crystal and poly-crystalline Lead Oxide samples of the orthorhombic phase and tried to measure the transport properties of both electrons and holes. The choice of the orthorhombic phase was not accidental, β-PbO in facts above 489°C only the β-PbO is stable and a single phase can be grown. The main drawback, reported in literature[24], of β-PbO is the conversion in α—PbO for temperature below 489°C in presence of water vapor. In the β-PbO samples grown at IMEM-CNR institute no phase transition was observed for over several months.

4.2 Crystal Structure and Band Structure

The crystal structure of orthorhombic PbO is shown in fig.4.3 and fig.4.4[25][26]. Above 489°C β-PbO crystallizes in orthorhombic system, space group: Pcbm (No. 57) with **a** = 5,4904 $\mathring{A}$, **b** = 4,7528 $\mathring{A}$, **c** = 5,8931 Å[25]. As shown in fig.4.4 the structure of β-PbO consists in layers stacked together along the **c** axes. In each layer two oxygen planes (fig.4.3b and fig.4.3c) are sandwiched between two lead sublayers, which form the outside of the layer. The layers are made up of parallel -Pb-O-Pb- zig-zag chains (fig.4.4). As shown in fig.4.4 right, the distance between two lead atoms of different layers is 3.97 Å that is 0.5 Å higher than the interatomic distance in metallic lead. This means that the interaction between two different layers is very weak, and in literature is not clear if this interaction has a weak bonding or van der Waals behaviour. Despite this uncertainty in the type of interaction it is possible to state that the interaction between layers is very weak[27].

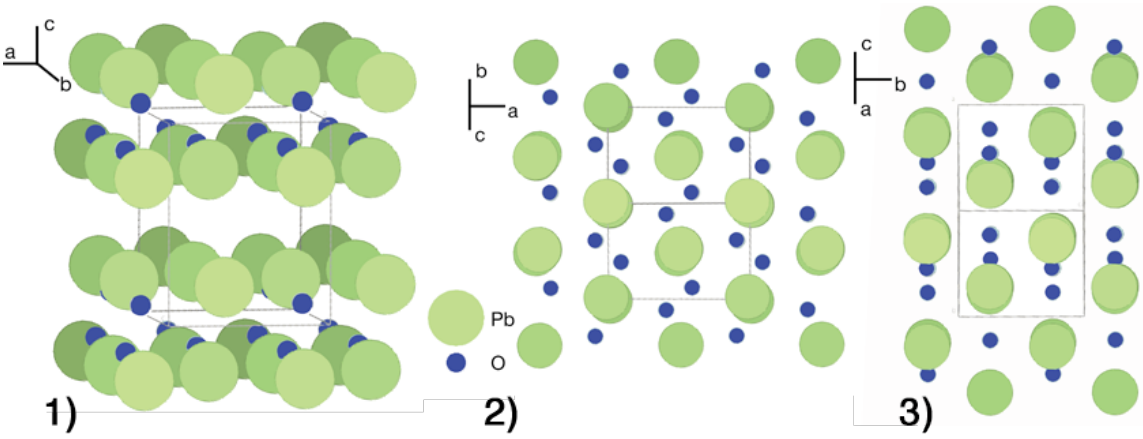

Figure 4.3: *Different projections of the crystal structure of the Orthorhombic PbO (space group: Pbcm 57).[28]*

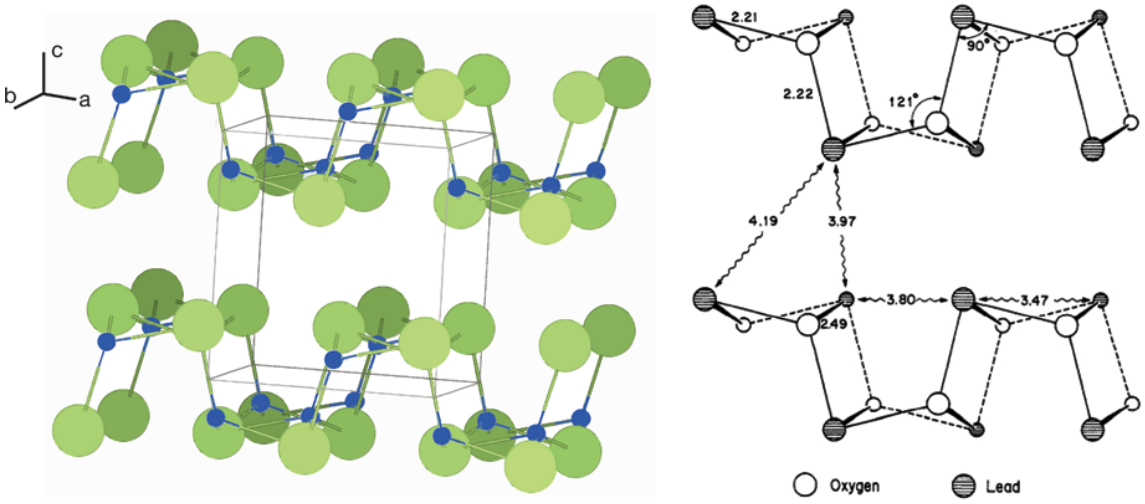

Figure 4.4: *Projections of the crystal structure along c axes, on the right figure the bonding length are specified according[26].*

The calculated band structure of β-PbO[26] is shown in fig.4.5. The energies are given with respect to the top of valence band (signed with a red square in fig.4.5), the bottom of conducting band is along another direction of the Brillouin zone (green square). The band gap of β-PbO is indirect and the value is, at 300K, 2.7 eV. From the calculated band structure, considering the slope of of valence band top, a large effective mass of holes must be expected. The results is that in β-PbO a small hole mobility is expected (the same also for α—PbO). On the contrary, considering the bottom of the conduction band, the mobility of electron must be much higher than the mobility of holes.

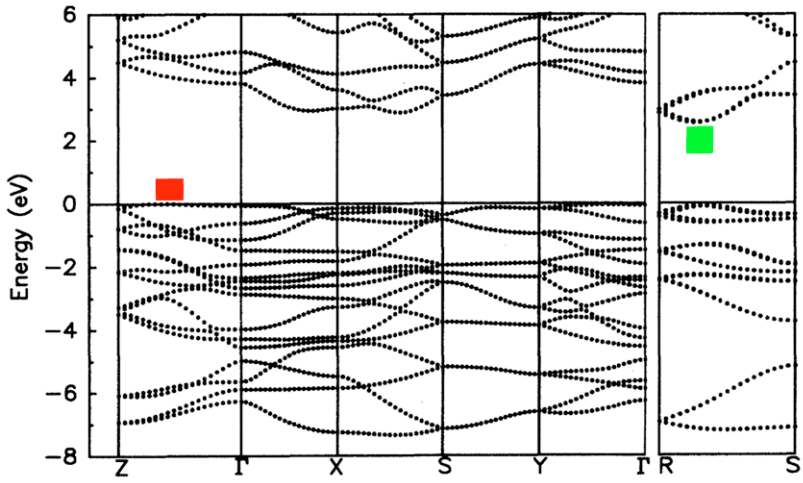

Figure 4.5: *Band structure of β-PbO, the top of the valence band is positioned along $Z - \Gamma$ direction, the bottom of the conduction band is along the $R - S$ direction[26].*

4.3 Polycrystalline films

4.3.1 Introduction

Nowadays X-ray detectors are widely used in different fields of application. In particular, in the last years, a lot of interest was focused on medical imaging and non-destructive investigation tests. These applications require low cost sensors with active area larger than the shadow produced by target object in order to record all information. These large area detectors are called flat-panel x-ray detector. These detectors consist of a large active matrix array covered by a suitable material that converts x-ray photons into electric signals. The main goal of this configuration is that each pixel has a TFT (thin film transistor) directly connected to the active material, so the number of pixels can be very large (as required in x-ray imaging applications). Two different approaches are available to detect x-rays, as previously discussed in chapter 3: indirect and direct conversion. With direct conversion of absorbed x-rays it is possible to increase signal-to-noise ratio avoiding the signal losses by x-ray/light conversion enhancing the intrinsic spatial resolution of the devices. There are several materials that are under investigation for flat-panel detector applications. The choice of the material is also limited by the constraints required for imaging application, that are large active area and low cost fabrications. This means that only polycrystalline or amorphous films are usually considered. The most considered materials for this application are amorphous Se, amorphus Si, polycrystalline $CdZnTe$, HgI_2 , PbI_2 and PbO.

4.3.2 Growth

β-PbO polycrystalline films were obtained by means of a combined thermal evaporation of metallic Pb source and controlled oxidation. The grow apparatus was a two zones tubular furnace where different gases can be flowed through as shown in the sketch of fig.4.6. A similar apparatus

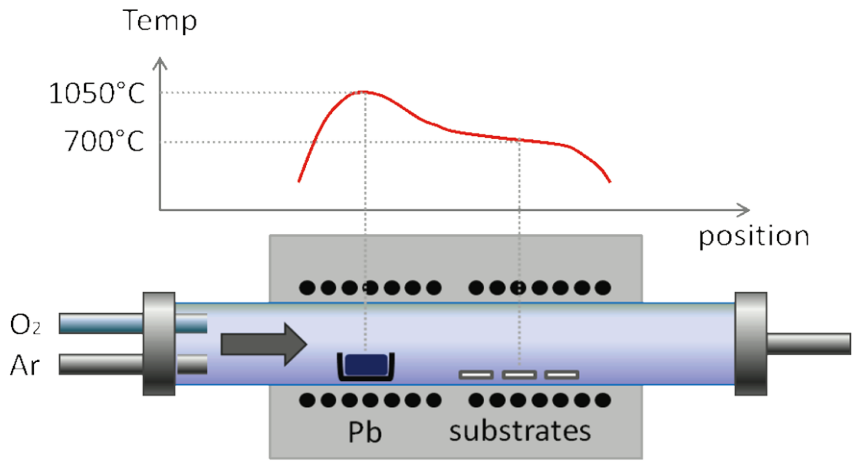

Figure 4.6: *Sketch of the two zones tubular furnace and the temperature profile.*

was used in the past to deposit other metal-oxides, as SnO_2[29], In_2O_3 [30], and ZnO[31]. The films were obtained on alumina substrates. This because i) alumina is inert to Pb and oxygen vapors, ii) it is a rather good thermal conductor, iii) substrates down to 100 micron thickness

are available, iv) it shows a low stopping power to X-ray. PbO vapors are very aggressive with glass and quartz and, therefore, also the reaction tube was made of alumina.
Pb metallic source was placed in the hottest place of first zone (figure 4.6), inside an alumina container with only a small window through which Pb vapors can exit, while alumina substrates were placed a few centimetres downstream in the second zone. Temperature gradient among these two zones was set in order to obtain the desired liquid Pb re-condensation on the substrates at the desired temperature, i.e. in the optimal configuration source zone was heated up to 1050°C while substrates were kept at 800°C. During the first step of the growth process only Ar was flowed along the furnace (100 ml/min) while temperature was raised up to the maximum value. Once this temperature was reached, Ar flow was maintained for 5 minutes in order to let Pb transport and condensation take place. Then the second step of the growth process started by introducing oxygen in the reactor (1000:1 Ar/O2 ratio, 100 ml/min total flow). After 25 minutes, the furnace was switched off and cooled down to room temperature. After growth, a yellow film was visible on alumina substrates, clearly suggesting the formation of the orthorhombic phase.
Substrate temperature and oxygen partial pressure were chosen in order to promote the formation of β-PbO using the graph in fig.4.2 (right). The described growth setup and process were based on two different growth steps. During the first step Pb is heated in inert gas (Ar) in order to promote its evaporation, while the combination of transport and temperature gradient promotes the re-condensation of Pb droplets on the substrates. During the second step of the process oxygen is introduced in the reactor and the oxidation process starts. In the substrate zone, a different Pb condensation is obtained with a nearly continuous gradient. In the farthest position from source, the deposition is limited and SEM images reveal that Pb droplets transform into PbO crystals with a round plate-like shape (figure 4.7). Their typical size is 10–20 microns

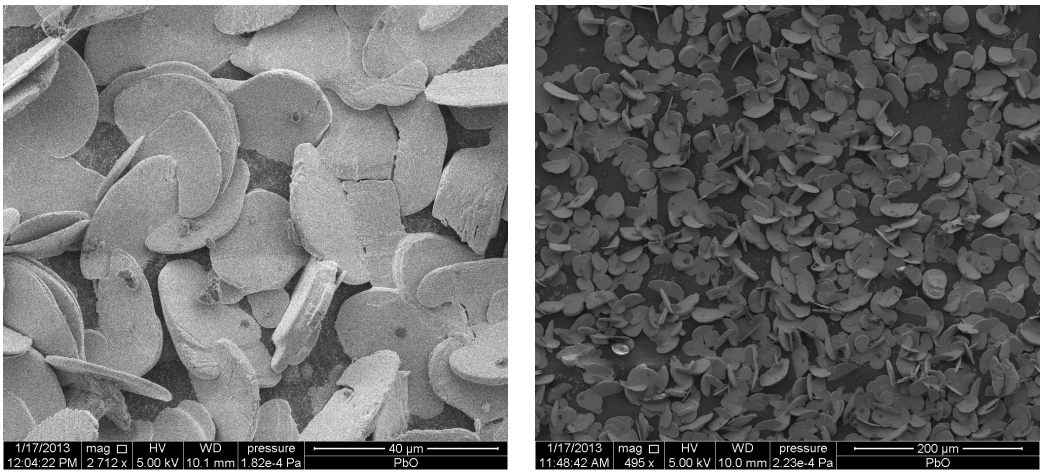

Figure 4.7: *Plate-like crystals of Lead Oxide grown in the farthest position from source.*

while their orientation on the substrate is almost random. On substrates closer to the Pb source, where Pb deposition is larger, a continuous film is observed (figure 4.8) because of the more homogeneous and dense distribution of Pb droplets. Indeed, once droplets are oxidized, they grow laterally, merging together in a rather continuous film. Moreover, under these conditions plate-like micro-crystals are also mainly aligned with a common orientation, i.e. with their flat

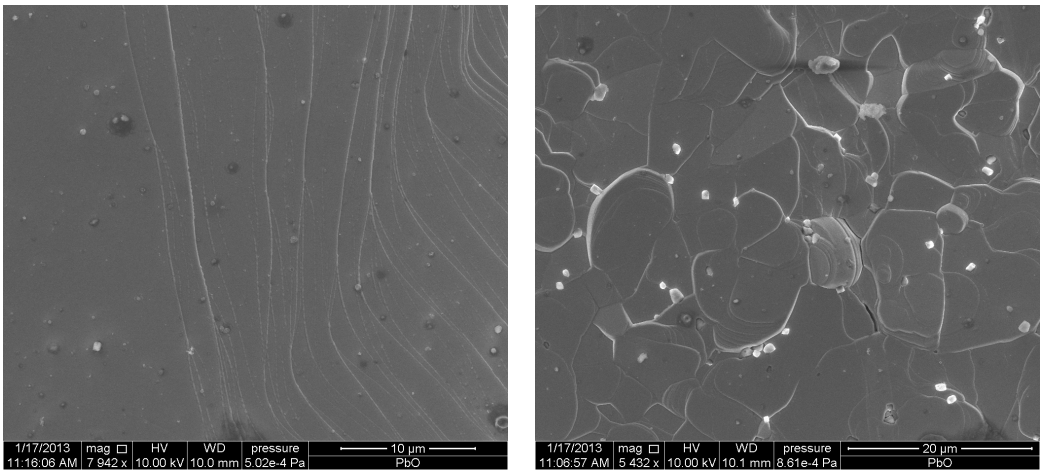

Figure 4.8: *ESEM-FEG images of the continuos film of Lead Oxide grown close to the lead source.*

surfaces perpendicular to the substrate as shown in fig.4.9. The typical thickness of these films

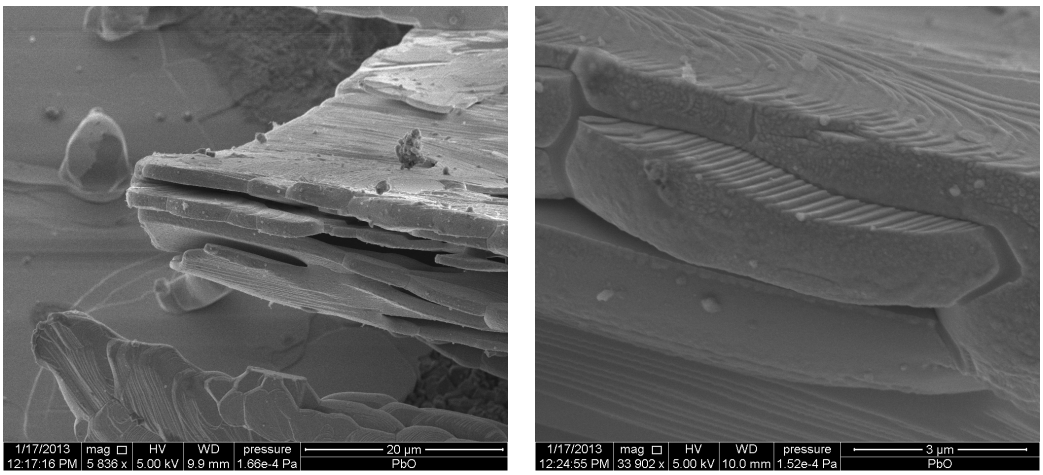

Figure 4.9: *ESEM-FEG images of the film in some broken parts in order to evaluate the thickness.*

are in the range is $15 \div 20\,\mu m$ as shown in fig.4.9.

Growth mechanism

The growth of the round plate-like crystal can be explained considering the phase diagram shown in fig.4.2(left). In the first part of the growth no oxygen was present inside the system and therefore only Pb was present (left part of the phase diagram). Due to the supersaturation caused by the temperature gradient, lead started to condense to the substrates as big lead drops. When oxygen started to flux, Pb drops on substrates started to oxidize and β-PbO started to crystalize. Due to the continuous fluxing of oxygen the equilibrium of oxidation reaction was always favourable for β-PbO formation. As shown in the phase diagram of fig.4.2 (left) the liquid Pb is in equilibrium with the β-PbO solid at the temperature of substrates (800°C).
Due to the large amount of Pb present in the substrates close to the source the round plate-like

crystals started to coalesce creating a continuous film (fig.4.8), while on the substrates far from the source the plate-like crystals are isolated (fig.4.7).

4.4 Film Characterizations

4.4.1 Morphology

Film morphology was studied by means of an ESEM-FEG FEI Quanta 259 (figures 4.7, 4.8, 4.9).

4.4.2 X-ray diffraction

4.4.2.1 Experimental Setup

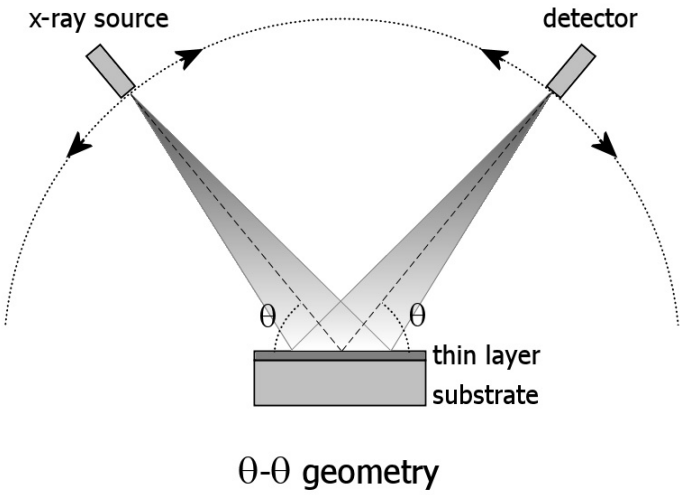

Figure 4.10: *X-ray diffraction setup.*

The X-ray DIFFRACTION (XRD) were taken directly on the grown films with Thermo ARL X'TRA Powder X-ray Diffratometer. As shown in fig.4.10 the diffractometer has a Bragg-Brentano $\theta - \theta$ configuration with a maximum 2θ excursion ranging from -8° and 180°. The X-Ray source is Cu Kα ($\lambda = 1.542$ Å) and the accelerating voltage can be set in the range 20÷40 KV. Diffracted rays were collected through a solid state Si:Li detector cooled by Peltier element.

4.4.2.2 Results

The typical XRD spectrum of these films is shown in fig.4.11. XRD spectrum reported in figure 4.11 shows that the obtained film is characterized by the orthorhombic β-PbO phase. Peaks have been indexed and clearly confirm that the grown polycrystalline film is made of well crystallized micrometric grains. The lack of most of the expected peaks in the spectra is due to the common orientation of plate-like micro-crystals with **c**-axis (fig.4.3-1) perpendicular to the growth substrate. This tendency of β-PbO to grow highly oriented can be explained in terms of crystal structures. As shown in fig.4.3 (2) and (3) along **b** and **a** axes there are planes that

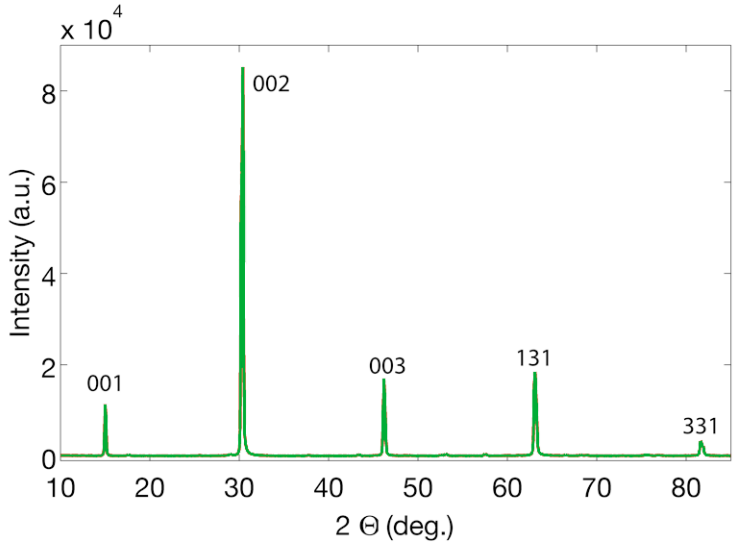

Figure 4.11: *X-ray diffraction spectra of the film. The peaks are indexed according to the orthorhombic PbO cell.*

contain both Pb and O chemical bounded. On the contrary along **c** axis there are two planes that contain only Pb atoms weakly bonded as shown in fig.4.4 (left). The result is that the β-PbO have two direction in which the grow is fast (along **a** and **b** directions) and one direction where the grow is slow (along **a** axes). When thick films are grown, plate-like micro-crystals arrange on the same plane giving rise to a film with a clear texture along the **c** axis. It should be underlined that no peaks relative to lead or to α-PbO were detected confirming that with vapor approach is possible to grow single phase polycrystalline β-PbO.

4.4.3 Photoluminescence

4.4.3.1 Experimental Setup

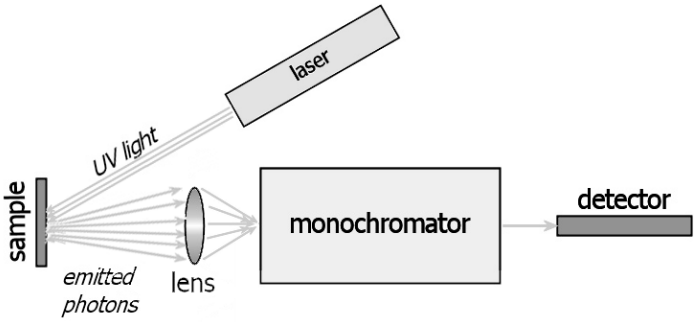

Figure 4.12: *Photouminescence setup.*

The PL setup is shown in fig.4.12. In this setup the exciting laser is a 325 nm He-Cd produced by Kimmon Electronics and rated for 200 mW. Laser beam passes through a mechanical chopper

(32 Hz frequency) controlled by a power supply allowing precise adjustments of the chopper frequency. The periodic interruptions of the light was required in order to provide the reference signal for the lock-in amplifier, which operates on the base of a phase-locked loop (PLL) device. Two optical mirrors set the beam height and a convergent lens focuses the spot on the sample mounted on the cryostat. Luminescence light is collected through two condenser lenses and focused on monochromator's input slits. PMT is used as photon to electron conversion element, the signal is amplified by a lock-in amplifier (Princeton Applied Research mod. 5209) and a RS-232 pc based interface (SPEX 1702/04) is used to program the spectrum acquirement.
The low temperature setup is made by a rotary pump (10-3 mbar), a compressor and the cryostat. Rotary pump is used to make vacuum inside the cryostat chamber, while the compressor employs a closed loop circulation of helium gas, used for sample cooling. The gas flows from the compressor to the refrigerator cryostat through a stainless steel high pressure hoses.

4.4.3.2 Results

The Photoluminescence (PL) spectra were taken under the UV irradiation of a He-Cd laser source (325 nm) in the temperature range 12–300 K (fig.4.13). No PL signal was recorded at

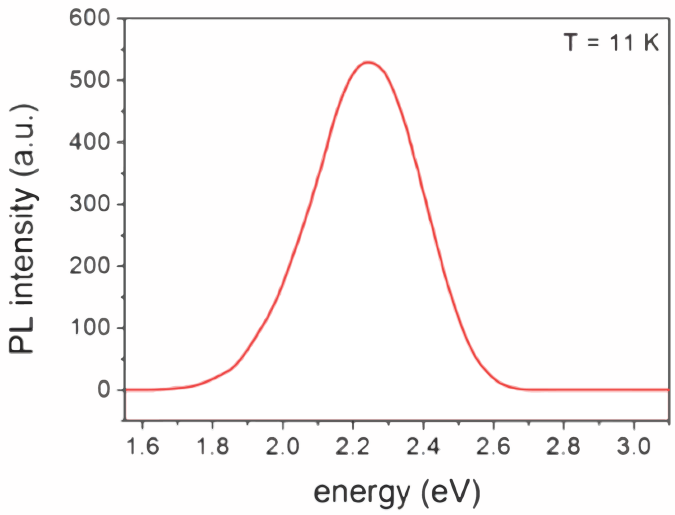

Figure 4.13: *PL spectrum taken at 15 K with a 325 nm laser.*

room temperature, indeed a strong yellow band was clearly visible at 11 K. The emission intensity again confirms the good crystallinity of the obtained films. The spectra shows no band edge emission around 2.7 eV, in accordance with the fact that β-PbO is reported to be an indirect band gap material[32].The broad emission band is constituted by at least two different emissions and it should be attributed to deep level emission, whose nature should be studied in more details

4.4.4 Electrical Characterization

For electrical and functional characterization, gold contacts were deposited on the films by sputtering technique. Current-voltage characteristics were studied in the range $-200 \div 200$ Volts and in the range $-4 \div 4$ Volts. As shown in figure 4.14 the gold sputtered contacts on β-PbO have an injecting behaviour and show a superlinear characteristic at high voltages. In the range $-4 \div 4$ V the characteristic is linear and the resistivity can be evaluated. Taking into account contact geometrical dimensions, a resistivity of about $10^{14}\Omega cm$ can be deduced, that is one order of magnitude larger than that previously reported for orthorhombic PbO and three orders of magnitude larger than that reported for tetragonal PbO[21] .

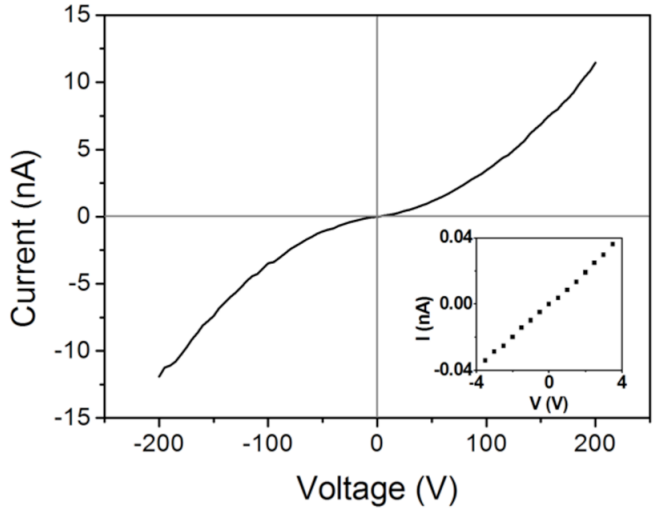

Figure 4.14: *IV characteristics of the film with gold contacts. In the range* $-4 \div 4$ *the characteristic is linear (inset).*

4.4.5 Spectral Photoconductivity

The basic principle involved in photoconductivity is that when photons of energy greater than that of the band gap of the semiconductors are incident on the material, electrons and holes are created resulting in the enhancement of electrical conductivity. This phenomenon is called intrinsic photoconductivity. It is also possible to observe photoconductivity when the energy of the incident photon is less than that of the band gap. When the energy of the photon matches the ionization energy of the impurity atoms, these are ionized, creating extra carriers and hence an increase in conductivity is observed. This phenomenon is called extrinsic photoconductivity. Spectral response of photoconductivity is the measurement of the induced current for different wavelengths. There is a close correlation between the optical absorption spectrum and the photoconductivity spectral response. For this reason from spectral photoresponse the band gap value can be extracted. Nevertheless due to surface recombination the photoconductivity spectra show, on the contrary of absorption spectra, a drop in the photoresponse at low wavelength.

The result is that the response drops down on the shorter-wavelength side even if the absorption coefficient increases in this spectral region. This because the photons of these energies are absorbed by the surface of the semiconductor where recombination velocity is higher than in the bulk[33].

4.4.5.1 Experimental SetUp

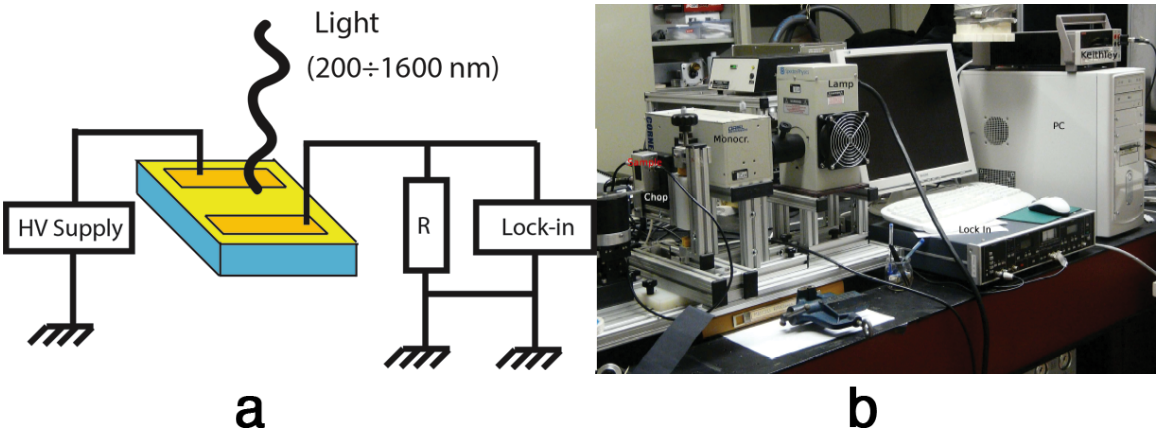

Figure 4.15: *a)Experimental setup and sample illumination geomerty. b)Picture of the real system used.*

The experimental Photoconductivity (PC) apparatus is shown in fig.4.15 (b). It consists of a light source system ORIEL Mod. 66882 suitably screened and focused, with a Quartz Tungsten Halogen-250Wlamp (on the sample, without neutral filter applied), neutral filters, a monochromator CornerStone 130TM 1/8 m Model 74000 covering the range 200–1600 nm (wavelength resolution of 3 nm), a chopper Signal Recovery Model 197 operating at 220 Hz. As shown in fig.4.15 (a) a HV power supply was used to bias the sample and the signal was measured on a load resistance by a lock-in EG&G PARK Model 5209.

4.4.5.2 Results

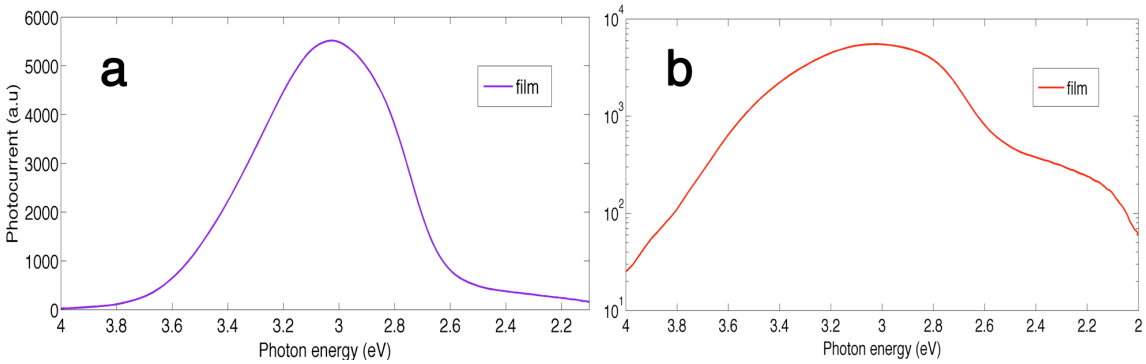

Figure 4.16: *Spectral Photoconductivity of β-PbO film in linear a) and semi-log b) scale.*

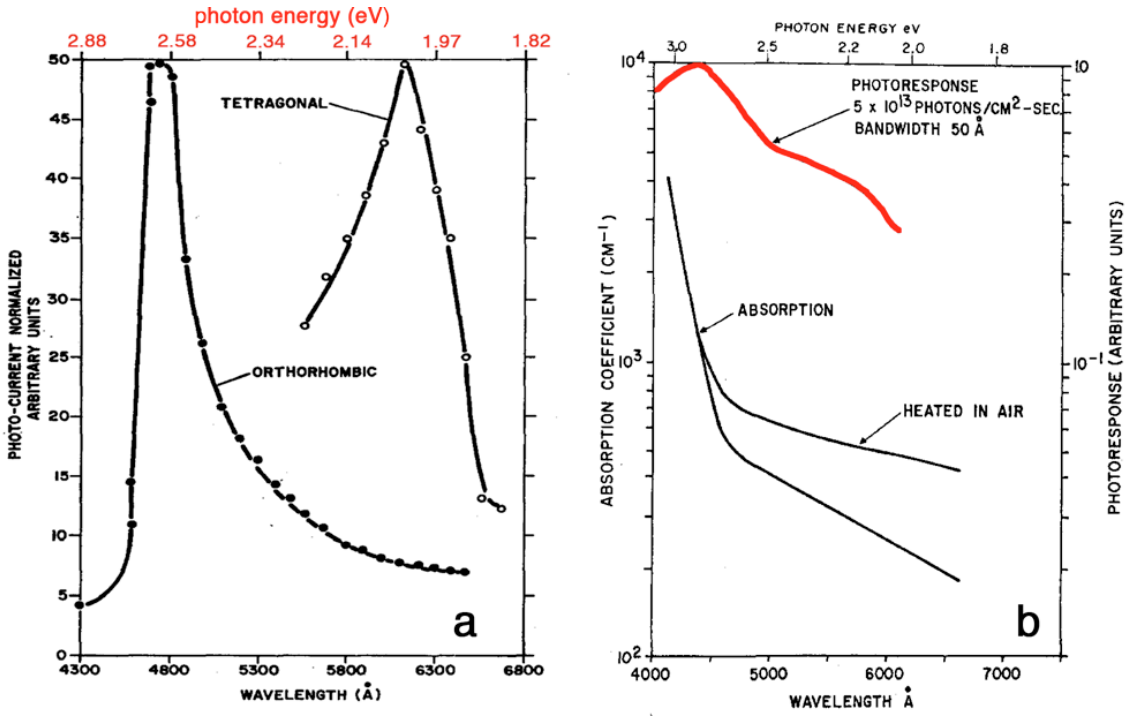

Figure 4.17: *a)Photoconductivity measured by J. Schottmiller.[21] b)Photoconductivity (red line) and optical absorption of orthorhombic PbO measured by R. C. Keezer[22].*

The spectral photoconductivity of β-PbO film is shown in fig.4.16 in both linear (a) and semi-log (b) scales. For comparison the phoconductivity spectra reported in literature by J. Schottmiller[21] and R. C. Keezer[22] are shown in fig.4.17 (a) and 4.17 (b).
The main peak in the photoconductivity response can be attributed to the band gap transition and it is centred around 3 eV. According to the method used by Keezer the band gap value can be extrapolated by the position of the dropped of 50% in the photo response: this position (fig.4.17 (a)) is around 2.7 eV according with the value of band gap reported in literature. Comparing the spectra of figures 4.16 (a) and 4.17 (a) a different shape of the photoresponse can be noted. On the contrary, there is a good agreement between the semi-log photoresponse and the photoconductivity reported by Keezer (4.17 (b) red line). If the spectrum is analysed in semi-log scale, in fact, the presence of a second broad band at lower energy can be evidenced in both the spectra. It is interesting to note that the energy position of this shoulder in the room temperature PC spectra coincides with the position of the band in the Photoluminescence spectra shown in fig.4.13 .

4.5 Transport Properties

The transport properties, in particular the $\mu\tau$ product, represent a very important parameter for radiation detectors. The $\mu\tau$ product is directly connected to the charge collection efficiency and, therefore, is connected to the quality of the material as a radiation detector. In order to collect all the generated carriers the quantity $\mu\tau E$ (E is the applied electric field) must be comparable

with the thickness of the detector. For this reason the $\mu\tau$ value is also related to the maximum thickness that can be achieved for X-ray detectors.
Several techniques are available in order to extrapolate the $\mu\tau$ product for both electrons and holes from the charge collection efficiency measure. These types of measurements are characterized by two different steps:

- Using a exciting source a large number of free carriers (e-h pairs) is created inside the semiconductor material.
- These carriers drift in the sample, due to the electric field, and are collected by the electrodes. The amount of collected carriers as function of applied voltage is recorded.

For CdZnTe material, for example, α-particles (that are mono-energetic) are normally used as exciting source and the position of the response peak of the detector spectrum is measured as function of applied voltage [34]. Other excitation sources can be used to generate carries, so that other techniques can be used to determine muxtau product, such as UV photocurrent (PC) , electron beam induced current (EBIC), ion beam induced charge (IBIC) and X-ray beam induced current (XBIC).

4.5.1 X-ray beam induced current technique

In XBIC technique [35] a X-ray beam is used to generate a large number of e-h pairs that, due to the applied electric field, are collected by contacts. As discussed in section 2.3.3 charge collection efficiency (CCE) is connected to the $\mu\tau$ product with the Hecht equation. Changing the applied voltage of the film, saturation in the induced current should be observed when the entire generated carriers are collected by electrosed. The main advantage of this technique over the photocurrent, for example, is that X-ray absorption is less sensitive to the surface of the material. This because, as discussed in chapter 2, the photoelectric absorption involve the bulk of the material and not only the surface.
The parameter of interest in this type of measurements is the induce current. This value can be calculated as the difference between the current with and without the exciting source (in this case the X-ray beam):

$$\Delta I = I_x - I_{dark} \tag{4.1}$$

where I_x was the X-ray induced current and I_{dark} was the dark current without X-ray.
The induce current is connected to ammount of generated charge that are collected that depends on the transport properties.
A. Many in 1965[56] found the relation between induce current and $\mu\tau$ product in high resistivity cadmium sulphide crystals under light ($\lambda < 450$ nm) illumination in the case of uniform carrier excitation throughout the sample.
In this case the total induced current density is given by the sum of both hole and electron current densities:

$$j_{tot} = j_p + j_n \tag{4.2}$$

These current densities are connected to the transport properties of the carriers. Therefore the total current density assumes can be expressed as:

$$j_{tot} = q\mathcal{L}E\{\mu_h\tau_h \cdot \{1 - (\frac{E\mu_h\tau_h}{L})[1 - e^{(\frac{-L}{E\mu_h\tau_h})}] + \mu_e\tau_e \cdot \{1 - (\frac{E\mu_e\tau_e}{L})[1 - e^{(\frac{-L}{E\mu_e\tau_e})}]\} \quad (4.3)$$

where E is the elctric field, τ_h and τ_e are the carrier lifetimes, μ_h and μ_e are the carrier mobilities, L is the sample thickness and $\mathcal{L}$ is the volume excitation rate. The 4.3 is called Many equation. If $\mu_h\tau_h \neq \mu_e\tau_e$ the transition between linear and saturation in the current density-electric field curves would extend over a wider range than for the case of only one carrier type.
Theoretically the induced current can be measured in both continuous and pulse mode. In the pulse mode additional information can be extrapolated from the measurement, for example the response time of the sample (that is connected also to the transport properties of the material). Unfortunately only the continuous measurements can be done with the setup used at IMEM-CNR institute. Nevertheless the main parameter of interest ($\mu\tau$ product) can be extracted from measurements of induced current in continuous mode.

4.5.2 Experimental Setup

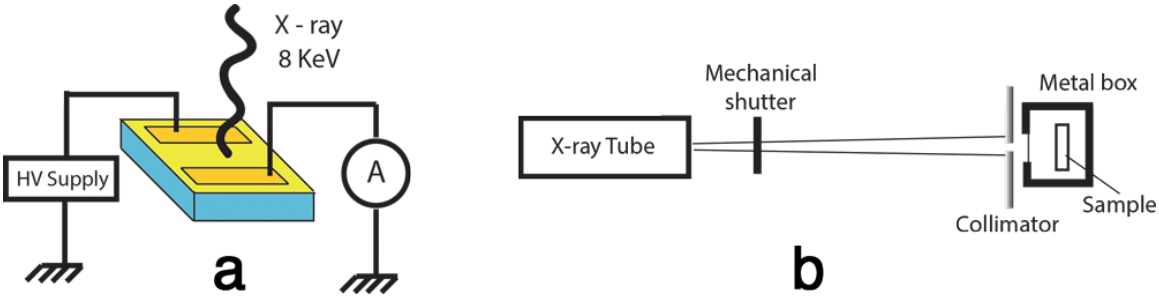

Figure 4.18: *a)XBIC measurement setup. b)Experimental setup of XBIC technique.*

The setup of the experiment is shown in fig.4.18 (a) and (b). The film was irradiated with X-ray beam continuously generated by a 40 KV X-ray tube. In this setup the intensity of the beam can be directly controlled and, for the measure, it was set in order to obtain the best induced current signal with the lowest signal to noise ratio. The induced current was measured with a pico-ammeter and a high voltage stabilized DC power supply was used in order to maintain the bias to the film. Both pico-ammeter and DC power supply are in the same instrument and all the parameters can be controlled with specific software.
For each voltage, current of the sample was recorded for 1-2 minutes. At each voltage dark current was measured, than, after some time (1 minute) the shutter was opened and the induce current was recorded. When the induce current was stable the shutter was turned off again. A mechanical shutter was used to control the on-off of X-ray beam, and therefore the rise-time and fall-time of the pulse were determined by this shutter. For this reason it was impossible to analyze the actual temporal response of the samples and all the samples were characterized by the same rise and fall-times.

4.6 Results

PbO film

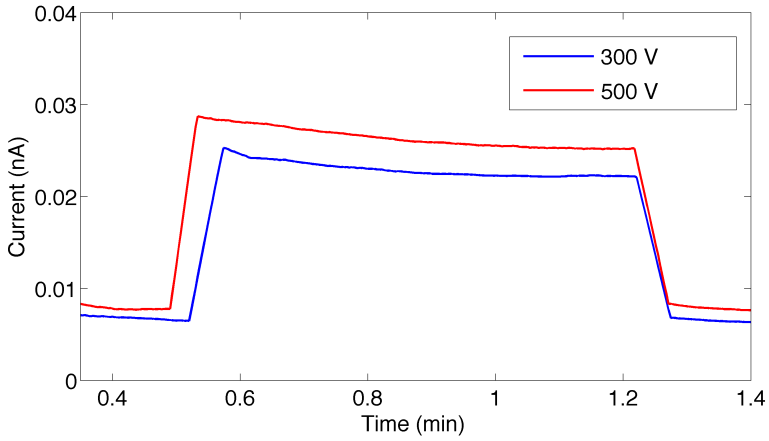

Figure 4.19: *Induced current as a function of time for 300 V and 500 V.*

The irradiation geometry of the measurement is shown in figure 4.18 (a). In this illumination geometry the X-ray beams hit the whole samples surface between electric contacts. This means that a mean $\mu\tau$ product of either carriers or at least the $\mu\tau$ product of one carrier (in the case that one carrier has much higher $\mu\tau$ than the other) was expected. This illumination geometry is not the best configuration because it doesn't allow extrapolate separately the $\mu\tau$ of single carriers.

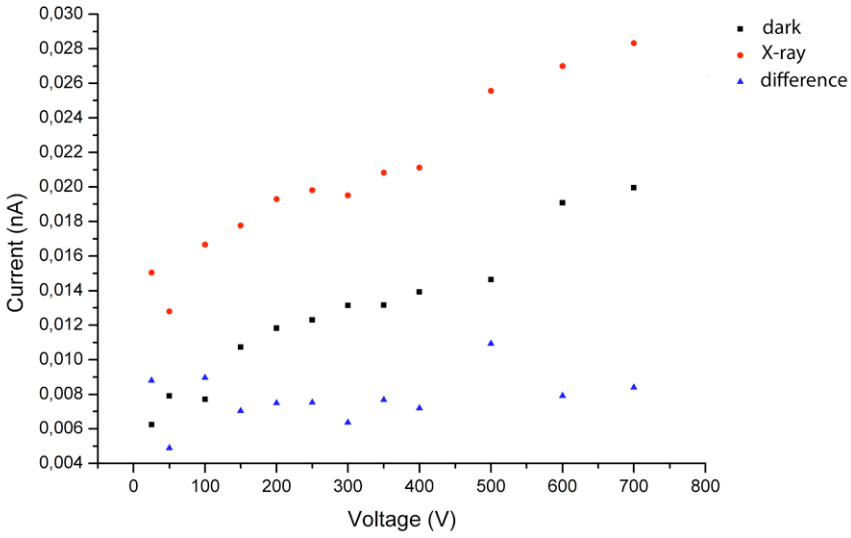

Figure 4.20: *The induced and dark current values as function of applied voltage.*

The induced current as a function of applied voltage is shown in fig.4.20. Unfortunately, as shown in the figure, no saturation in the induce current (diffrence, blue triangles) was observed

for these films even at 800V with a distance between contacts of 1 mm. This means that the $\mu\tau$ for both carriers in these films must be lower than $10^{-6} cm^2/V$ ($\mu\tau E << $ distance between contacts) confirming the very low values of $\mu\tau$ in a polycrystalline β-PbO film as calculated by Schottmiller[21] with a different technique..

CdZnTe

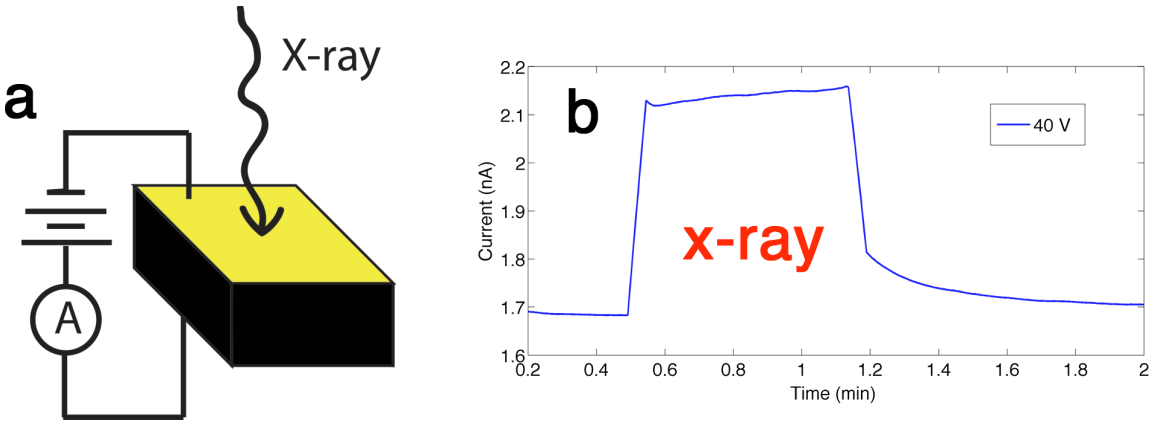

Figure 4.21: *a)XBIC setup for CZT sample measurement. b)Measured current as function of time with and without X-rays for a fixed voltage (40V).*

In order to prove that, with XBIC technique the transport properties can be measured, a standard CdZnTe material was characterized. The tested sample was a CdZnTe 040-02-b simple planar detector with gold electroless contacts. The setup of the measurement is show in fig.4.21 (a). The CZT was irradiated from the cathode surface (negative electrode). The interaction depth of few KeV is very small inside the CZT and, therefore the e-h pairs were created very close to the irradiated surface. In the configuration of figure 4.21 (a) the generated holes are immediately collected to the cathode and only the electrons contribute to the photocurrent signal. Using this illumination geometry the transport properties (in particular the $\mu\tau$ product) of only one carrier can be extracted. By changing the sign of the applied voltage also the $\mu\tau$ product of the other charge (holes) can be extracted. In fig.4.21 (b) the current-time measurement at 40V is shown. It is possible to note that when the X-rays beam was ON a increase in the current was observed. The delay of the mechanical shutter (3.2 sec) can be calculated from the rise time of the signal. It is also possible to note that a long exponential tail appears when the X-ray beam was shuttered off, as a consequence of de-trapping effects. As aspected no signal was measured when the sign of the voltage was changed. This because the transport properties of holes in CZT are very low and no signal was collected from electrodes.

The induced current as function of applied voltage is shown in fig.4.22. Saturation of the current for applied voltage above 50 V is evident. Using Many equation the $\mu\tau$ product of electrons was measured, in particular a value of $\mu_e\tau_e = 3.4 \cdot 10^{-3}\ cm^2/V$ was measured. This value is in a good agreement with the value measured with the $\mu\tau$ product measured with α-particles. This result confirms that XBIC is a very interesting technique for material characterization and in particular for the measure of the $\mu\tau$ product in high resistive semiconductors.

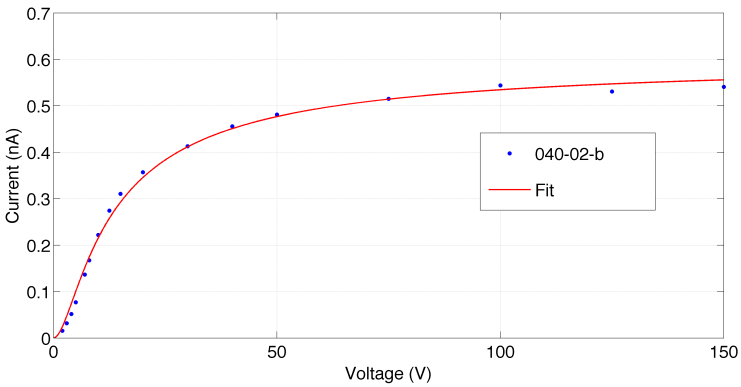

Figure 4.22: *Induced current as function of voltage for 040-02-b CZT sample (blue dots) and the data fit (red line).*

4.7 Single Crystal Nano-Ribbons of β-PbO

4.7.1 Introduction

The growth of single crystals of β-PbO is a crucial step in the study of the transport properties of the material. In particular the growth of b-PbO single crystal represents a challenge because the complexity of the phase diagram.

In IMEM-CNR institute of Parma the growth of other metal-oxide semiconductors (ZnO, SnO_2 and In_2O_3) has been developed in the last 10 years[36]. The research was especially focused in the growth of nanostructures (nano wires, tetrapods and nano-ribbons) for gas sensing applications. The interesting thing of these vapour phase grown nanostructures is that they grow spontaneously as single crystals.

So, the idea was to use the same approach also to obtain small single crystals of b-PbO and to measure their transport properties The main goal of this work was the growth of single crystals of β-PbO in the form of nano-ribbons in a reproducible and controlled way as shown in fig.4.23.

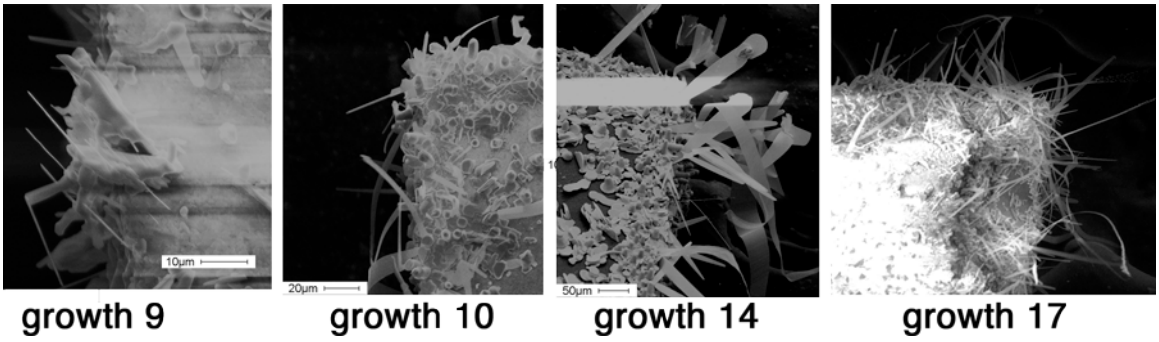

Figure 4.23: *Different growths of nano-ribbons. Several growth were done before finding the best conditions for growth.*

4.7.2 Growth

The same growth apparatus of fig.4.6 and the same growth steps of the β-PbO films were used also for the growth of nano-ribbons of β-PbO. In this growth apparatus both polycrystalline films and single crystals can be grown in the same run (following the procedure described in section 3.3.2) . The polycrystalline films and the round plate-like shape crystals grow at around 800°C (very close to the metal source). On the contrary the nano-ribbons grown at temperature around 650°C and therefore more distant form the source. Even if grown in the same apparatus,

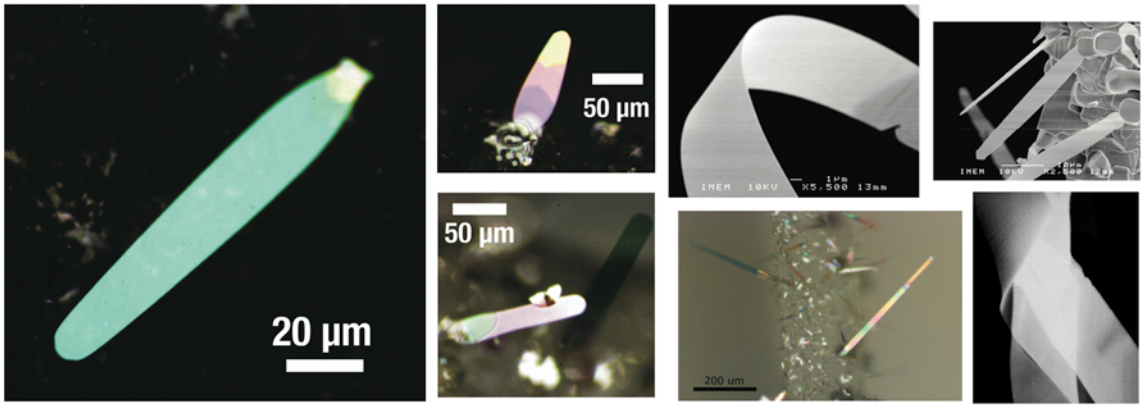

Figure 4.24: *Some images of nano-ribbons.*

plate-like shape crystals and nano-ribbons have a complete different growth mechanism.
These nano-ribbons exhibit an extreme length to thickness ratio as shown in fig.4.24. The thickness is typical 50-100 nm (this is the reason why the are considered nano-structures), the width and length are respectively in the range 10÷50 µm and 50÷500 µm. The macroscopic length and width of these nano crystals allows also the investigation with the optical microscope (figure 4.24). The differences in the colour that is possible to see in figure is due to small changes in the thickness of the ribbons along the length and/or to light interference in bended structures. Finally due to the two macroscopic dimensions, it was possible also to manipulate a single nano-ribbon and put it on special supports (substrates) for making structural, optical and electrical measurements on the single structure, as will be shown later.

Growth mechanism

In order to explain the self-assembly growth of nano-ribbon structures a growth mechanism based on experimental observations is proposed in this section. The growth steps are sketched in fig.4.25 and can be summarize as follow:

- a) In the first step of growth, re-condensation of Pb droplets on the alumina substrates occurs. Due to the higher distance from the metal source these droplets are smaller than those closer to the source. This because the nucleation critical radius results smaller at lower temperature. The droplets radius at 650°C is less than $1 \div 2\,\mu m$ (as shown in fig.4.25 (a))

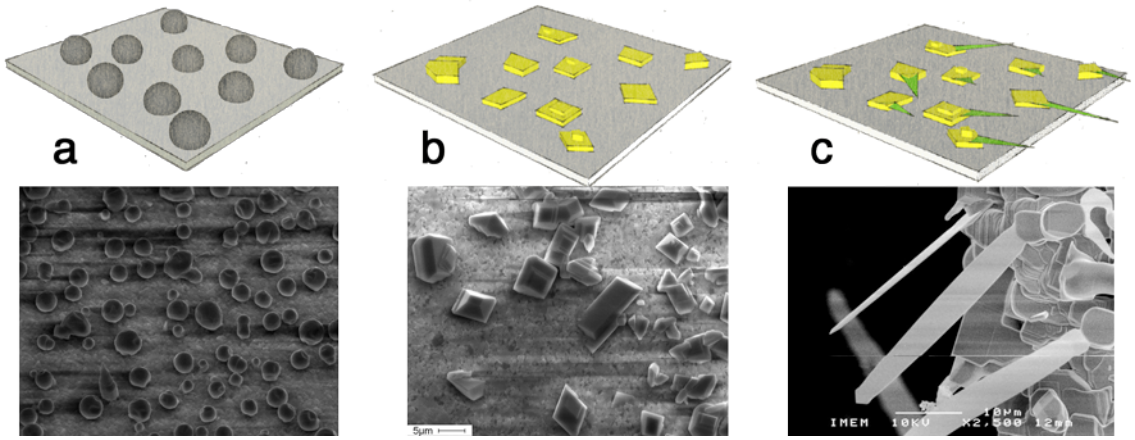

Figure 4.25: *Growth steps of the β-PbO nano-ribbons.*

- b) In the second step of growth, when the oxygen-argon mix is fluxed, the oxidation of the droplets occurs. At this temperature the crystals result with faceted shape (fig.4.25 (b)). The density of these crystals is lower than at higher temperature due to the lower number of re-condensated lead drops.
- c) The edges of these crystals are the nucleation centers for the growth of nano-ribbons (fig.4.25 (c)).

The growth of nanostructures occurs in the final part of the growth; this happens when two fundamental conditions for the growth of such anisotropic nanostructures are satisfied:

1. Local supersaturation in the vapor phase is high enough.
2. Some favorable nucleation points (with high surface energy) such dislocations, defects and edges are present.

When the oxygen start to be fluxed the vapor phase over the substrates at 650°C is in high Pb excess and strongly limited by low oxygen concentration (it is mainly consumed in the oxidation of Pb in the source and Pb deposited upstream). In this low supersaturation condition droplets are transformed in solid crystals of β-PbO (accordingly to the right diagram in Figure 4.2) with faceted shape. Further on during the last stage of the growth, while Pb vapour is slightly decreasing and oxygen increasing (most of upstream Pb is already oxydized), supersaturation reaches its maximum and both the conditions for nanostructures growth are satisfied. β-PbO nanoribbons hence start growing from some of the β-PbO faceted crystals edges.

4.8 Nano-Ribbon Characterization

4.8.1 Morphology

Film morphology was studied by means of FEG-SEM Jeol - 6400F (fig.4.24) and of SEM Philips 515 (fig.4.25). The optical characterization was made using a NIKON Microfot-FXA optical microscope (figure 4.24).

4.8.2 TEM Diffraction

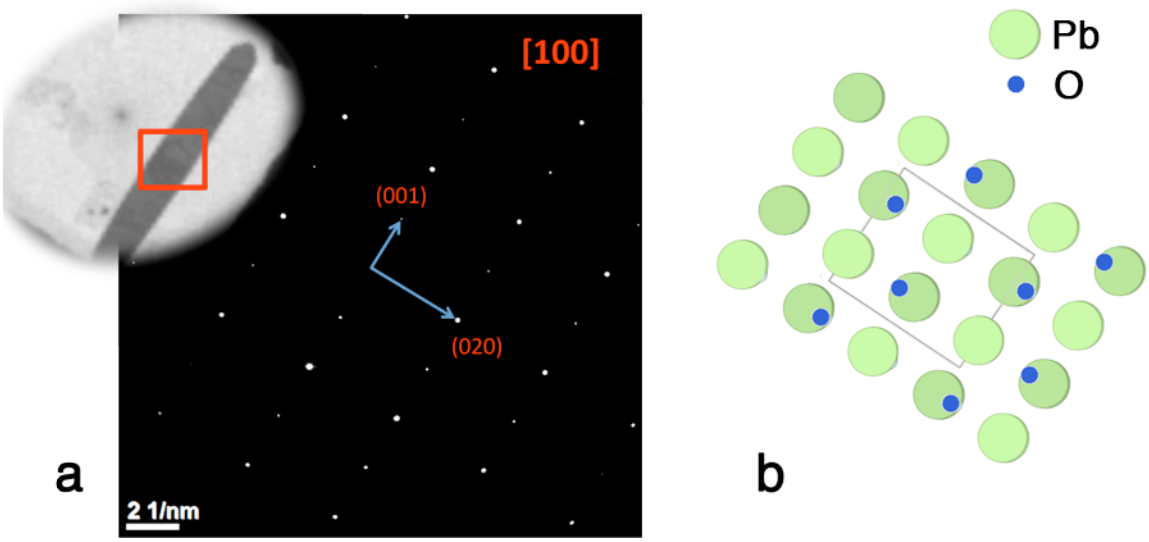

Figure 4.26: *a) TEM diffraction patter of single nano-ribbon. b)PbO Orthorhombic crystal cell solved by the diffraction pattern.*

A TEM diffractions were performed on single nano-ribbons deposited on the standard patterns grids. The TEM diffraction was performed with JEOL 2200 FEG [200KeV] microscope at IMEM-CNR thanks to Dr. Laura Lazarini and Enzo Rotunno. The diffraction pattern of a single nano-ribbon and the image of the nano-ribbon investigated are shown in fig.4.26 (a). As discussed also for the polycrystalline films, β-PbO shows always some favorable direction of growth, in particular the fastest one is the <001> and, for this reason, normally β-PbO grows with strong orientation (**c** axes orthogonal to the substrate plane). This tendency is also more evident in the case of nano-ribbons in which the length to thickness ratio results extremely high (1000/1).
As shown in fig.4.26 (a) in the **a** axis <001> the growth of nano-ribbons is very fast followed by growth along the **b** axis <020>. Contrariwise, due to the weak bonding between two Pb layers, the growth along the **c** axis <100> results very slow. The small difference between the growth velocity along **a** and **b** directions can be explained in terms of chemical bonding length. As shown in fig.4.4 (right) along the **a** direction the length of bonding (2.21 and 2.22 Å) is slightly lower than the length of bonding along **b** direction (2.49 Å).

4.8.3 Photoluminescence

With the same setup used for polycrystalline films (section 3.4.3) the Photoluminescence (PL) spectra of a single nano-ribbon placed on a glass substrate were measured. PL spectrum is shown in fig.4.27. Also for single nano-ribbon no PL signal was recorded at room temperature. At 11 K a strong yellow emission was observed in the position of the nano-ribbon. The emission intensity, also in this case, was very high confirming the good crystallinity of the obtained structure. The spectra shows no band edge emission around 2.7 eV according to the indirect band-gap of the

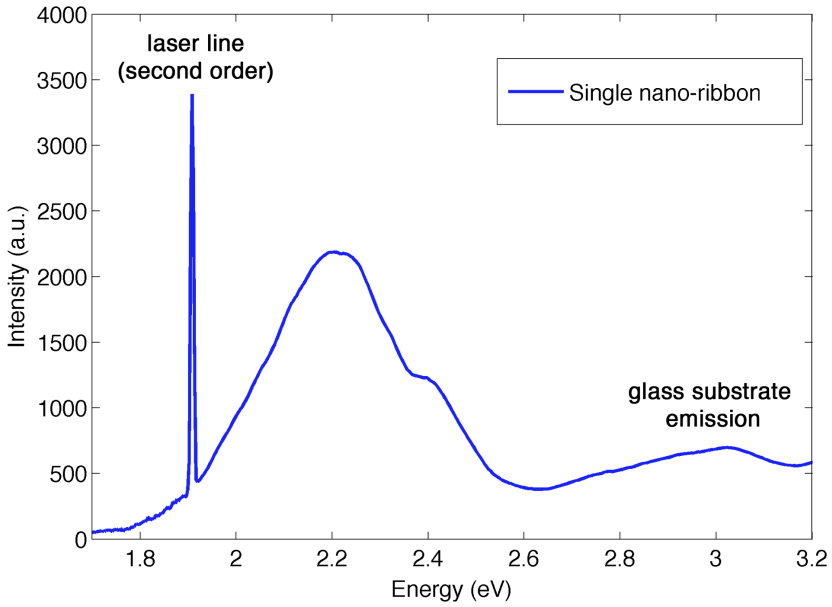

Figure 4.27: *PL spectrum of single nano-ribbon taken at 11 K with a 325 nm laser.*

material. The broad emission band is constituted by at least two different emissions centered at 2.2 and 2.4 eV and, as in the case of films, it should be attributed to deep level emission. Even if in the case of the nanoribbon, the presence of two different emissions results more evident, however, the emission band in the nanoribbon and in the film look quite similar.

4.8.4 Electrical Characterization

Electrical characterizations of single nano-ribbons were done in order to measure the resistivity of the material. Single nano-ribbons were placed on special glass substrates with gold evaporated contacts. As shown in fig.4.28 these substrates had two independent small gold contacts separated by a 50 μm space. The nano-ribbon was placed orthogonal to these two contacts (fig.4.28). Small drops of silver epoxy were placed on the two terminal parts of the ribbon in order to guarantee the stability of the contacts. The electrical contact is assumed to be between gold and nano-ribbon.

For each sample a UV induced current test was done in order to check the electrical connection of the nano-ribbon and gold contacts. As shown in fig.4.29 (right) UV lights induces current signal that can be measured confirming the electrical connection between nano-ribbon and substrate.

Nano-ribbon the current-voltage characteristic was studied for several samples in the range -400 $\div$ 400 Volts and a resistivity in the order of $10^8 \Omega cm$ was determined, taking into account nanoribbons dimensions as measured with SEM. The typical IV characteristic is shown in fig.4.29 (left). The characteristic is almost linear, even if an injecting behaviour is evident, with a close similarity with the case of PbO films. It was impossible to measure the I-V characteristic at low voltages due to the small values of currents.

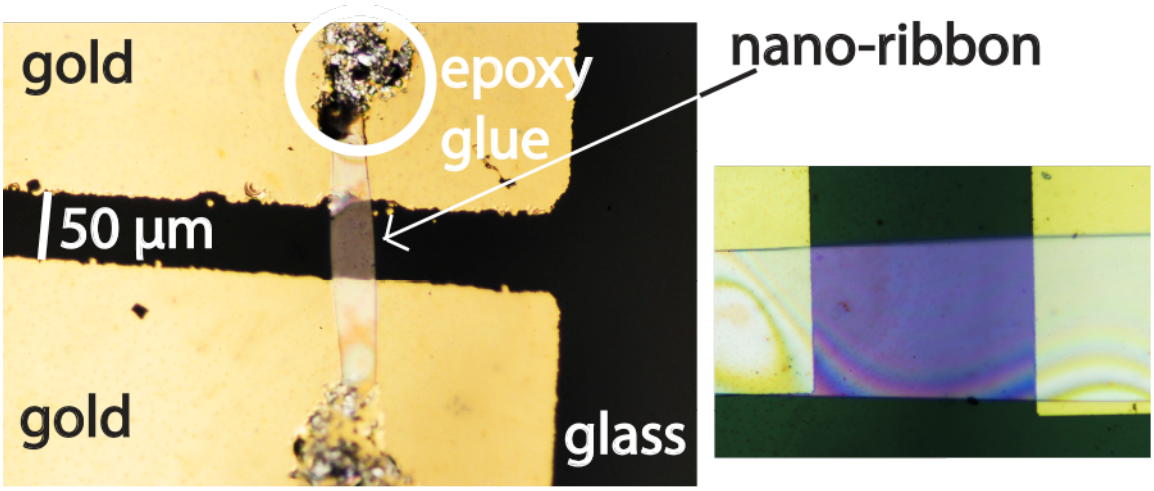

Figure 4.28: *Single nano-ribbon on the glass substrate with gold contacts.*

4.8.5 Photoconductivity

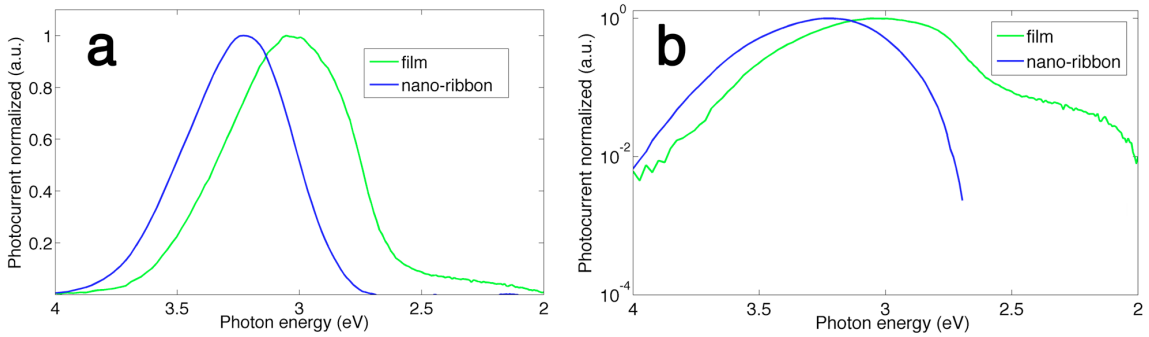

Figure 4.30: *Spectral Photoconductivity of both polycrystalline film and single nano-ribbon plotted in linear a) and semi-log b) scale.*

With the same experimental setup used for polycrystalline films Photoconductivity spectra of single nano-ribbons were measured (at room temperature). The comparison between the photoconductivity response of film and single nano-ribbon is shown in fig.4.30. It is possible to observe immediately that the spectra have two main differences:

- The centre of the main absorption peak for nano-ribbon is shifted at higher energies. This shift in the band gap absorption energy can't be explained in terms of quantum confinement because , considering the effective mass of carriers, quantum confinement effect should appear with dimensions in the order of few nanometers.
  The shift can be explained only considering the differences in the surface/bulk absorptions. In particular in the nano-ribbon the difference between bulk and surface is fleeting in comparison with the film and therefore a different shape in the photoconductivity may be expected. The absorption of the nano-ribbon is always dominated by the surface effects due to the small thickness of the sample, therefore the drop of the photoresponse results

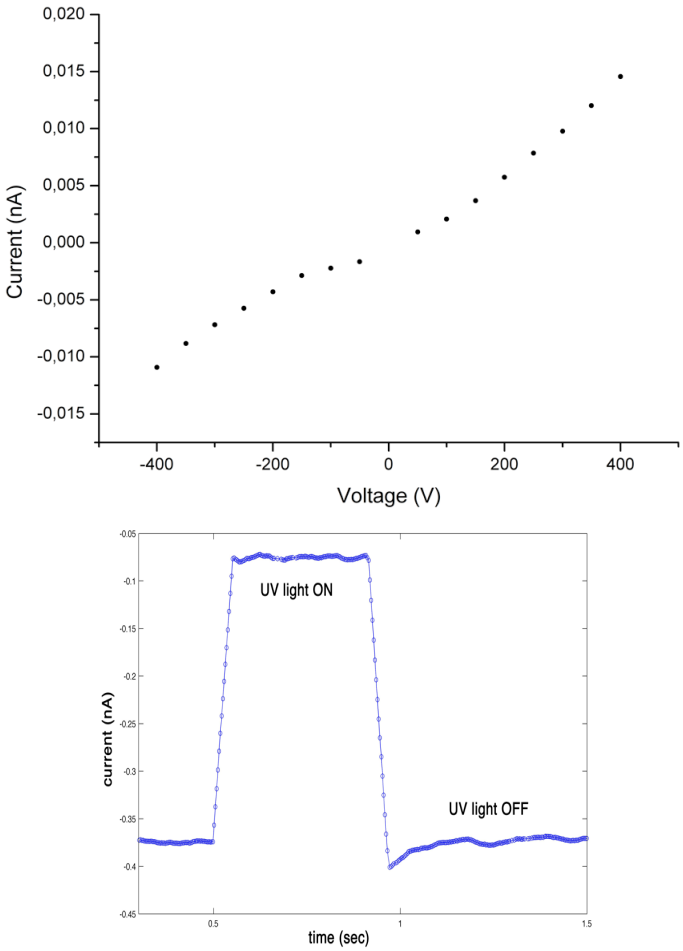

Figure 4.29: *Typical IV characteristic of a single nano-ribbon measured at 300K (Right). UV induced current on the nano-ribbon contacted to the glass substrate (left)*

shifted at lower wavelengths in comparison with the film. For the film at low wavelength tha absorption coefficient increases but the drop of photoresponse is dominated by the effects of the surface. On the contrary in the nano-ribbon the photoresponse is more sensitive to the increase of the absorption coefficient, this because, due to the small thickness of the ribbon, the surface effect appears at much lower wavelengths. The final result is that the peak results shifted at lower wavelengths.

- The second broad band at lower energy of the film spectrum was not observed in the nano-ribbon response. As shown in fig.4.30 (b) for nano-ribbon it was impossible to measure the photoresponse at energies lower than 2.6 eV. This because the photoresponse signal was too low to be measured.

4.8.6 Transport Properties

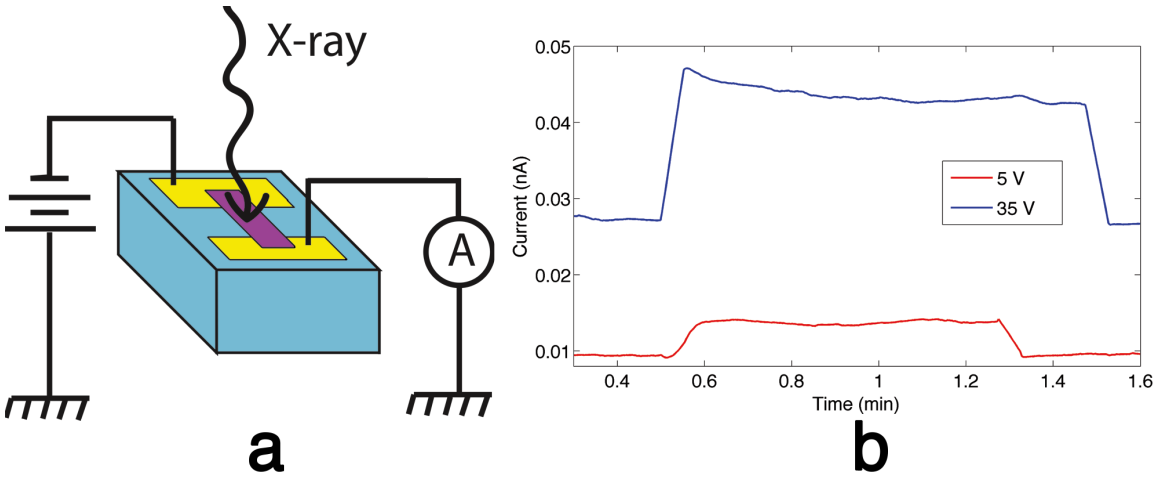

Figure 4.31: *a)Irradiation geometry for XBIC on single nano-ribbon (marked with purple). b)X-ray induced current for two different voltages 5 and 35 V.*

Using the same setup described in section 3.5.2, X-ray beam induced current (XBIC) technique was used in order to evaluate the transport properties of a single nano-ribbon. The same substrates and the same electrical characterization techniques were used (fig.4.28). Despite the small thickness of the nano-ribbon (less than 100 nm), the absorption was enough to produce a measurable signal as shown in fig.4.31 (b).

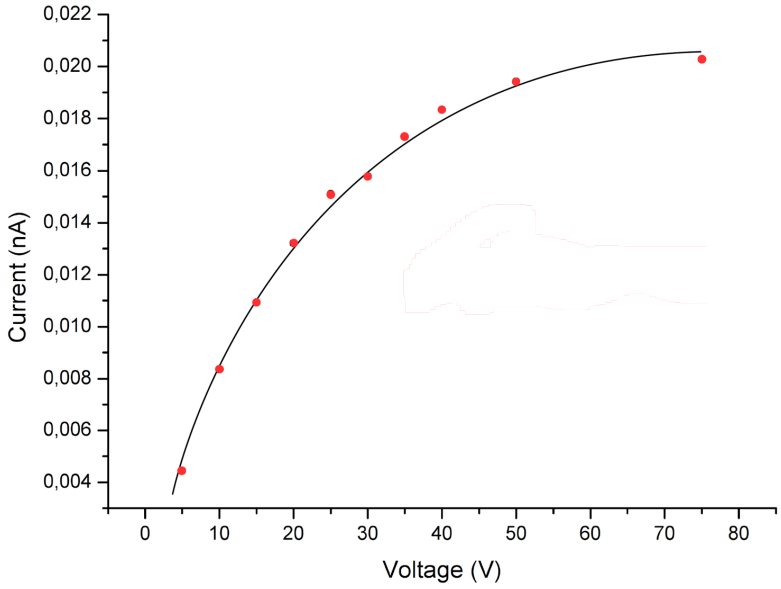

Figure 4.32: *Induced current as function of voltage for a single nano-ribbon (red dots) and the Hecht fit of data (black line).*

The fist measurement was made with the irradiation configuration of fig.4.31 (a). In this configuration, as discussed in section 3.6, the $\mu\tau$ product for single carrier cannot be extracted.

The induced current as function of applied voltage is shown in fig.4.32 (red dots). From this measurement it is clear that, on the contrary of β-PbO films, saturation in the induced current appears at high voltage values. This is a very good result because for the first time saturation in the induced current in β-PbO sample is observed. This means that, fitting data with Many equation, the $\mu\tau$ product can be extrapolated. This fit is shown in fig.4.32 (black line) and a $\mu\tau$ value of $2 \cdot 10^{-5}\, cm^2/V$ has been obtained. This value is considerably higher than the value found bt Schottmiller ($1 \cdot 10^{-9}\, cm^2/V$)[21] and it is much more similar to the value found by Keezer ($4 \cdot 10^{-4}\, cm^2/V$)[22].
Due to the irradiation geometry both electrons and holes contribute to the induced current. However, due to the expected difference in the effective mass between holes and electrons, the main contribution to the detected signal is expected to derive from electrons and, thus the determined μτ can be associated to these carriers.

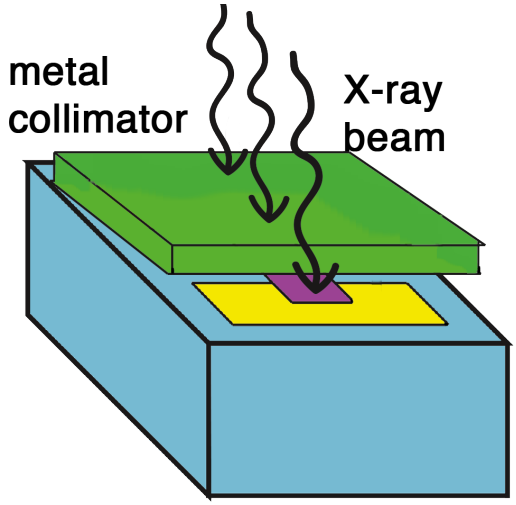

Figure 4.33: *Irradiation geometry of single nano-ribbon with metal collimator.*

In order to extrapolate the $\mu\tau$ of both holes and electrons a different irradiating geometry must be used. In particular the generation of the free carriers must be done very close to one electrode (as discussed in the case of CZT), so that only one carrier type drifts along the sample polarizing in the opportune way the sample. This measurement results very difficult in our case, because the sample length is only 50 micron and a very collimated source would be required, such as the one available in a synchrotron facility, where very small X-ray beam size can be achieved. Despite this, we tried in any case to extrapolate the single transport properties by means of a metal shield placed in such a way to cover the main part of the active channel of the device. The collimator was fixed on the nano-ribbon substrate with the help of an optical microscope; by an optical microscope equipped with a digital camera it was determined the width of the nano-ribbon outside the metal shield.

In this configuration, simply by changing the polarity of the electric field both of the μτ of both electrons and holes can be extracted. The induced current as a function of the voltage for the two polarizations are shown in fig.4.34 (a) and (b). Fitting the two measurements values

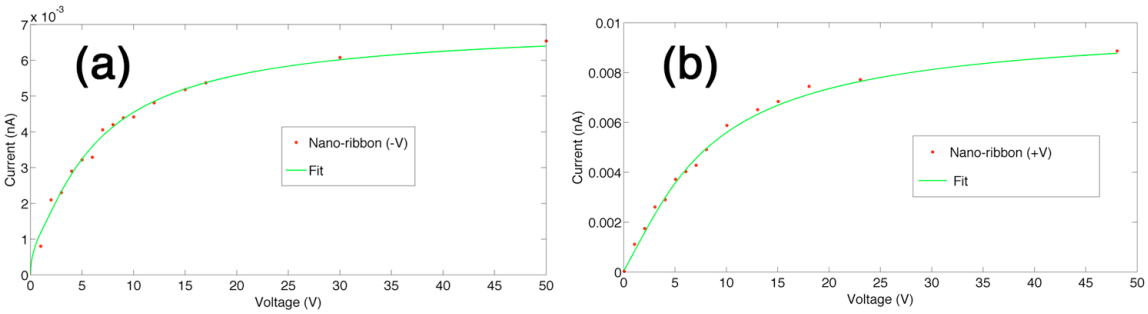

Figure 4.34: *The induced current as function of voltage and the fit for two different polarities using the experimental setup shown in fig.4.33.*

of $\mu_e\tau_e = 4.8 \cdot 10^{-5}\ cm^2/V$ and of $\mu_h\tau_h = 2.5 \cdot 10^{-5}\ cm^2/V$ of can be extracted. These value are quite different confirming that, irradiating close to one electrode, the single $\mu\tau$ products of single carriers can be measured. Moreover, the obtained value for $\mu_e\tau_e$ is larger than the obtained value for $\mu_h\tau_h$, as expected from energy band structure. Unfortunately using our setup it was impossible to collimate the X-ray beam precisely in a small enough region close to the electrode. Thus, we think that the obtained values of $\mu_e\tau_e$ and $\mu_h\tau_h$ are not fully reliable and the measurement should be repeated under more controlled conditions.

4.9 Conclusion

4.9.1 Conclusion Film

Lead oxide films were grown by the vapor phase starting from metallic lead and oxygen. Only β-PbO (orthorhombic phase) was formed. Film thickness up to 20 microns was reached up to now. Even if this is enough to efficiently stop x-ray radiation exploited by a large part of medical applications, the film thickness should be increased to about 100 microns. The films were oriented along the c axis and showed a few micrometer grain dimension that is compatible with the realization of a pixel structure in the order of 100 µm. Films showed very high resistivity, thanks to the higher energy band gap of orthorhombic phase with respect to tetragonal phase. The good film crystallinity was also demonstrated by an intense PL emission. Both PC and PL spectra showed the presence of a broad deep level band. Films showed a clear increase in current as a consequence of X-ray irradiation with no pile up or memory effects. No transport properties can be extracted from the XBIC measurement confirming the poor transport properties of polycrystalline films as calculated by Schottmiller[21].
Finally the XBIC proves to be a very interesting technique for studying the transport properties of high resistive semiconductor materials. This technique can be developed in order to obtain more information such as the role of detrapping in CZT crystals.

4.9.2 Conclusion β-PbO Nano-Ribbon

Single crystals of β-PbO were grown by vapor phase using the same setup used for films. This crystals are in form of nano-ribbons with an extremely high thick-to-length ratio (1000/1): the

width and length are respectively in the range 10÷50 µm and 50÷500 µm and the thickness is typically 50-100 nm. TEM diffraction confirms that these nano-ribbons are single crystal of the β-PbO phase. Single nano-ribbon can be manipulate and put on special substrates and and electrically contacted. The PL response of single crystal was very similar to those of the film. On the contrary the PC spectra shown a shift in the main response peak in comparison of those of the film. This shift can be explained considering the difference between surface/bulk absorption and recombination in the films and in the nano-ribbons.

With XBIC technique for the first time the saturation in the induced current was observed. By fitting the measurements a $\mu\tau$ value of $2 \cdot 10^{-5}\ cm^2/V$ was obtained when all the sample was irradiated. This value can be attributed to electrons considering the band structure of β-PbO. In any case this value is considerably higher than the value found by Schottmiller ($1 \cdot 10^{-9}\ cm^2/V$)[21] and it is much more similar to the value found by Keezer ($4 \cdot 10^{-4}\ cm^2/V$)[22].

We tried in any case to extrapolate the single transport properties by means of a metal shield placed in such a way to cover the main part of the active channel of the device. In this configuration and changing the polarity of electrode, two different saturations were observed. But this effect was not enough to separate completely the two contributions.

The obtained values of $\mu_e\tau_e$ and $\mu_h\tau_h$ are not fully reliable and the measurement should be repeated under more controlled conditions. In order to measure $\mu_e\tau_e$ and $\mu_h\tau_h$ a very collimated source would be required, such as the one available in a synchrotron facility, where very small X-ray beam size can be achieved.

Chapter 5

CdZnTe based detectors

5.1 Introduction

In comparison with PbO, CdZnTe (CZT) is a much more well established material, and nowadays it represents one of the standard materials for radiation detection applications. CZT based detectors are indeed already available on the market and they start to be integrated into conventional industrial and medical systems.
The unique properties of CZT represent the driving force of the continuous development in the material quality and in the detectors preparation.
The most interesting and important properties of CZT are:

1. High average atomic number $Z \simeq 50$
2. High density (4 mm of material are enough to stop 180 KeV energy photons)
3. High resistivity.
4. Band gap value of 1.6 eV (for 10% of Zn) that allows the operation at room temperature.
5. Good electron transport properties.

Despite these good properties the research on this material is still under way and some issues are still open:

- The incomplete charge collection due to the trapping of holes.
- Difficulty to growth large single crystals parts (now the standard dimensions of commercially available CZT detectors is 20 mm x 20 mm x 5 mm).
- The crystal quality is often affected by defects: Te inclusions, grain boundaries, dislocation, twins and/or cracks.
- The uniformity of material properties within the volume of the crystals.

Moreover other issues are connected to the device fabrication:

- CZT is fragile material, especially near the edges and the cutting and polishing processes are difficult.
- CZT properties change with temperatures higher then 100-150 °C.
- The resistivity of surfaces are alway less than the resistivity of the bulk.
- Poor adhesion of metal contacts on CZT.
- Impossibility of making ohmic contacts.

These problems has limited up to now the diffusion of the CZT technology on the market and strong efforts are continuously done to increase the quality and the dimensions of the CZT crystals, and hence to reduce the cost of each detector.
From the chemical point of view $Cd_{(1-x)}Zn_xTe$ is a semiconductor compound in which, due to the perfect miscibility of CdTe and ZnTe, the Zn fraction x can be varied between 0 and 1. In particular the increase of zinc fraction increases the band gap energy E_g following the relation[37]:

$$E_g(x) = 1.51 + 0.606 \cdot x + 0.139 \cdot x^2 \ eV \tag{5.1}$$

Therefore the value of band gap can be varied from 1.5 (CdTe band gap) to 2.2 eV (ZnTe band gap). As discussed in chapter 3 the band gap energy is very important for the spectral performance of detectors. Specifically, it must be a compromise between two different aspects: E_g must be as low as possible in order to reduce the ionization energy (increasing the energy resolution) and, on the other hand, it must be high enough to reduce the number of thermal generated carriers. The addiction of Zn in CdTe has also other benefits, such as increasing the energy of defects formation and enhancing the mechanical proprieties of the lattice[38][40].
At IMEM-CNR institute crystals of $Cd_{0.9}Zn_{0.1}Te$ are grown; 10% in Zn to Cd substitution is the standard composition of CZT that is usually reported in literature.

5.2 Crystal growth of CZT

The performance of CZT based radiation detectors are directly connected to the quality of CZT material. The growth of high resistivity ingots, with a sufficiently good quality in order to ensure high efficiency radiation detection, still remains an open challenge. The goal is to obtain ingots with large single crystal grains, ideally free from extended defects and with high resistivity, maximizing the yield (the quantity of material that can be used to realize radiation detectors) and, hence, reducing the production cost.
For CZT growth several technique were developed during the last 20 years. Nowadays the growth of CZT is done mainly by two techniques: Bridgman method and Travelling Heater Method (THM) techniques. These two growth techniques are completely different and it is difficult to state which is the best for growing CZT ingots. The complete description of both techniques is out of the aim of this thesis and can be found in some good textbooks ([40]) . The following discussion will be focused only on the growth technique used at IMEM-CNR institute of Parma, i.e. a modified version of the standard Vertical Bridgman technique.

5.2.1 Boron encapsulated vertical Bridgman

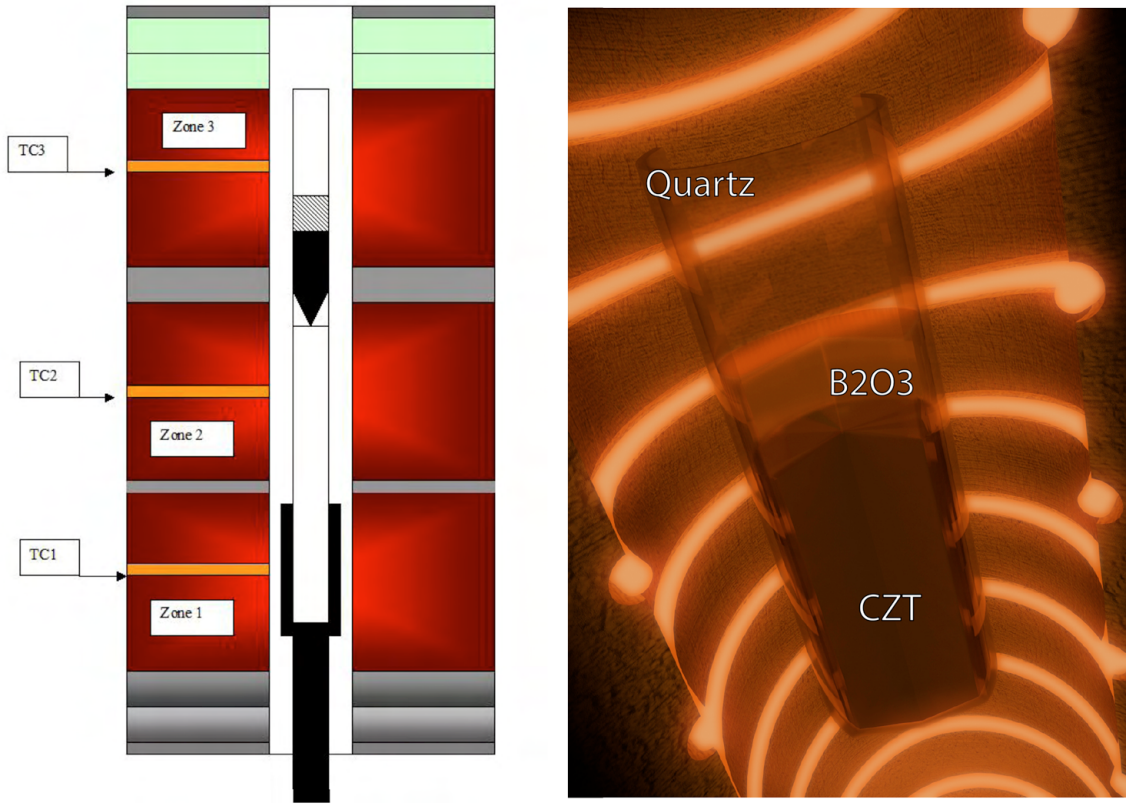

Figure 5.1: *Scheme of the Bridgman furnace used at IMEM (left), image of the CZT ingot surrounded by boron-oxide encapsulant (right).*

Crystal growth of CdZnTe ingots at the IMEM-CNR is performed using an innovative Bridgman technique developed in the institute since 2007[41]. The technique is basically a vertical Bridgman where the ampoule is not directly sealed ("closed ampoule" configuration), but in which the loss of the elements is avoided using an encapsulant B_2O_3.
In order to obtain high quality crystals, CdZnTe is synthesized starting from high purity elements (7N). Direct synthesis of polycrystalline CdZnTe charge is carried out at high pressure (20-40 atm) of inert gas (argon) while all the elements are encapsulated by a layer of liquid B_2O_3 [42]. Encapsulation helps to maintain the stoichiometry between the elements. Synthesis is performed in a quartz or Pyrolytic Boron Nitride (PBN) crucible. The melting of B_2O_3 (that occurs at 600°C) results in a complete encapsulation of the elements before any loss of the elements (in particular Cd) occurs. After the synthesis, the encapsulation layer can be easily removed using de-mineralized water (B_2O_3 is highly soluble in water). The synthesized polycrystalline charge material is then placed in a quartz ampoule, located in the upper and hotter part of the furnace [43].

The furnace currently used at IMEM is set for the growth of ingots up to 3 inches but the chosen crystal size is usually 2 inches. The furnace has three temperature zones, as shown in figure5.1 (left), with a thermal gradient of 10 °C/cm at the growth interface. The ampoule is

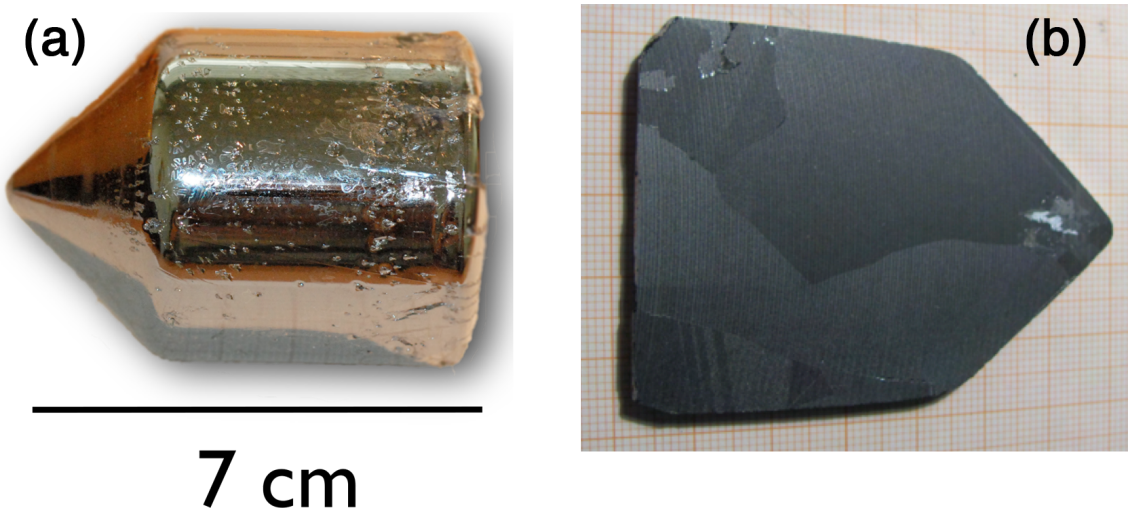

Figure 5.2: *a) 2 inches ingot growth at IMEM-CNR insitute, using B_2O_3 very smooth surface can be obtain due to the no interaction between ingot and ampoule. b) Ingots with large single crystal grains can be grown at IMEM-CNR.*

then moved along the gradient axis with a speed of 1-2 mm/h toward the cold part of the furnace. On the contrary of standard Bridgman technique and similarly to the synthesis of polycrystalline charge, the used ampoule is not sealed because the charge is protected by a melted boron oxide encapsulating layer. This avoids the presence of impurities that are usually associated with the ampoule sealing procedure. The adhesion of B_2O_3 on the charge surface is produced by means of a moderate pressure (5-10 atm) of inert high purity gas.
Beside the higher purity provided by the boron encapsulation, an additional control on the stoichiometry is added by the lack of a free volume during the growth. Moreover, the B_2O_3 encapsulation prevents the contact between the ampoule and the ingot (fig.5.2 (a)). It's proved that B_2O_3 forms a thin molten layer that surrounds completely the charge during the growth, as schematically illustrated in figure5.1 (right).

5.3 Detector preparation

In order to test the material quality of the CZT grown at IMEM-CNR institute, several detector samples were made during this work. The aim of these characterizations was to study different properties of the grown material: resistivity, metal-semiconductor contact, transport properties and spectroscopy performance. For testing the material, ingots were cut and simple detectors with planar electrodes were prepared and characterized. The detector preparation will be discussed also in chapter 6.

5.3.1 Cutting

The 2 inches ingots grown at IMEM institute (shown in fig.5.2) are normally cut into wafers perpendicular to the growth axis. In this way the effect of Zn segregation (that results in a not-uniform concentration of Zn along the growth axis) can be reduced. Several ingots were first

cut into wafers and than cut again into smaller samples with rectangular shape. The cutting process is ideally a trivial procedure, but on the contrary it is one of the critical steps in the realization of CZT devices. Every cut, in fact, produces several damages that may have a large influence on the performances of the sample as a radiation detector. For the wafer cutting a diamond saw is used; for cutting the wafer into smaller samples a diamond wire saw is used. The diamond saw for cutting ingot is a standard machine for semiconductor industry with a 0.3 mm thick diamond circular blade. The wire saw is a South Bay Tech. machine that allows a fine regulation of the weight to be applied on the wire and by means of this tool an extremely soft cut can be made.
The samples used for the characterization of the ingots have usually areas of 7 mm x 7 mm or 5 mm x 5 mm, therefore many devices can be obtained from a single wafer. Before cutting wafers optical and IR transmission inspections are normally carried out in order to select the usable parts of wafers.

5.3.2 Mechanical polishing

The obtained samples are then mechanically polished. The aim of this process is to remove the parts of the crystal that were damaged during the cut. Normally a 100-150 µm layer of material must be removed in order to remove all the damaged parts.
Polishing technique consisted of a rotating plate where sandpapers with different grains were mounted. The system was equipped with bi-distilled water supplier in order to have the best lubrication on the sandpaper without introducing any type of impurities. We developed a standard procedure for mechanical processing that is working very well with CZT crystals.

- In the first step a paper with relatively large grain (p2500, 8.4 µm of average particle diameter) was used. The aim of this first stage was to remove a relative thick layer of material in order to eliminate the existing contacts and eventually the scratches present on the surfaces.

- In the second step p4000 SiC grains sandpaper (5 µm of average particle diameter) was used. This step is fundamental for subsequent machining, with p4000 all the remaining scratches must be eliminated. For this reasons this step is the longest one.

- After the lapping (process with sandpaper), the polishing procedure started. The sandpaper was replaced by polishing cloths. A set of abrasive diamond suspension was used with diameters ranging from 3µm down to 0.1 µm. The entire process required a usually one day for the two sides of each sample.

- After the polishing and the mechanical polishing the sample was cleaned with two hot solvents: acetone (10 minutes at boiling temperature) and isopropanol (10 minutes at boiling temperature).

At the end of the polishing process the samples have mirror surfaces. At the end of this process the samples are cleaned with hot solvents (boiling temperature): toluene, isopropanol and acetone.

5.3.3 Contact deposition

The development of a reproducible and high performance contact deposition technique met some difficulties. The main problems are connected with CZT characteristics. CZT is fragile, especially near the edges, and a particular care has to be taken when techniques, like photolithography that requires contact between the sample and the mask, with a consequent pressure on the sample, are used. Moreover the poor adhesion of metals on the CZT surface is well known. This limit cannot be overcome with a thermal annealing, as it's usually done for other materials, because of the detrimental change in CZT properties with temperatures higher then 100-150 °C.
At IMEM-CNR institute the electrical contacts on CZT are deposited using a wet technique called "electroless depostion". In this technique an aqueous solution of $HAuCl_4$ (5%) is used to deposit a thin layer of gold on CZT surface.
When $HAuCl_4$ salt is in an aqueous solution, the following reaction takes place:

$$HAuCl_4 + H_2O \rightleftharpoons H[AuCl_3OH] + HCl$$

In particular, without any external current, two reactions (one anodic and the other cathodic) take place simultaneously at the surface of the CZT crystal. The complete reaction is:

$$2H[AuCl_3OH] + CdZnTe \rightleftharpoons 2Au + CdCl_2 + ZnCl_2 + TeCl_4 + 2H_2O$$

In this reaction Au atoms are deposited on CZT surface and $CdCl_2$, $ZnCl_2$ and $TeCl_4$ salts are dissolved in the solution[44].
The thickness of the gold layer roughly increses as the square root of the time of reaction and the typical deposited thickness is around 600 Å[45]. .
In this type of process a significant amount of gold diffuses into the bulk following the same square root law creating a thin highly doped region under the contacts. Due to the low doping efficiency of gold, however, perfect ohmic contacts cannot be achieved by using this method on CZT. Electroless contacts always exhibit a small rectifying behaviour.
At IMEM-CNR institute the standard deposition is obtained with 1 min of reaction at 20°C. Using this procedure a good reproducible contact can be deposited on CZT crystals. The typical IV characteristics of these contacts are shown in fig.3.5.

5.3.4 Passivation

In order to increase the surface resistivity, a passivation process must be done after the deposition of contacts. The standard passivation procedure is done using an aqueous solution of $NH_4F + H_2O_2$ (3%). For this process, the sample is immersed for 6 minutes in room temperature solution. After this process, the reduction of leakage currents can be ascribed the formation of an oxide layer with higher resistivity. The oxide layer formed by NH_4F-based etching was studied by optical ellipsometry with a variable angle spectroscopic ellipsometer working in the range 200-1700 nm. The measured refractive index for the layer is compatible with that of an oxide resulting from a mixture of ZnO, TeO_2 and CdO (n=2.2 and n=2.5 at 1500 nm, respectively). The passivation procedure can be performed on the sample before or after the contact deposition.

It has been tested that the oxidizing solution does not affect or remove the metal layers on the CZT surface.

5.4 Detector Current-voltage characteristic

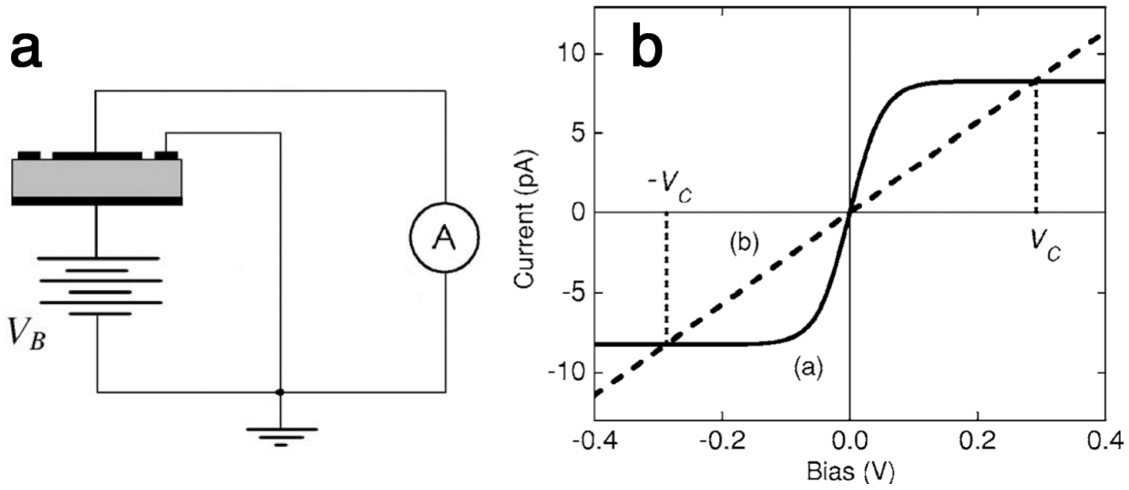

Figure 5.3: *a) The experimental setup for CZT current-voltage characteristic. b) Ideal thermionic IV characteristics without series resistance (a) and bulk I-V curve (b)[46].*

As discussed in chapter 3, the current-voltage (I-V) characteristic is a fundamental tool for the resistivity measurement, that is one of the crucial parameter for radiation detectors. Also the metal-semiconductor contact behaviour and the dark current value can be extracted from the detector I-V characteristic. The most common contacts on CZT are made with Au or Pt and in both cases a rectifying contact is generally obtained. At IMEM-CNR institute electroless deposition of gold is used for making blocking contacts. For these type of blocking contacts, when the equivalent electric circuit of the detector is considered, an additional resistance (due to the contact barrier) must be added in series to the resistance of the bulk. Normally, in order to measure the resistivity of the material eliminating the effect of contacts, four-probe measurement must be done.

Unfortunately in the case of CZT these measurements are always affect by the error due to the not-negligible surface currents. To overcome this problem a two-probe method was proposed by Michael Prokesch and Csaba Szeles in 2006[46] for resistivity measurement in CZT. In this configuration (shown in fig.5.3 (a)) the central anode is surrounded by a grounded guard-ring and the current is measured between central anode and cathode contacts. In this configuration the surface leakage current does not contribute to the bulk current measured through the central anode.

The current-voltage characteristic of a Schottky diode with series resistance is given (thermionic theory) by:

$$I = I_s \left\{ exp\left[\frac{q(V_B - IR_S)}{k_B T} \right] - 1 \right\} \tag{5.2}$$

I_S is the reverse bias saturation current, q is the charge, R_S is the series resistance of the semiconductor, k_B is the Boltzmann's constant, and T is the temperature. For small current values the 5.2 becomes:

$$I \to 0, \quad R_S = \frac{V_B}{I} - \frac{k_B T}{q I_S} \tag{5.3}$$

where $\frac{k_B T}{q I_S}$ is the value of the resistance due to Schottky barrier. If the series resistance due to the semiconductor is much higher than the resistance of the contact, the second term can be neglected and R_S can be obtained directly from the I-V slope at low voltages. As shown in fig.5.3 (b) it is clear that, at low voltages (V< V_C), the series resistance (due to the semiconductor) controls the slope of the I-V curve and linear I-V curve can be measured between -V_C and +V_C.

5.4.1 Experimental Setup

The experimental setup for current-voltage characteristic measurement is shown in fig.5.3 (a). The applied voltage and the current were simultaneously measured by the same instrument (source-meter). All the characteristic were measured using a closed metal box equipped with gold micro-probes connected to the instrument. The box is fundamental in order to limit the electrical noise and to ensure the absence of light during the measurement. All the voltage and current values were recorded by a software and the I-V curve was plotted in real time.

5.5 CdZnTe Detector Spectroscopy

The study of the spectroscopic performance for CZT material grown at IMEM-CNR institute is another crucial part of the work for device realization. Both material quality and its processing for the preparation of the devices can have a critical influence on the spectroscopic response of detectors and hence the spectroscopy measurements are therefore important for the development and optimization of both these aspects.
In this work all the spectroscopic measurements were performed at INAF-IASF in Bologna under the supervision of Dr. E. Caroli and Dr. N. Auricchio. Samples with a simple planar configuration were studied; in particular two symmetrical electrodes where deposited by electroless technique on the two opposite surfaces, covering the whole area in order to minimize the field distortion.

5.5.1 Spectroscopy Set Up

The setup used in this characterization is shown in fig.5.4. The basic readout chain can be summarized as follow:

- In order to amplify the detector signal, a charge sensing preamplifier (CSP) is directly coupled to the detector anode. This component (also called "per-amplifier") is a commercial eV-509.
- The signal coming out of the preamplifier is further amplified by a shaping amplifier (Ortec model 450).

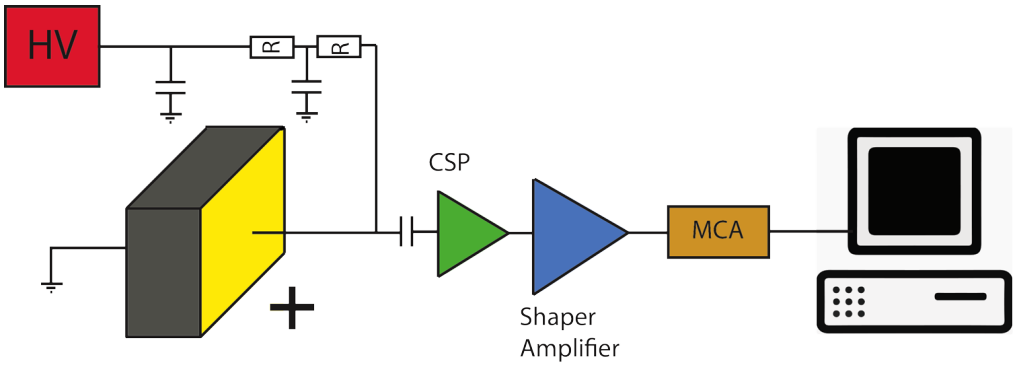

Figure 5.4: *Basic electronic readout chain for CZT detector.*

- The output of the shaping amplifier is converted into digital signal by a Multi Channel Analyzer (MCA).
- Highly-stabilized HV DC generator is connected to the detector, in thsi setup the voltage can be varied between 0 and 1000 V.
- A conventional PC is used in order to record the MCA signal plotting also the detector response on the screen.

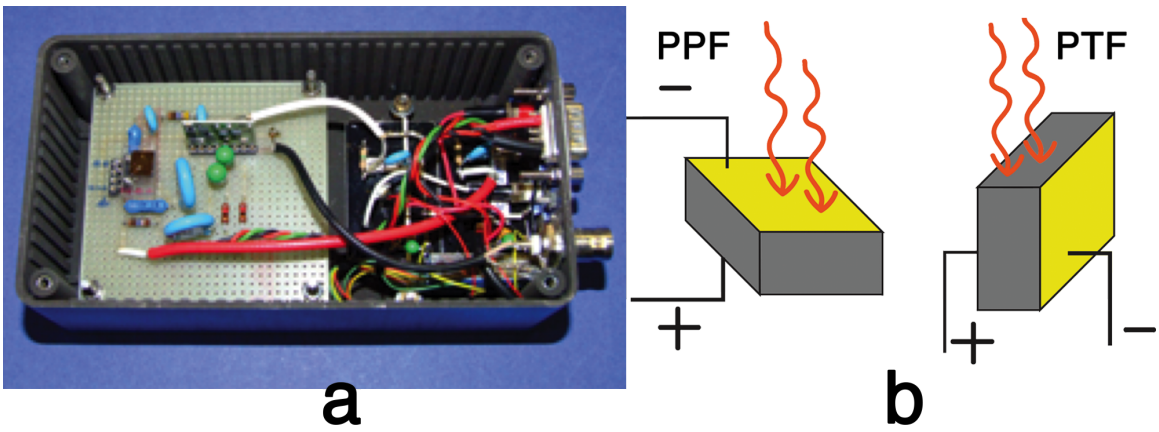

Figure 5.5: *a) The readout electronic chain used at INAF-IASF institute. b) PPF and PTF irradiation configurations.*

During the measurements, the detectors were placed inside an aluminium box in order to reduce the electronic noise and to shield them from light (fig.5.5 (a)). The box is equipped with a particular support that allows the mounting of the sample in two irradiation configurations: the planar parallel field (PPF) and the planar transverse field (PTF) (shown in fig.5.5 (b)). The two configurations differ in the way radiation interacts with the detector material. For the PPF configuration the beam impinges the top surface and interacts with the material generating an exponential decay and it's fully stopped at a certain distance from the entering electrode depending on the photon energy. In the PTF configuration instead, the events are generated at every depth in the sample thickness. In this case the exponential decay occurs in the direction

parallel to the surface area. Depending on the energy of the incident photons and on the type of application one configuration may be preferred over the other. In general, to achieve the best detector resolution, a collimated source must be used in PTF configuration to irradiate the part of the detector which is closer to the cathode electrode. The spectra acquisition was performed without the collimated sources and without any electronic correction of the signal. The source was positioned at a distance between 3 and 5 cm to the top of the measurement box. In this configuration the entire surface of the sample was illuminated during the measurement. The parameter of the measurements were:

1. The shaping time of the amplifier. A correct integration time must be selected in order to collect all the signal without increasing the noise.
2. The Bias was selected in order to collect all the carriers (highest CCE) without increase also the noise associated with the dark current.
3. The gain of the Amplifier.
4. The time of measurement must be high enough to collect a statistical number of events.

5.6 Transport properties

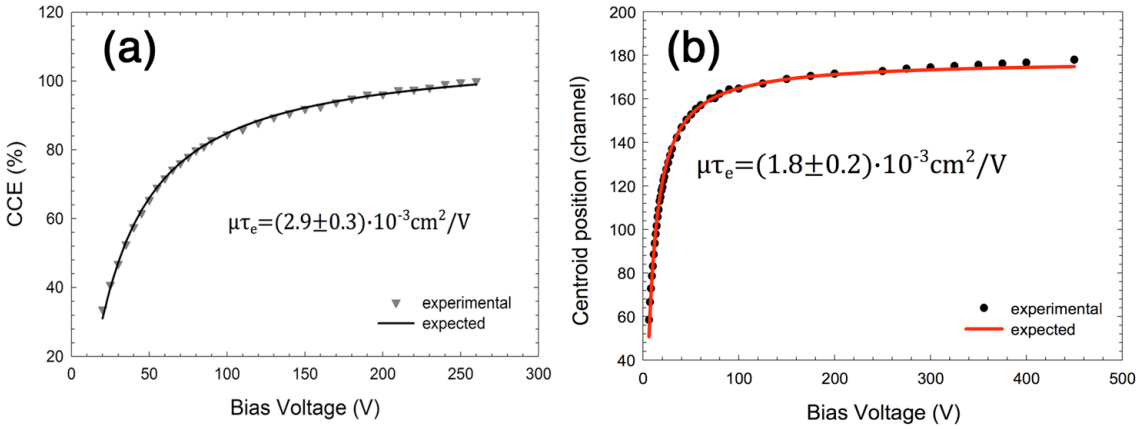

Figure 5.6: *μτ product of two samples obtained by fitting the centroid position of the a) 22 KeV emission of ^{109}Cd source and b) 5 MeV α-particles emitted by ^{241}Am source, with the electronic part of the Hecht equation.*

The μτ product represent a good indicator of the transport properties of the device. The μτ product is usually calculated from the fitting of the curve obtained by measuring the CCE (corresponding shift in the peak position) as function of applied voltage. The measurement can be performed with different radiation sources: alpha particle, an X-ray source with a low energy emission, a laser or by means of photocurrent measurement. The peak position is identified by a gaussian plot of the photopeak in the detector response. In this work both the alpha particle and the X-ray source techniques were used. The resulting curve is fitted with the Hecht equation, considering only the electron part of the equation, since electrons are the only carriers drifting

trough the device and contributing to the photopeak formation in the used configuration. In fact the irradiated electrode is the cathode, and with both sources the events are occurring very near to the entering surface. The measurement require the same electronic equipment as the measurement of the spectroscopic response with a standard X-ray source (described in the spectroscopy setup section).
The peak position is identified by a gaussian fit of the photopeak. Because of the importance of the measurement of the $\mu\tau$ value in judging the material and device properties the measurement was performed independently, in different laboratories, on the same set of samples. The measurement with the alpha particle source was performed in Physics Department of Parma, the measurements with the X-ray source at INAF-IASF using the 22 KeV emission of the ^{109}Cd source. In figure 5.6 (a) and (b) some of the resulting fitting are shown. The obtained values for electrons is between 1 and 3 $\cdot 10^{-3}\, cm^2/V$ for both kind of sources.

5.7 Detector Characterizations

More than 50 CZT detector samples were tested during this work. The aim of this characterization was the study of the quality of the material grown at IMEM-CNR institute. During the PhD work several ingots were grown and characterized. Some of the measurements that will be shown in the following pages were made in collaboration with PhD Laura Marchini; my work follows her work on CZT detector characterizations.

5.7.1 Current-Voltage characteristic

The first characterization for detectors is the I-V characteristic. This because, as discussed in the previous chapter, the resistivity of the material, the quality of the contacts and surfaces can be obtained at once from a simple I-V measurement. Some examples of typical IV characteristics for planar detector with gold electroless contacts are shown in fig.5.7 (a) and fig. 5.8. As shown in these figures, gold electroless contacts on CZT grown at IMEM-CNR institute have a double diode back-to-back behaviour.
In fig.5.7 the low-voltage linear IV characteristics and the linear fits are shown. In table 5.1 the resistivity of several samples is shown. For different ingots is possible to note a small difference in the value of the resistivity which is, however, always in the order of $10^{10}\,\Omega cm$ (i.e. the typical value reported also in literature for CZT material).
The I-V characteristic is also important for the spectroscopic performance of the detector, because small dark current produces less noise inside the system and a better energy resolution can be achieved.

5.7.2 Photo-Induced Current Transient Spectroscopy

Photo-Induced Current Transient Spectroscopy (PICTS) was performed on the boron-encapsulated CZT grown at IMEM- CNR institute in order to investigate the electronic levels in the forbidden gap. These measurements were carried out at University of Bologna by prof.ssa Anna Cavallini. PICTS technique can identify deep levels, against strong background signals, and it is a strong

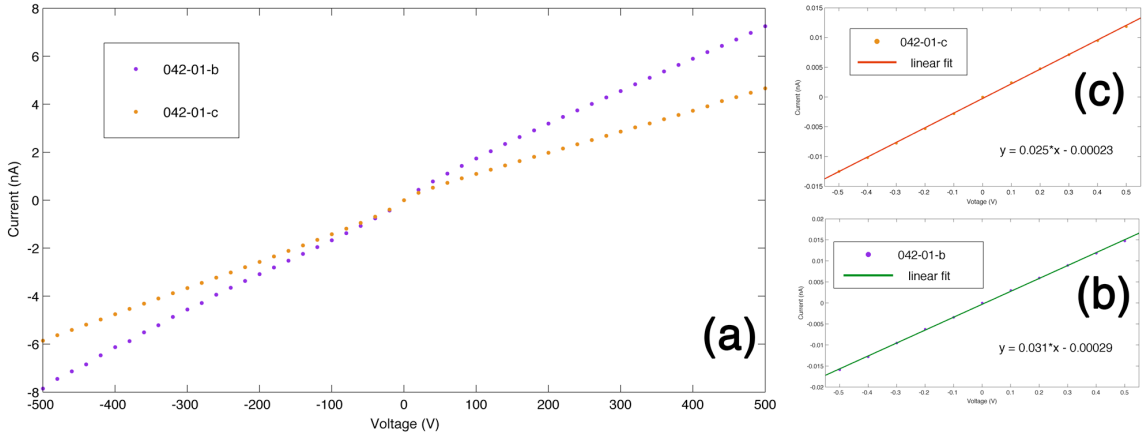

Figure 5.7: *a)I-V characteristic of CZT samples of the ingot 042. b) and c)Low voltage linear I-V characteristic and the linear fit.*

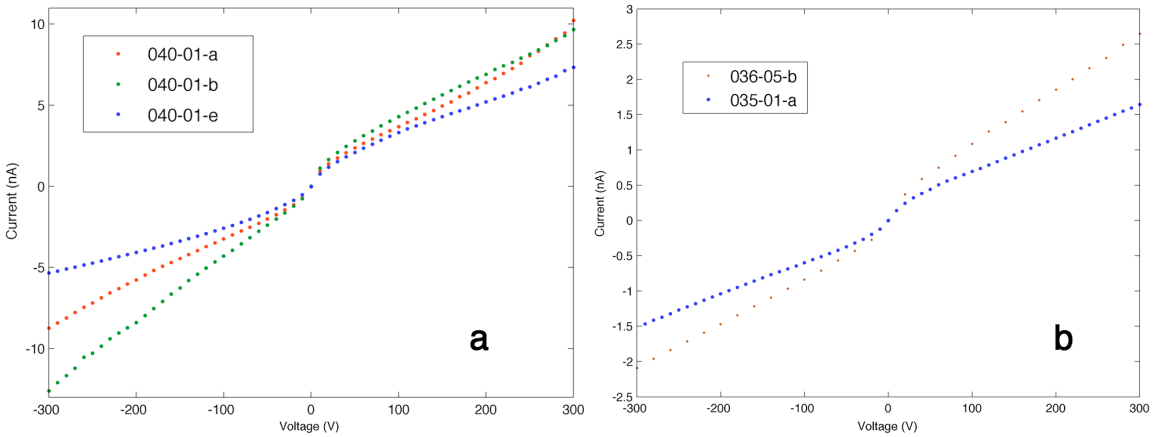

Figure 5.8: *a) I-V characteristic of several samples of ingot 040 with gold electroless contacts. b)I-V characteristic of two samples with gold electroless contacts.*

technique for characterizing the CZT material. In particular a comparison between "standard CZT" grown with standard Vertical Bridgman (VB) and CZT growth with Encapsulated Vertical Bridgman (EVB) was carried out. The PICTS spectra of these different materials are shown in figure 5.9 (a).

From comparison of PICTS spectra it is possible to note that the response of the two materials is quite different. Each peak (Z1 to Z6) in the spectra reported in fig.5.9 (a) corresponds to a type of level inside the band gap. From these spectra the type and the concentration of these levels can be extrapolated.

The most evident result is that in EVB detectors less type of levels can be found and the density of traps emitting in the range [110–320] K is lower, as shown in the histogram of fig. 5.9 (b).

This measurement confirm that with the Boron Encapsulated Vertical Bridgman technique material with low types of level in lower concentration (in comparison to the standard Vertical Bridgman method) can be grown. These concentrations of traps are also in agreement with the values that can be found in literature[48]. This measurement confirms that with the Boron

Sample	Thickness (mm)	Resistivity (Ωcm)	Sample	Thickness (mm)	Resistivity (Ωcm)
035-01-a	2.66	$2.5{\cdot}10^{10}\ \Omega cm$	040-01-d	2.6	$2.2{\cdot}10^{10}\ \Omega cm$
035-01-b	2.68	$2.5{\cdot}10^{10}\ \Omega cm$	040-01-e	2.6	$2.46{\cdot}10^{10}\ \Omega cm$
035-02-e	2.62	$6.5{\cdot}10^{10}\ \Omega cm$	040-01-a	2.6	$2.48{\cdot}10^{10}\ \Omega cm$
035-02-d	2.64	$2.06{\cdot}10^{10}\ \Omega cm$	040-01-b	2.6	$1.91{\cdot}10^{10}\ \Omega cm$
036-04-a	1.04	$4.2{\cdot}10^{10}\ \Omega cm$	040-01-c	2.6	$2.01{\cdot}10^{10}\ \Omega cm$
036-04-b	1.01	$1.72{\cdot}10^{10}\ \Omega cm$	042-02-b	2.5	$2.83{\cdot}10^{10}\ \Omega cm$
036-05-b	2.14	$3.19{\cdot}10^{10}\ \Omega cm$	042-01-b	5	$2{\cdot}10^{10}\ \Omega cm$
036-01b-a	2.15	$3.92{\cdot}10^{10}\ \Omega cm$	042-01-c	5	$2.32{\cdot}10^{10}\ \Omega cm$

Table 5.1: *Resistivity of some CZT samples measured during this work.*

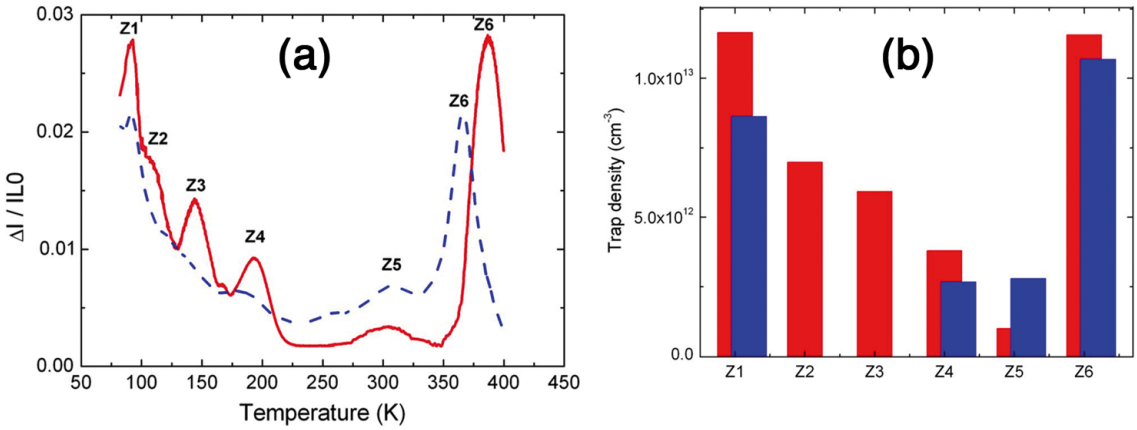

Figure 5.9: *a)Typical PICTS spectra of VB (red line) and EVB (dotted blue line) detectors. b)Histogram of the density of the traps in VB (red) and EVB (blu) detectors[47].*

Encapsulated Vertical Bridgman technique provides a material with a lower number and lower concentration of levels than Vertical Bridgman method. The revealed concentrations of traps are in agreement with the values that can be found in literature. Furthermore, these results also indicate that most of the boron atoms that contaminate the CZT grown with EVB method, are however electrically inactive and do not affect the transport properties of the material.

5.7.3 CZT Spectroscopy

The detector performance is usually qualified by the photopeak resolution and the peak to valley ratio of the photopeak. These quantities depend on several experimental parameters that can be set during the measurement (as discussed in the spectroscopy setup section).
In CZT detectors the resistivity is higher with respect to CdTe and hence the standard bias applied to the device is higher with respect to the one used for CdTe detectors. 100 V/mm are commonly accepted as the minimum bias to have a sufficient electric field to drift charge carriers (when the CCE is close to 100%). During the testing of IMEM devices several parameters were studied in order to obtain the best resolution in the acquired spectrum. The optimal shaping time of the amplifier and voltage were deeply analysed for several of the studied samples. In general the behaviour of IMEM samples was found to be very reproducible. A strong

homogeneity of characteristics was found among the different ingots and in particular among the samples cut from the same ingot. The acquisition method was set up in order to have the best reproducibility in the measurement. The spectra were all acquired without the collimation of the sources and by keeping constant the distance between the source and the measuring box. The spectra were acquired one hour after the biasing, so that sample internal electronic configuration was stable after a relatively long stay in the dark and under polarization condition. The first test discriminates the samples with better qualities: if the ^{241}Am photopeak (59 KeV) was resolved at 100 V per mm, further investigations were done to find the optimal configuration. The samples were biased at different voltages and with different sources; then the optimal bias is chosen by looking at the FWHM of the characteristics photopeak of every radiation source.

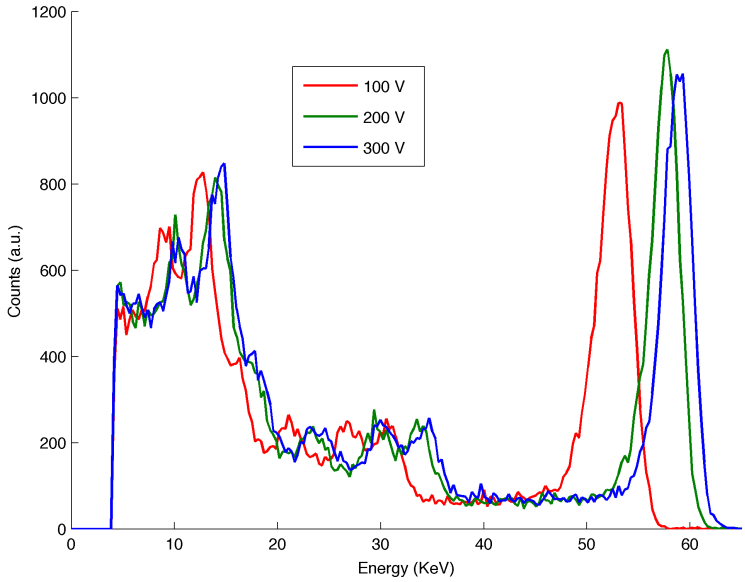

Figure 5.10: *Response of sample 040-01-a with the 241Am source at different biases.*

In fig.5.10 it is possible to see that the photopeak position changes with the applied bias due to the increase in the charge collection. On the contrary, the increase of bias can lead also to an increase of dark current and a compromise must be find in order to achieve the best energy resolution and the highest CCE (peak position close to the theoretical position in energy). In fig.5.11 the response spectra of two samples with ^{241}Am source are shown. These spectra were taken in the best condition and the FWHM and the resolution can be calculated from them. In particular an energy resolution of 6% for the 040-01-f and 6.2% for 040-01-a can be extracted. Moreover, for both spectra also a large number of peaks are solved in the lower energy range. In fig.5.12 several emission peak of the ^{241}Am are solved and labelled. Also the two escape peaks of Cd and Te are clear visible.

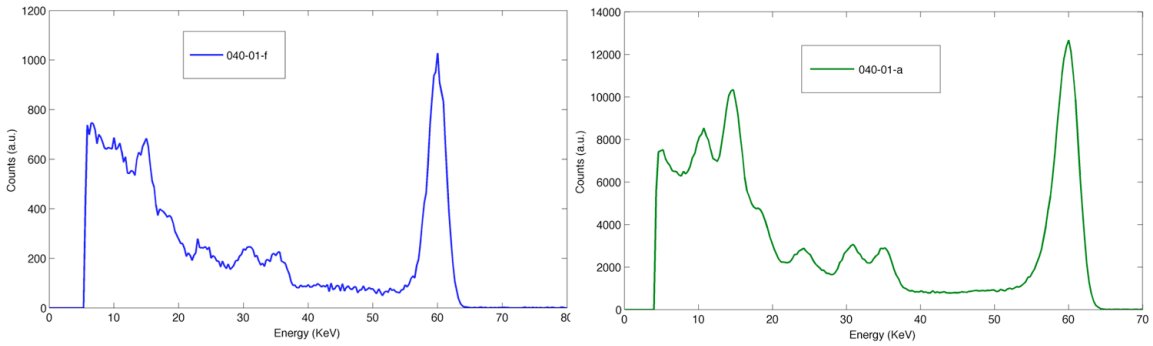

Figure 5.11: *The spectral response of two samples with the* ^{241}Am *source in PTF configuration.*

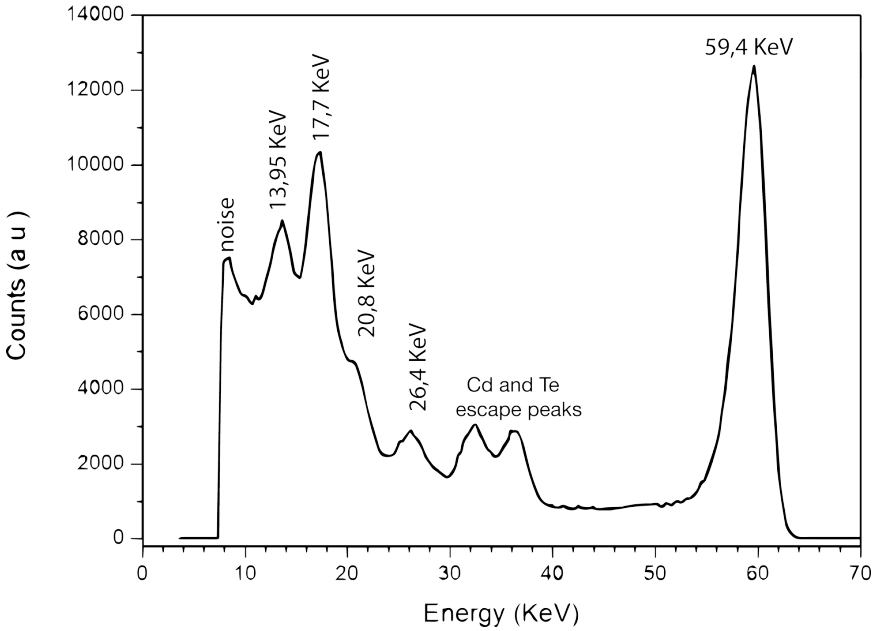

Figure 5.12: *Response of the 040-01-a sample with labelled peaks.*

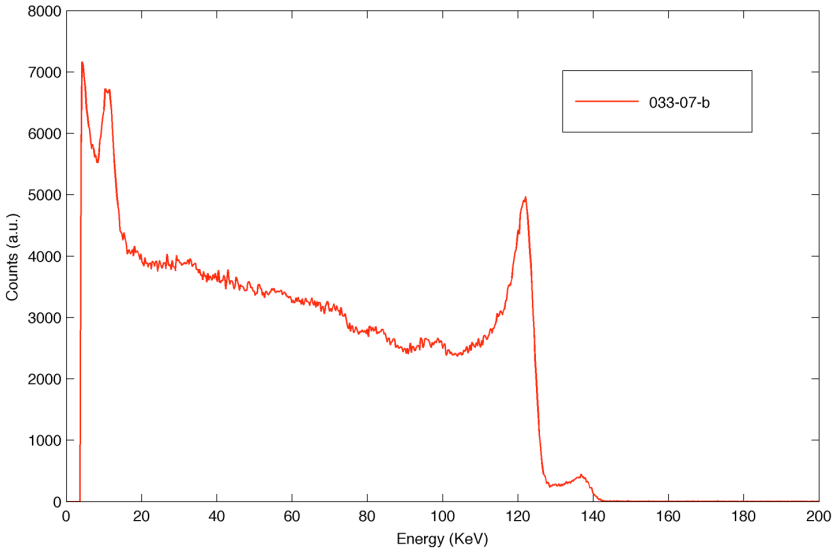

Figure 5.13: *Response of the sample 033-07-b with the* ^{57}Co *source.*

For simple planar detector, upon increasing of the gamma photon energy, the effect of hole trapping starts to be dominant and detector resolution decreases. In figure 5.13 the response of the sample 033-07-b detector in PTF configuration with ^{57}Co is shown. In this spectrum only three main peaks are solved by the detector and the energy resolution of 9% at 122 KeV can be calculated.

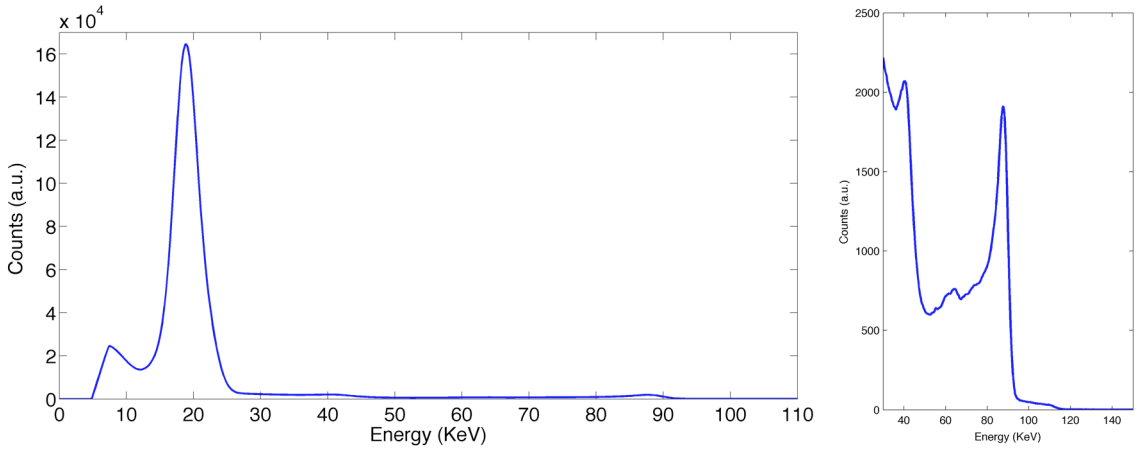

Figure 5.14: *Response of the 033-07-b detector with* ^{109}Cd *source.*

In fig.5.14 the response of the detector 033-07-b with ^{109}Cd is shown, in particular on the right figure the 88 KeV photopeak is shown with 8.4% energy resolution.
In ^{57}Co and ^{109}Cd spectra the effect of trapping is clearly visible in the lower energy part of the photopeak. Increasing the energy of the incident photons the effect of trapping starts to be dominant and at 660 KeV, for example, the photopeak cannot be solved by the detector. For the material characterization point of view this means that in the CZT material grown at IMEM-CNR institute the transport properties of holes are very low and the quantity $\mu_h \tau_h E$ is always smaller than detector thickness. Hole transport properties, indeed, cannot be measured by standard technique in CZT grown at IMEM-CNR institute because of the strong trapping. On the contrary, electrons transport properties are good and in agreement with the values reported in literature. Single charge devices (such small pixel, stripes and coplanar grid) must be fabricated in order to increase the energy resolution of of IMEM-CNR CZT detectors.

5.8 Progress in the Development of CdZnTe at IMEM-CNR

Several ingots grown at IMEM-CNR by Boron Encaplsulated Vertical Brigman technique were tested and the material quality was evaluated.The ingots typically show large single crystal parts and several 1 mm x 1 mm x 5mm detectors can be prepared. Using B_2O_3 as encapsulant there is no interaction between the ampoule and the ingot during all the growth and very smooth side surfaces are obtained. As demonstrated by PICTS measurements, this can also reduce the contamination of the material due to the interaction with ampoule and the sealing procedure. A possible drawback of B_2O_3 is the contamination of B atoms inside the CZT, but the PICTS measurements showed that B atoms are not electrically active and do not affect the transport

properties of the material.
The transport properties of electrons in CZT grown with EVB technique are good and in agreement with the values reported in literature. In particular value of $\mu_e\tau_e = (1 \div 3) \cdot 10^{-3}\ cm^2/V$ is normally measured. On the contrary the $\mu_h\tau_h$ for holes is very low and no signal contribution can be recorded in a typical measurement.
As shown in fig.5.11 the spectroscopic response of detectors is very good with ^{241}Am source and a resolution of 6% is normally measured for CZT grown at IMEM-CNR. At higher energy the effect of trapping in the planar detector starts to be dominant and the response of detectors is strongly limited. To overcome this problem, single polarity charge sensing devices must be used if high-energy resolution has to be achieved.

5.9 3D CdZnTe Detectors

CZT represents a almost a standard material for radiation detector and high-performance large volume detectors can be fabricated. In particular, during this work, the undersigned was involved in a very interesting project, funded by European Space Agency (ESA). The project, entitled "3D CZT High Resolution Detectors", was leaded by Doc. Carl Budtz-Jorgensen and Doc. Irfan Kuvvetli, from National Space Institute of Technical University of Denmark (DTU Space Center). This project started from original idea of Doc. Carl Budtz- Jorgensen and Doc. Irfan Kuvvetli that developed a novel type of CZT based detector: the drift stripes 3D detector.
IMEM-CNR institute was involved in some important parts of the project:

- Detectors preparation. All detectors and prototypes were completely made at IMEM by Nicola Zambelli and Giacomo Benassi.
- Detectors characterization. The detector characterization was performed at European Synchrotron Radiation Facility (ESRF) in Grenoble.
- Data analysis. The data analysis of the Synchrotron characterization.

In particular, Nicola Zambelli and Giacomo Benassi were directly involved in the characterization at ESRF and the data analysis of the 3D detector.

5.9.1 3D drift stripes detector concept

Requirements of X and gamma ray detectors for high energy astrophysics missions include high detection effiency and good energy resolution as well as fine position sensitivity even in 3D. X-ray astrophysics missions in the keV to MeV band require advanced instrumentations in both spectral and imaging capabilities. The instrumentation for these types if telescopes require detectors of high efficiency, with energy resolution on the order of few keV and capability of 3D position sensitivity.
Compound room temperature semiconductor detectors such as CZT are good candidates for hard X-ray (higher than 10 keV) and Gamma-ray astronomy instrumentation. The most significant

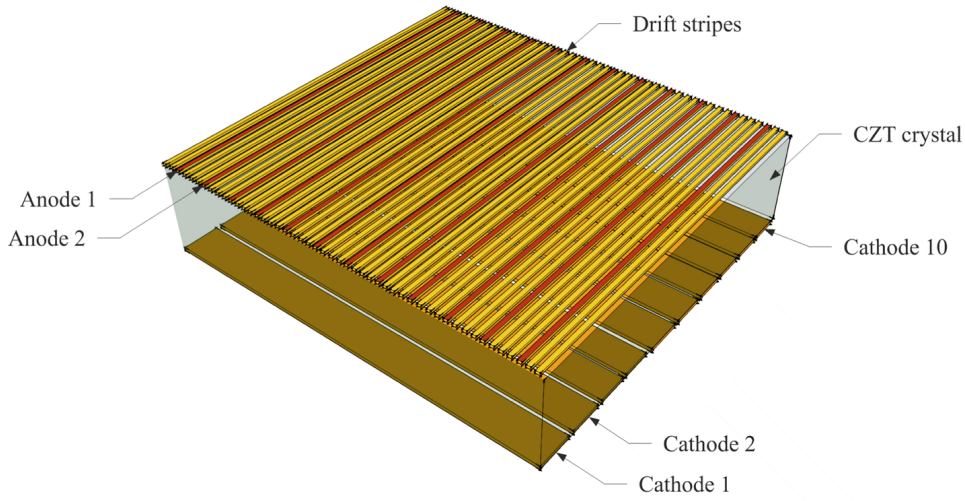

Figure 5.15: Principle of the CZT drift strip detector. The drift strip electrodes and the segmented cathode are biased in such a way that photo-generated electrons moves to the anode strips.

disadvantage for these type of detectors is the incomplete charge collection, especially for holes which can affect and can degrade the detectors spectral performances. As discussed in chapter 3 this problem can be solved using a single charge weighting potential generated by, for example, small stripes electrodes. The Reducing the dimensions of the electrodes significant improvement in energy resolution can be achieved. The only problem is the lost of carriers connected to the reducing in the electrode dimensions. To overcome this problem DTU Space Center proposed [49] [50]a novel type of detector that uses several non-collecting stripes (drift stripes) surrounding the collecting anode. These stripes are biased with a negative bias (compared with the anode bias) in order to focus the carriers on the collecting electrode. Fig.5.15 shows the principle of CZT drift strip detectors, the detector structure is similar to the Silicon drift detector which was first time introduced by Emilio Gatti and Pavel Rehak in 1983[51]. The structures employs a number of drift strips (three) separating each anodes readout strips on the upper side and a segmented (ten) cathode on the lower side. A voltage divider supplies each drift while the anodes strips are held at ground potential. The detector is biased such that the electrons, produced by the interaction of the incoming photons with CZT crystal, are drifted to an anode readout strip. As we cited above, the positive charges (holes) produced by the photon interaction have a poor mobility-lifetime product ($\mu\tau$ up to $10^{-5}\, cm^2/V$) and will, with high probability, be trapped in the detector. However, the anode signal is unaffected by the holes since the anode strips are screened by the bias strips[52]. The anode signals are therefore proportional to the photon energy and high spectroscopic performance is ensured for CZT materials with good electron drift properties. Although the spectroscopic properties of these detectors type are almost independent of material holes transport properties, they are obviously very dependent in the electron transport properties; for this reason crystals with fluctuating electron trapping length will result in degraded detector performances.

5.9.2 Detector prepared during the project

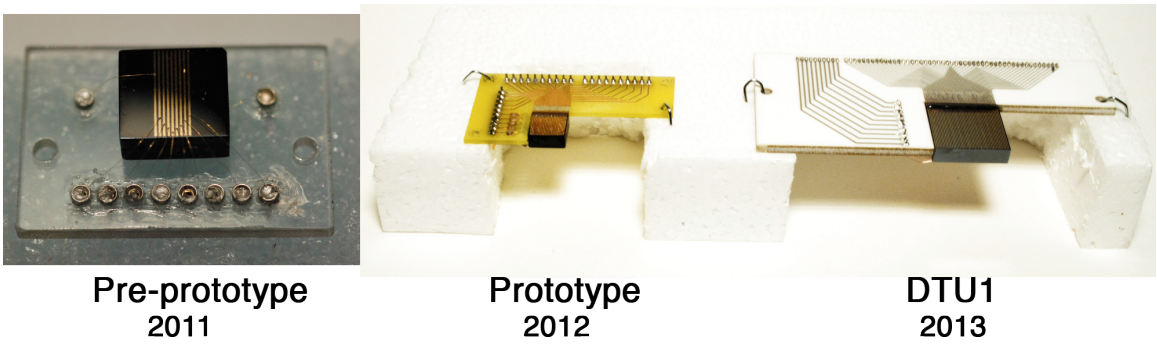

Figure 5.16: *Pictures of some detectors made during the 3D CZT detectors project.*

For the 3D CZT detector project several detectors were made:

1. The first 3D detector called "pre-prototype" was made in 2011 (fig.5.16 left) with dimensions of 10mmX10mmX5mm. It had only one drift cell (1 anode and 8 drift stripes) and a full area cathode electrode. Therefore this detector was not a real 3D but 2D images were measured.

2. The second 3D detector called "prototype" was made in 2012 (fig.5.16 centre) with dimensions of 10mmX10mmX5mm . It had 4 anode stripes and 13 drift stripes on one surface and 5 cathode stripes on the other side. This was a real 3D detector but, due to some problems related to the crystal quality, it was impossible to characterize the properties of the final device.

3. In 2013 (shown in fig.5.16 right), four 3D detectors were made, labeled according to the order of preparation as DTU1, DTU2, DTU3 and DTU4. These detectors have 12 anodes, 37 drift stripes and 10 cathode stripes. The dimension of the crystals were 20mm x 20mm x 5mm. DTU1 was the only one detector without alumina layer among the anodes, the drift stripes were deposited directly on passivated CZT surface. DTU2, DTU3 and DTU4 were realized depositing an alumina layer on the passivated CZT surface among the anode stripes, with the aim to reduce the leakage current between adjacent drift stripes. The DTU2 in particular was the detector that was characterized with the synchrotron beam at ESRF.

5.9.3 3D detector preparation

The detector preparation still remains a critical step for obtaining high performance CZT detectors. Each step of preparation requires special atten- tion and, for this project in particular, a lot of technological problems had to be solved. All the processes, that will be discussed in this chapter, were performed by Giacomo Benassi and Nicola Zambelli using the IMEM-CNR facilities.
IMEM has a long experience in CZT detector preparation, in particular in the last 5 years several

detectors were fabricated. The aim of these detectors was the characterization of the material grown at IMEM has a long experience in CZT detector preparation, in particular in the last 5 years several detectors were fabricated. The aim of these detectors was the characterization of the material grown at IMEM institute and therefore stan- dard detectors (planar detectors) were normally fabricated on relatively small CZT samples. For this reason the complexity of these 3D detectors required a different approach and an incredible effort was made in order to increase the quality and to solve problems of standard fabrication procedure. The detectors were realized on crystals produced by Redlen. This choice was imposed by the committers (DTU), who selected the best commercial material on the market in a previous step of the project.
The main challenge of the project can be described listing some features of these detectors:

- The size of the 3D detector. Before this project the standard dimensions for detectors made in IMEM were 7mmX7mm for 2 or 3 mm thick. For 3D CZT project the crystal size increased to 20mmX20mm for 5 mm thick (commercial Redlen crystals) and, as will be discussed later, due to this reason, many processes had to be changed.

- The complexity of the electrodes geometry. 49 stripes with 0.4 mm pitch (150 µm stripes width and 250 µm of space) constituted the anode electrode and 10 stripes constituted the cathode electrode. Therefore a double (at least) photolithography process on both surfaces was done representing one of the main challenge. Moreover such high number of independent electrodes required an extremely high uniformity of photolithography and contact deposition processes that was not trivial to reach.

- The extremely low currents requirement.For 3D project there was the requirement to have the currents between adjacent stripes lower than 2 nA @ -100V at T=22oC. This because for this type of detector is very important to decrease the noise due to the currents between stripes. As discussed before the control of surface resistivity is still an open challenge in the detector preparation technology. For this reason an alternative passivation process was developed during this project in order to decrease the currents between stripes. This process was used for the first time during this project and a lot of time was spent in order to develop all the procedures.

- The bonding of detectors. This process, as will be discussed later, was one of the main challenges in the project and in some cases was the critical step of the 3D detector realization. It was not trivial to make 50 electrical connections between detector and PCB, moreover these connections had to be mechanical stable (the detector were sent to Denmark) with a good electrical contacts (without any noise). For bonding a semi-automatic machine was developed with this machine the bonding resulted more reproducible and faster than the manual process (used before this project).

- The alignment. These detectors had to be perfectly aligned to the PCB and, for making bonding, to the pads of PCB. The alignment with the PCB was fundamental for the characterization with Synchrotron beam. This because, due to the small dimensions of the beam (50 µm x 50 µm) any small change in the alignment angle of the detector with PCB could be a strong change in the real dimension of the beam detector interaction volume.

For all these reasons this project was a personal and a group challenge. All these problems represented a very interesting challenge that involves a lot of personal energies and time. Several persons of the IMEM-CNR institute were involved in some parts of the detector realization. It was impossible to solve all the problems for such as complex detector but finally very good results were observed during the characterization at synchrotron facility.
We are very proud with the results of this project and for all the developments that we made in all the detector preparation processes.

5.9.4 Detector preparation steps

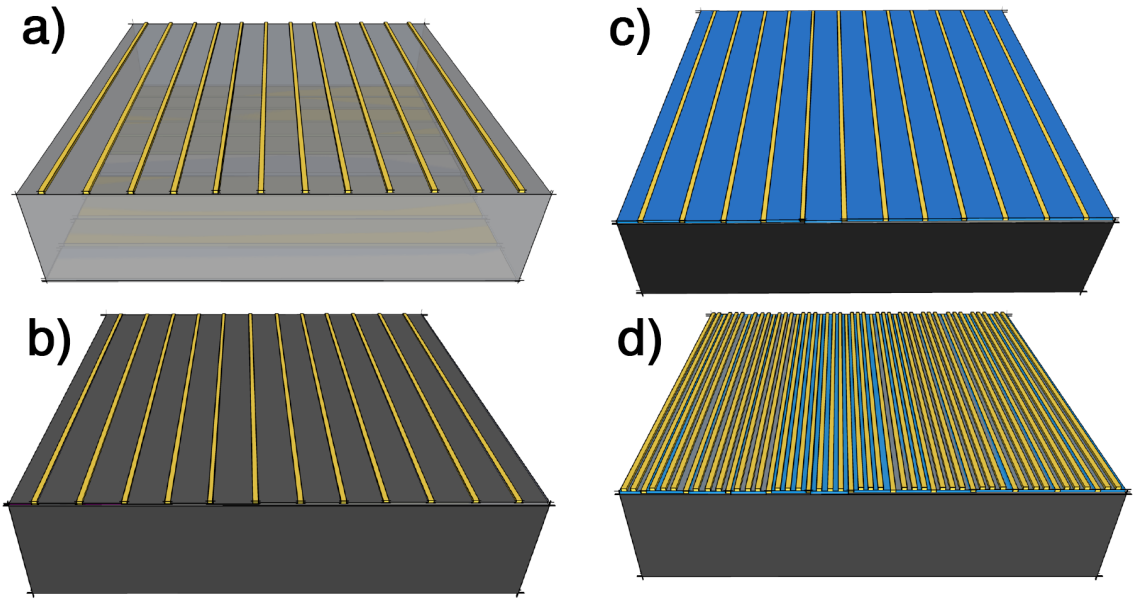

Figure 5.17: *Sketch of the detector preparation steps. a)depostion of anode and cathode stripes, b)passivation of surfaces, c)alumina depostion (only for detectors DTU2,3 and 4), d)deposition of the drift stripes.*

All the 3D detector fabrication steps are shown in fig.5.17 and they can be summarized as follow:

1. Mechanical process. In this process all the six surfaces of the crystal are polished and lapped, at the end of the process a sample with six mirror surfaces is made.

2. Deposition of collecting electrodes. In this step, using a double photolithography process, the 12 collecting anodes and the 10 cathodes are deposited. All these contacts are made of gold deposited via electroless technique (fig.5.17a).

3. Passivation. In order to increase the surface resistivity a standard passivation process was made on all the surfaces of the crystals (fig.5.17b)..

4. Alumina deposition. First of all the deposited gold anode contacts (step 2) were protected using the photoresist deposited by photolithography pro- cess. Then a 150 nm Al_2O_3 layer

was deposited with Pulsed Electron Deposition (PED) technique (fig.5.17c). This step was done only for detectors DTU2, DTU3 and DTU4.

5. Deposition of drift stripes. On passivated CZT surface and/or on alumina layer, gold drift stripes (non collecting electrodes) were evaporated. Also for this deposition a photolithography process was necessary (fig.5.17d).
   In the following, all the single processes will be discussed, in particular: mechanical polishing, photolithography, contact deposition, passivation, alumina deposition, and bonding. In figure 5.18 some pictures of the detector during the processes are shown.

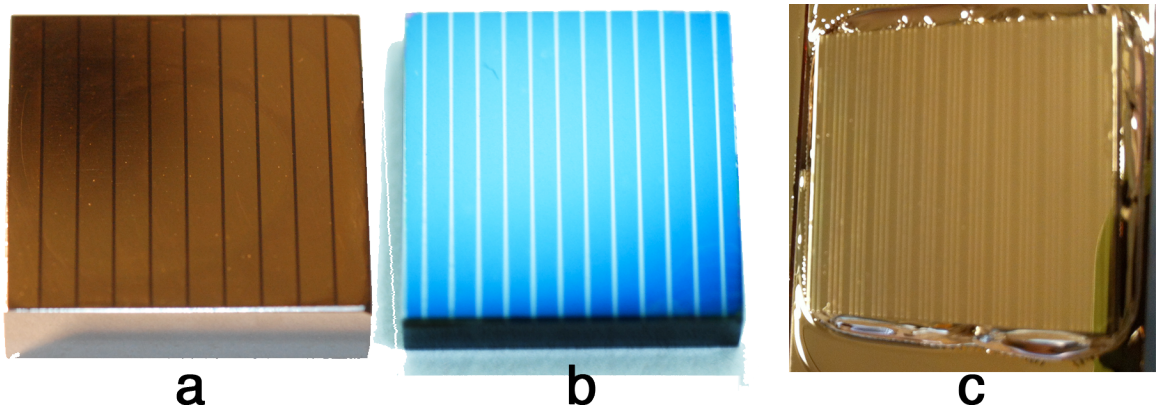

Figure 5.18: *Some picture of the detector during the preparation: a) cathode stripes, b) alumina deposited by PED and c) the evaporated drift stripes.*

5.9.5 Mechanical polishing

The Redlen crystals (dimension 20mmX20mmx5mm) are sold with pixelated gold anodes and planar gold cathodes this represents the standard detector geometry of this company. The first step was therefore to remove all the gold contacts from crystals. More details of the polishing porcess are described in section 5.3.2.
Due to the big dimensions of these crystals special attention was taken in order to increase as much as possible the uniformity of the surfaces. This because is well known that due to mechanical polishing the peripheral area of the crystals can be reduced more than the central parts. This problem, that can be neglected in the small samples or using a chemo-mechanical process, required special tricks during the polishing (such as the double rotation of the sample).

5.9.6 Photolithography

Photolithography is the process normally used for making micrometer patterned contacts on a semiconductor surface. In this technique a UV light is used to transfer a pattern from a mask (made on quartz) to a light sensitive chemical photoresist, or simply resist, previously deposited on the substrate. After the exposition of the resist to UV light a series of chemical treatments are used in order to remove the exposed resist (if the resist is negative) or the contrary if the

resist is positive. After this process some parts of the sample are covered by a hard and chemical stable resist, other parts are free to be processed. The main steps of this technique are:

1. Using a Sulzer Electro Technic spin coater a uniformly layer of resist, that is a high viscosity liquid, is deposited on the surface of the sample. The thickness of the resist layer spun at 4000 rpm for 30 sec is around 1 µm.
2. The sample with resist is than baked in a special furnace at 90°C for 30 min.
3. Using a Karl Suss mask-aligner the patter of the mask is transferred to the resist (Microposit S 1813 G2). The resist used at IMEM is negative, the irradiated parts are removed by developer.
4. After exposition the resist is removed by dipping the sample in a basic solution called "remover" at 20°C for 1 min.
5. At the end of the process the sample is cleaned with high purity water and than dried with argon gas.

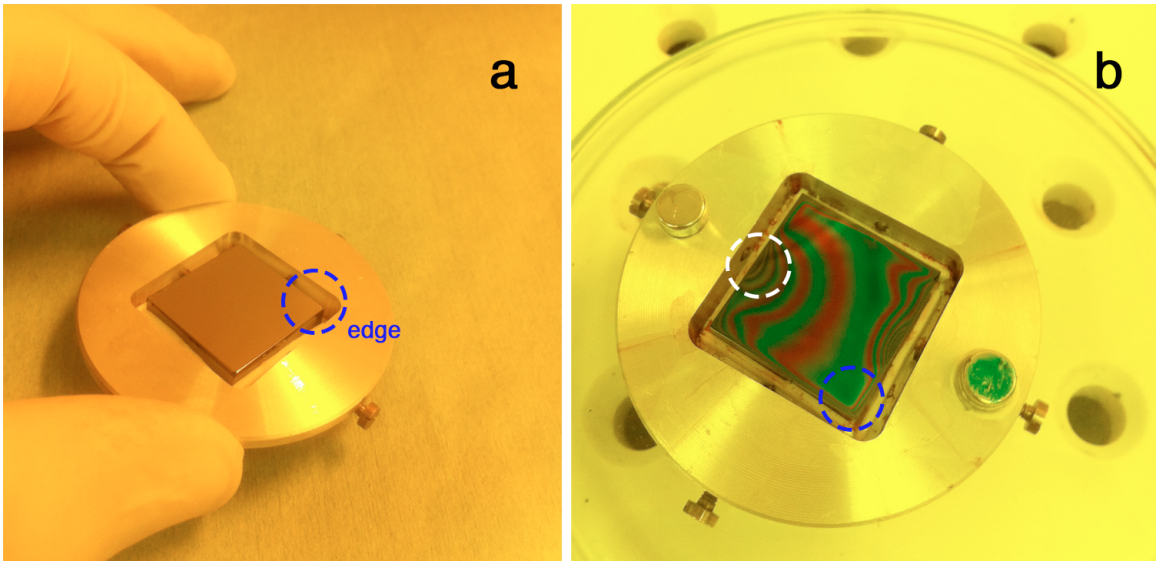

Figure 5.19: *a)The chuck for non-rounded sample designed and relized for this project. b)Using both chuck and plate a very uniform resist layer can be achieved.*

All these process steps were made inside the clean room of the IMEM-CNR institute. Also for the photolithography process several developments were made for 3D detector fabrication. In particular the main problem was connected with the deposition of the resist on the sample. This because the sample area was large (compared with standard samples) with a non-rounded shape, for these reasons a thickening of the resist in the edges was found. During the rotation (that is needed to uniform the liquid resist on the sample surface) the solvent contained in the resist evaporates and the viscosity of the resist increases during rotation time. It is important that evaporation process happens relatively slowly in order to allow the liquid resist to cover

the entire surface. If a non-rounded sample is rotated with the resist two main problems must be solved. The 4 edges of the square surface, during rotation, feel a tangential velocity higher than the central part of the sample. This means that the solvent contained inside the resist will evaporate faster in these edges. The result is that at the edges resist is too thick to be developed. To solve this problem a special chuck was designed and realized. This chuck has a rounded shape with a square hole for the sample (fig.5.19a): in this way the geometry of the system is again circular. With this chuck an extremely uniform resist thickness was achieved also at the edges, therefore the entire surface of the samples (20mm x 20mm) could be used (as requested by the specifications of the project). The second problem was connected with the surface area of the sample: the speed on the resist on the surface not enough to eliminate the excess of the resist before the evaporation of the solvent. By putting a metal plate very close (1 mm) to the rotating surface this problem was solved. With a plate a local sovra-saturation of solvent was created close to the rotating surface and the effect was to decrease the evaporation velocity of the resist on the surface. With this plate and the chuck the resist had uniform thickness over all the sample as shown in fig.5.19b, in particular it is possible to see that in correspondence of edges (blue circles) the resist results very uniform. In the white circle it is possible to see that the resist uniformity is completely indipended on the non-rounded shape of the sample. Using the described chuck and plate the stripes could be deposited over the whole surface and with a space between stripes edges and crystal edges < 100 µm . In order to collect all the generated carriers it is important that the strips extend up to the edges of the sample as much as possible.

5.9.7 Contacts deposition

Every contact geometry can be transferred to the sample surface by means of photolithography (as previously discussed) or, for simple geometry, using mechanical masks. Mechanical masks allow only simple geometries and the resolution of the edges is quite poor with respect to other techniques and, for preparation of 3D detectors, cannot be used. Photolithography can instead be applied to any desired contact shape. In particular, after the photolithography process with a negative resist, sample surface is uncovered where illumination occurs (transparent parts of the mask) and covered by the hard resist in all other parts. The parts without resist are therefore ready for the deposition of the metal contacts or any other layer (for example alumina).
Several techniques for deposing contacts are available, for this project both electroless and evaporation techniques were used.
To deposit anodes and cathodes stripes (collecting electrodes) the electroless depositions was use. Electroless technique is described in more details in section 5.3.3.

5.9.8 Gold contact deposition by thermal evaporation

To deposit the gold drift stripes on passivated surface or alumina layer the thermal evaporation technique was performed in a ultra-high vacuum chamber. The samples were mounted in the chamber and then a primary vacuum is obtained using a zeolites pump (the average vacuum is 10-3 mbar). The secondary vacuum was achieved with a cryopump, at this stage the vacuum reaches 10^{-9} torr. The gold charge was positioned on a molybdenum melting pot and then evaporated

by Joule effect. The vacuum chamber was equipped with a in-situ system for monitoring the deposited layer. For CZT samples a 800Å of gold were deposit.

5.9.9 Surfaces Passivation

The reduction of surface currents is a main concern in the detector fabrication. Several solutions have been proposed in the literature, most of them including the use of H_2O_2 as oxidizing agent. At IMEM we use a new technique to deposit thin film of alumina (Al_2O_3) at room temperatures (RT) on CZT surfaces.
The standard aqueous solution of $NH_4F + H_2O_2$ (3%) was used for passivating all the surfaces of the samples. This procedure was done after the deposition of collecting electrodes by dipping the sample inside the solution for 6 min. After the passivation the sample was cleaned with bi-distillated water and than washed in acetone and isopropanol. More details of the passivation technique are described in section 5.3.4.

5.9.10 Alumina Layer

Despite its good properties, CZT requires special contact geometries in order to improve the energy resolution using the so called "single charge" techniques. As discussed in the chapter 3 this is possible using pixels and stripes with at least one (length or width) dimension smaller than the thickness of the detector. Moreover this segmentation open also the possibility of making 2D and 3D imaging detectors. Nevertheless two main problems affect CZT detectors with patterned contacts:

- The resistivity of the surface is always smaller compared with the bulk resistivity ($> 10^{10}\Omega cm$). The noise associated with the surface currents may deteriorate the energy resolution of the detector. This also because the distance between electrodes is normally very small (10 to 100 um) and the electrical resistance between electrodes may result to be low.

- In some devices (for example drift stripes detectors, in coplanar grid de- vices and in pixel detectors with steering grid) there is a voltage difference between different electrodes in order to collect all the charge only from the electrodes of interest (more positive the electrodes for collecting electrons). The voltage drop between electrodes can increase the noise associated with the current in a dramatic way.

The surface resistivity can be increased for example using an efficacy passivation technique. Unfortunately in some cases the standard passivation is not enough to decrease these currents. For this reason and in particular for the 3D detector project a novel approach was used. The idea was to deposit an additional insulating layer with resistivity higher than the native CZT oxide directly on the CZT material. This idea is not new and it was already proposed in literature to overcame the problem of noise related to the steering grid in pixelated detectors [53][54]. In 3D detectors (also in pixel detectors) there are always both collecting and non collecting electrodes at different potential on the anode surface of the detector. In order to reduce the leakage current between electrodes a thin layer of high-resistivity material can be deposit on the surface of the

CZT between the crystal and the non-collecting electrodes. I. Jung proposed alumina as good material for these types of applications. This because alumina has high resistivity value and has a good chemical and mechanical stability. The main difference in this work in comparison with the work of Jung was the novel approach to deposit alumina on CZT. In particular a growth technique called Pulsed Electron Deposition (PED) was used.

5.9.11 PED technique

In thin film technology a lot of deposition methods have been studied and still used, also for industrial production of thin film-based devices. Vacuum deposition technique can be grouped in two main categories: physical vapour deposition (PVD) and chemical vapour deposition (CVD). Among PVD processes there are also sputtering and evaporation. In physical vapor deposition (PVD) processes, the coating is deposited in vacuum by condensation from a flux of neutral or ionized atoms of material. These deposition processes require the use of very good vacuums system. The CVD process use some gaseous precursors that react directly on the substrate. The problems related to this technique are due to: reactant costs and toxicity and the low control of chemical, structural and morphologic homogeneity along the whole film.
Pulsed Electron Deposition is a process in which a pulsed high power electron beam penetrates approximately 1 µm into the target. The result is a rapid evaporation of target material that generates a plasma. The non-equilibrium extraction of the target material (also called ablation process) facilitates stochiometric composition of the plasma. Under optimum conditions, the target stoichiometry is thus preserved in the deposited films and this represents the main advantage of this technique (shown in fig.5.20b).
In contrast to conventional technique as conventional e-beam evaporation, the main feature of the pulsed systems is the ability to generate a high power density of $\sim 10^8 W/cm^2$ at the target surface. As a result, thermodynamic properties of the target material such as the melting point and specific heat become unimportant for the evaporation process. This is particularly advantageous in the case of complex, multi-component materials. As in the case of Pulsed Laser Deposition (PLD), the Pulsed Electron Deposition (PED) technique provides a unique platform for depositing thin films (1 nm to 5 µm) of complex materials on a variety of technologically important substrates, with a unique strength of extending the range of materials and applications.

Another very important characteristic of PED deposition is that Al_2O_3 can be deposited also at room temperature. This characteristic is very important for two main reasons: i) as mentioned above CZT material is very sensitive to the temperature and normally it is better to operate at temperatures lower than 100°C, ii) The properties of the photoresists (in particular adhesion and stability) are not altered if a room temperature process is used.
The fundamental steps of PED technique (shown in fig.5.20a) can be summarized as:

1. The electron beam generation is initiated by a pulse of auxiliary low current gas discharge. The pulse is controlled by a trigger with a 10 Hz frequency.

2. The plasma penetrates into the hollow cathode (gas pressure inside 1-3 Pa) that is connected to the plate of a low-inductance capacitor, to which a negative static potential (16

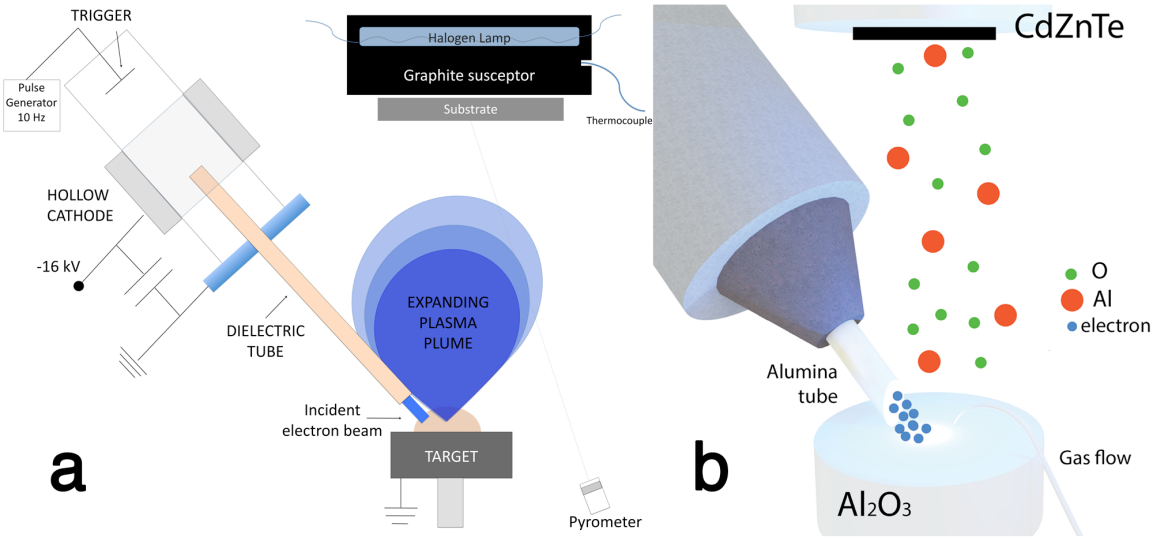

Figure 5.20: *a)PED scheme. b)PED setup for Al_2O_3 deposition on CZT samples.*

KV) is applied. The plasma excites emission from the hollow cathode surface.

3. A ceramic tube plays the role of a channel ensuring directivity of the beam, providing the electric insulation, and protecting the cathode from contamination with the beam erosion products.

In IMEM-CNR institute the PED technique was developed for $CuIn_xGa_{(1-x)}Se_2$ (CIGS) based solar cells research[56].

5.9.12 Attachment Method and Bonding

Semi-automatic procedure to attach the detector to the alumina PCB and make the electrical bonding was developed during this project. This procedure is consisted by different steps:

1. First of all the detector was aligned to the PCB on a reference plane assumed to be perfectly planar.

2. After that the detector was perfectly aligned with the pads of the PCB, this was possible using a digital microscope automatically moved.

3. When the detector was aligned to the pads it was fixed to the PCB using space qualified high resistivity epoxy glue.

4. A special copper comb was aligned with detector stripes and PCB pads and than soldered to the PCB pads (fig. 5.21a).

5. In order to bond all the 49 anode and drift stripes a semi-automatic process was develop. A special copper comb was aligned to the PCB pads and the stripes of the detector. This copper comb was soldered on the PCB side with a special soldering paste. On the side of

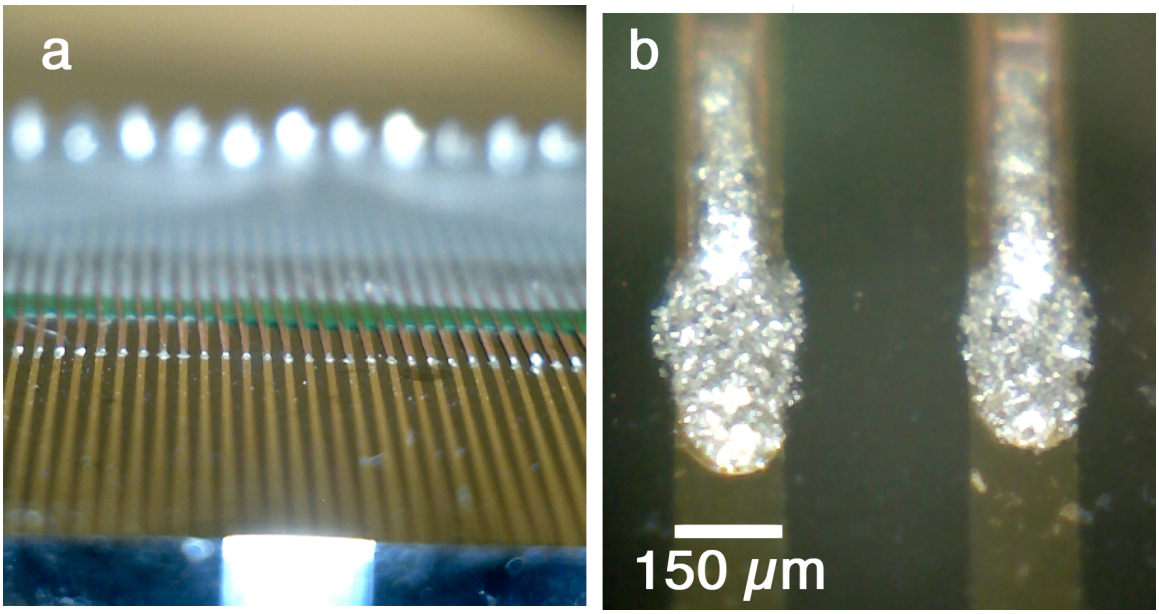

Figure 5.21: a) The copper comb bounded on detector stripes with epoxy glue, b) typical bondings made by the automatic machine.

the detector the comb was connected using automatic machine that connected the comb to the stripes of the detector using a special glue (fig. 5.21b).

6. The cathodes stripes were connected using copper wires soldered on PCB side and attached with conductive epoxy on the detector side (this proce- dure was carried out by manually controlling an especially developed tool).

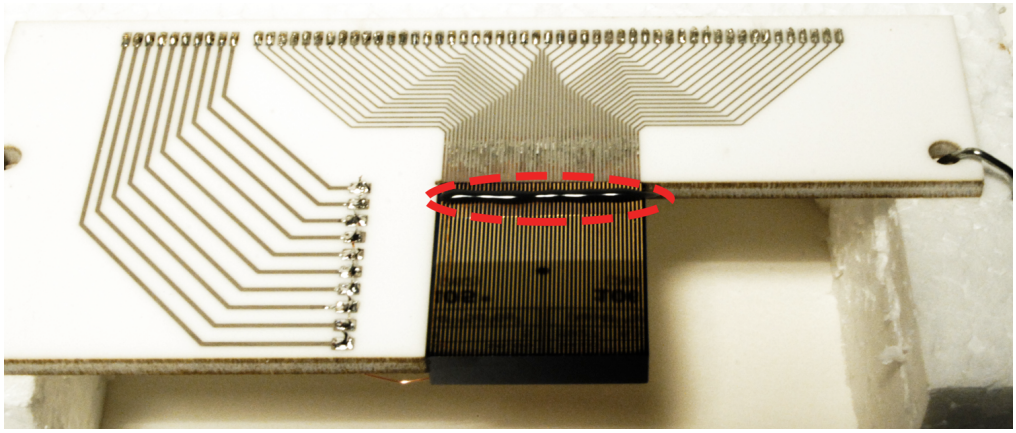

Figure 5.22: *The completed detector plus PCB, the red circle indicates the extra epoxy glue for covering bonding on CZT.*

In order to reduce the noise in the system and to increase the mechanical stability of the PCB in this project alumina PCBs (3 mm thick) were used. Alumina, in fact, guarantees a high rigidity to the PCB reducing the leakage currents between pads. Nevertheless all the soldering procedures

are more complicated because of the highly thermal conductibility of the alumina. The main features of this process are: low operation temperature ($<$ 100oC), high precision bonding (typical contact area 50µm x 50µm) and very good alignment between detector surface and PCB surface. Moreover high stability electrical connections were achieved adding high resistivity epoxy glue on the bonding on CZT as shown in fig.5.22. This cover layer was fundamental for the stability of the either system.

5.10 3D CdZnTe Characterization

5.10.1 Alumina Resistivity

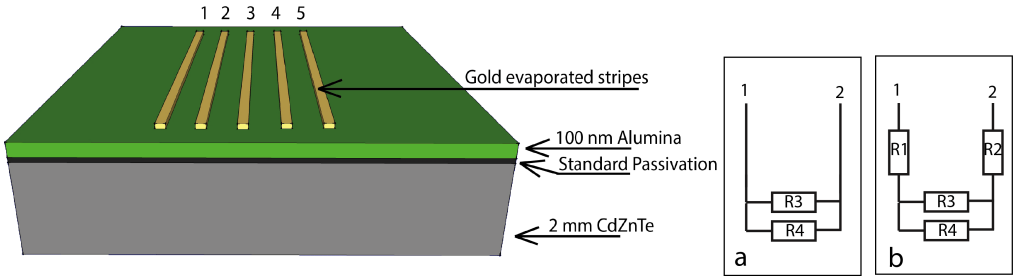

Figure 5.23: CZT detector with the alumina layer between gold stripes and passivated surface. On the right the equivalent electric circuit.

In order to extrapolate the resistivity of the alumina, a 100 nm Al_2O_3 (green layer on fig.5.23) was deposited by PED on standard passivated CZT sample (2 mm thickness) before processing the definitive detectors. Five gold stripes (60 nm thickness) were evaporated on alumina layer, having 250 µm width, 15 mm length, and with 250 µm pitch.
The CZT sample was passivated with the standard procedure described in the previous section. Without alumina layer, the resistance between stripes in a normal passivated CZT detector depends on the values of R3 and R4 (fig.5.23 (a)). R3 is the resistance due to the surface and R4 is the bulk resistance. Being these two resistors in parallel, the lower resistance (R3) controls the current value. For this reason, the addition of the two resistors in series (R1 and R2 fig.5.23 (b)) due to the alumina layer can decrease the total current of the circuit. The IV characteristics between two adjacent stripes are shown in fig.5.24. The IV characteristics are the same for all the stripes and clearly confirm that the thickness and the resistivity of the alumina layer are almost uniform. Considering the geometrical parameters a resistivity in the order of $5 \div 6 \cdot 10^{13} \Omega cm$ can be extracted in low voltage range.
Using this alumina extra layer the currents between stripes are comparable with the bulk current that normally are in the range $5 \div 15$ nA. As shown in fig.5.24 the gold-alumina contact has blocking characteristic, thus decreasing further the value of currents at high voltages.
The Al_2O_3 layer deposited by PED shown other very interesting properties:

1. The film shows very good adhesion to CZT passivated surface.

2. The layer was very uniform over all over the surface. Thickness variations in the order of

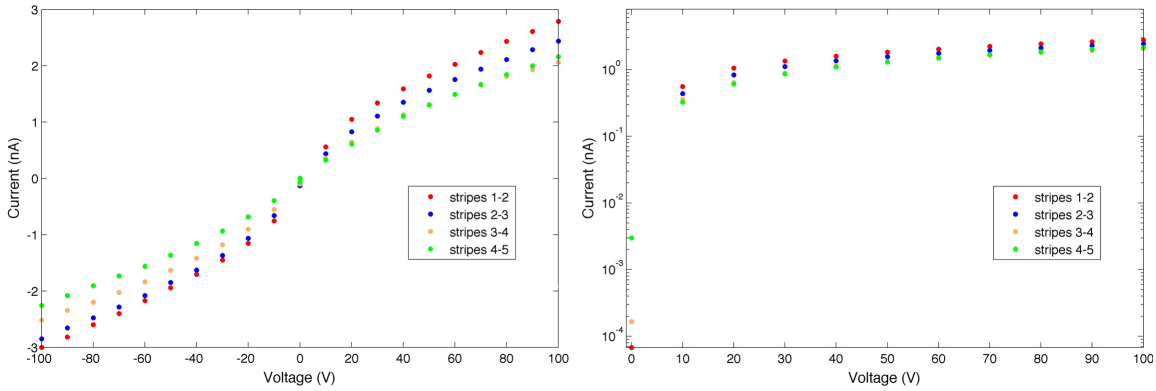

Figure 5.24: *Linear (left) and semi-log (right) IV characteristic of the stripes of fig.5.23.*

5% on 20mmX20mm area were measured with a standard profilometer.

3. The quality of the layer was very good also for room temperature deposition.

4. Evaporated gold contacts shows good adhesion on alumina layer (much stronger adhesion than evaporated gold on CZT surface).

5. PED deposition was compatible with the standard photolithography process. In particular the photoresist, after the Al_2O_3 deposition, was very easy to remove.

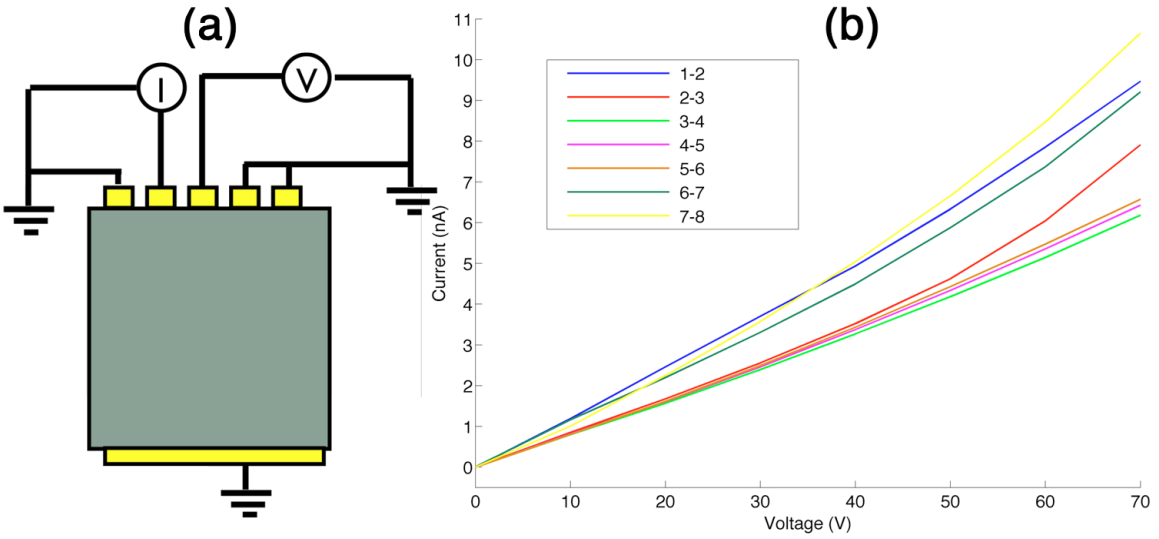

Figure 5.25: *a) I-V experimental setup used for preprototype characterization. b) I-V characteristics of the stripes.*

The effect of the extra layer of alumina on can be understood by comparing the IV characteristics of fig.5.24 with the IV characteristic (fig.5.25 (b)) of the preprototype sample made in 2011 (a picture of the sample is shown in fig.5.16 left). Both detectors were characterized by stripes of the same dimensions and same pitch. Therefore the IV characteristics measured between

adjacent stripes can be compared. In fig.5.25 (a) the experimental setup used for the IV stripes characterization of preprototype sample. As shown in fig. 5.25 (b) with the normal passivation process the current are 4-5 times higher than those of the alumina detector (shown in fig. 5.24).

5.10.2 I-V measurements

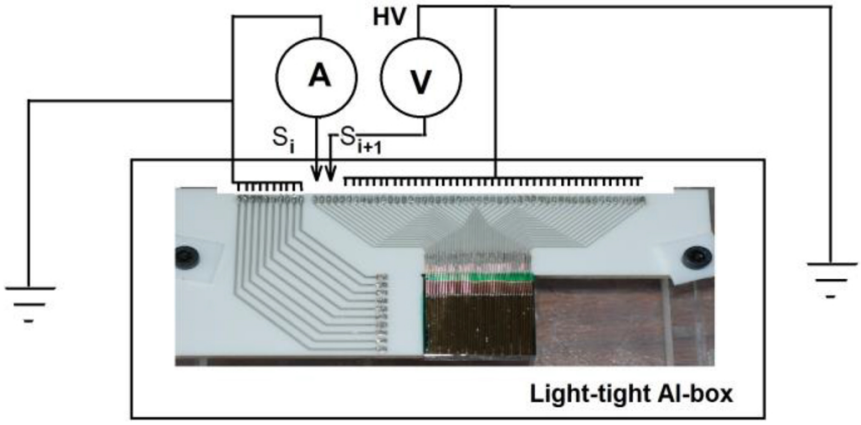

Figure 5.26: *Experimental setup for surface currents measurement.*

The requirement for the allowable surface leakage current between two 20 mm long strips with 0.15 mm width and 0.25 mm gap was <4 nA at applied -100 V on one strip and measuring return current on the near strip at T=22 C. For the bulk leakage current between cathode strips and one 20 mm long strips with 0.15 mm width and 0.25 mm gap requirement was < 2 nA at applied -100 V, always at T=22 C. All IV measurements were done at IMEM institute, then repeated and verified at DTU Space.

Fig. 5.26 shows the surface leakage current measurement setup. For the surface leak- age current measurements, all strips (including cathode strips) were held at ground potential except S_i and S_{i+1}. Surface leakage current were recorded between S_i and S_{i+1} with HV (-100 V). The measurement was repeated for all strips by shifting S_i and S_{i+1} to the right.

Fig. 5.27 shows bulk leakage current measurement setup diagram. For the bulk leakage current measurements, cathode strips were biased with HV (typ. -100 V or -500 V). Bulk current between cathode and S_i was recorded while the other strips help at ground potential. The measurement was repeated for all strips by shifting S_i to the next strip.

Tab.5.28 and 5.29 show the measured leakage current data for the DTU2 detector measured during ESRF synchrotron experiments. As it can be see from that tables, very good results were obtained. About surface leakage current, DTU2 shows very low currents between adjacent stripes, except for strip Nr. 21-22 that was 16.80 nA. The only other out-requirement value is for strip Nr. 29-30 that with its 4.67 nA at -100 V exceeding the target value (4 nA) for only a small amount. About bulk leakage current measurements, DTU2 completely fulfill requirement of 2nA currents at -100 V of applied bias, except for stripe 35 that behave 4.45 nA.

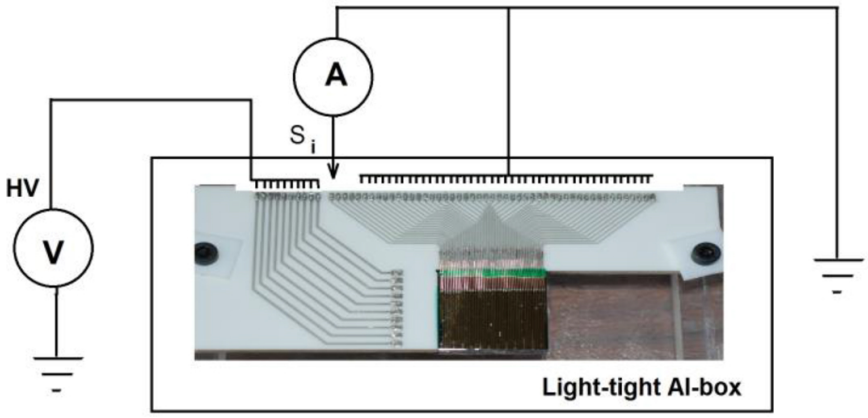

Figure 5.27: *Experimental setup for bulk currents measurement.*

Strip Nr.	**1-2**	**2-3**	**3-4**	**4-5**	**5-6**	**6-7**	**7-8**	**8-9**	**9-10**	**10-11**
Current (nA).	1.10	1.03	0.86	0.86	0.86	1.07	0.83	0.86	0.84	1.10
Strip Nr.	**11-12**	**12-13**	**13-14**	**14-15**	**15-16**	**16-17**	**17-18**	**18-19**	**19-20**	**20-21**
Current (nA).	0.87	0.85	0.89	1.16	0.97	1.09	1.50	1.15	3.28	1.52
Strip Nr.	**21-22**	**22-23**	**23-24**	**24-25**	**25-26**	**26-27**	**27-28**	**28-29**	**29-30**	**30-31**
Current (nA).	16.80	1.73	1.60	1.08	1.31	1.46	1.11	1.16	4.67	1.42
Strip Nr.	**31-32**	**32-33**	**33-34**	**34-35**	**35-36**	**36-37**	**37-38**	**38-39**	**39-40**	**40-41**
Current (nA).	1.18	1.63	1.30	1.53	1.30	1.44	1.28	1.55	1.22	1.26
Strip Nr.	**41-42**	**42-43**	**43-44**	**44-45**	**45-46**	**46-47**	**47-48**	**48-49**		
Current (nA).	1.45	1.62	1.31	1.51	1.68	3.98	3.62	3.27		

Figure 5.28: *Surface leakage current values measured on Detector DTU2 (measured also at ESRF) (HV = -100 V, T=22 C).*

5.10.3 ESRF synchrotron experiments

Due to the limited amount of time available at the European Synchrotrone Radiation Facility (ESRF) characterizations were performed only for one detector (DTU2) of four. Experiments were carried out at ESRF at the beam line 15A. This beam line provides an high intensity beam in a wide energy range (100-600 keV). The aim of this type of experimental investigations on CZT drift strips detector was to demonstrate that CZT drift strips detector combines a good energy resolution with 3D sensing capabilities of this detector configuration. Fig.5.30 shows a real picture of the CZT drift strips detector used for the ESRF synchrotron beam test experiment. It is worth repeating that CZT drift strips detector realized on spectroscopic grade material from Redlen with size of 20 x 20 x 5 mm3. The strip pitch was 400 μm with 150 μm of strip width and consist of the Au layer as described above.

Detector calibration

Detector system was energy calibrated at DTU Space using Am-241, Co-57, Ba-133 and Cs-137 radiation sources. Calibration was then repeated and verified using Ba-133 at ESRF. The gain and offset for the cathode and drift strips were all adjusted for the experiment.

Strip Nr.	**1**	**2**	**3**	**4**	**5**	**6**	**7**	**8**	**9**	**10**
Current (nA).	0.62	0.39	0.17	0.09	0.09	0.09	0.10	0.09	0.09	0.08
Strip Nr.	**11**	**12**	**13**	**14**	**15**	**16**	**17**	**18**	**19**	**20**
Current (nA).	0.10	0.08	0.06	0.06	0.09	0.06	0.09	0.10	0.13	0.09
Strip Nr.	**21**	**22**	**23**	**24**	**25**	**26**	**27**	**28**	**29**	**30**
Current (nA).	0.11	0.13	0.18	0.13	0.15	0.13	0.22	0.13	0.10	0.10
Strip Nr.	**31**	**32**	**33**	**34**	**35**	**36**	**37**	**38**	**39**	**40**
Current (nA).	0.13	0.11	0.16	0.17	4.45	0.12	0.13	0.11	0.12	0.12
Strip Nr.	**41**	**42**	**43**	**44**	**45**	**46**	**47**	**48**	**49**	
Current (nA).	0.09	0.07	0.07	0.04	0.04	0.05	0.05	0.05	0.05	

Figure 5.29: *Bulk leakage current values measured on Detector DTU2 (measured also at ESRF) (HV = -100 V, T=22 C).*

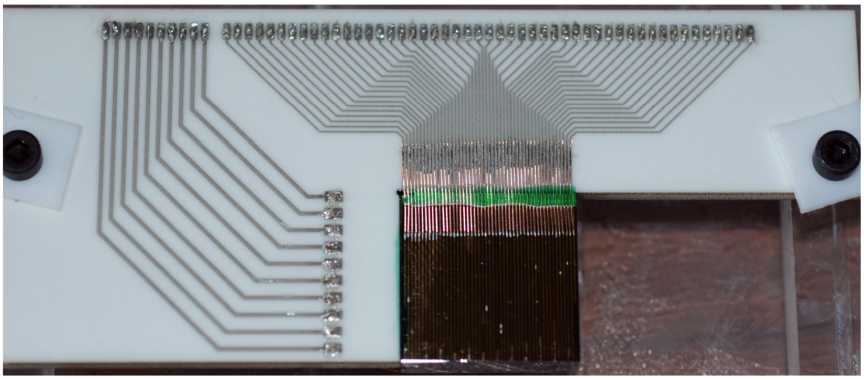

Figure 5.30: *3D CZT drift strips detector mounted on alumina PCB used for ESRF beam test.*

ID15A beam profile

The beam at ESRF was shaped by using two different tungsten collimators in the optical hutch, in front of the white beam and the second in the experimental hutch, after the monochromator. The beam was adjusted and shaped to be about 50 μm x 50 μm size for the selected energies respectively of 150 keV, 300 keV, 400 keV and 580 keV.

2D Scans

A number of 2D scans were performed on the selected detector on plane x-y and z-y. Before each scan, it was necessary to perform the beam preparation including changing beam energy, intensity adjustment and beam start position check. The last check is necessary since changing the beam energy can result in position shift for the beam. All these preparation work toke an average amount of time of about 2 hours.

At high energies (>500 keV), the intensity drops from 10^3 to 10^2 photons (for 50 μm square beam) so recording time for high energies were adjusted to record at least 10^3 events for each beam position at high energies. The readout strips and the segmented cathode were connected to eV5093 preamplifiers. CZT drift strips detector with its PCB, the preamplifier and the passive components PCB are enclosed in a special box, placed onto the xyz translational stage as depict

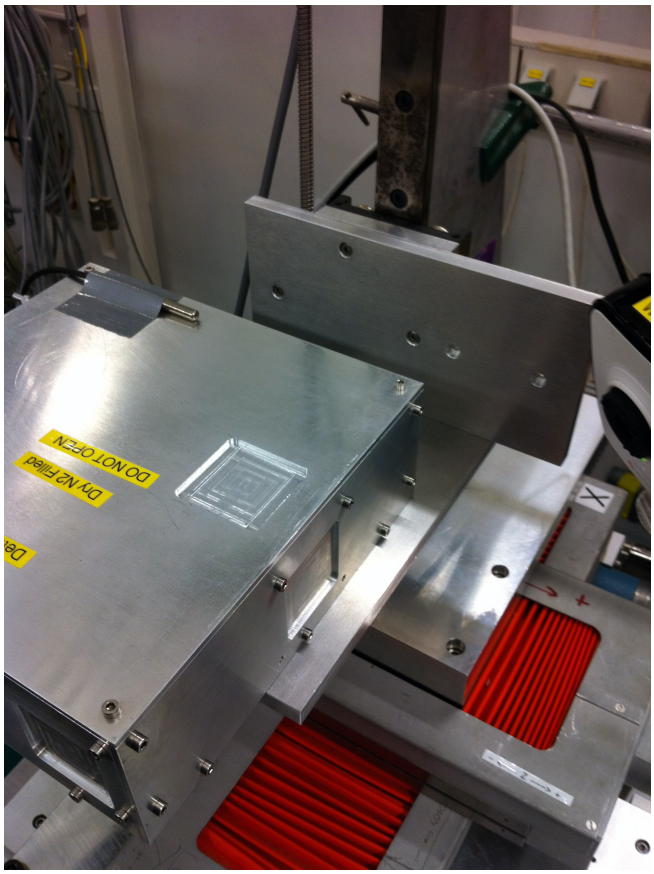

Figure 5.31: *Detector box mounted on mechanical translational xyz-stage at ESRF.*

in fig.5.31 . This system is capable of moving the detector box in 3 directions, controlled by a DTU developed program. Its main function is to record detector data for 2D scan in an autonomous way based on user-defined parameters. The scan software contains a main program, which interfaces and controls the data acquisition (DAQ) software and the xyz-stage controllers.
Each scans was performed in the "side illumination" configuration, the so-called PTF (Photon Transverse Field). Photons enter the detector perpendicular to its side; this mode has the advantage that photons can be absorbed in the full length of the detector (20 mm) while the created charge at most will drift through the thickness of the detector (5mm). Therefore this detector illumination mode will provide high efficiency, preserving the excellent spectroscopic performances obtained for the CZT drift strip detectors. At each energy all scans were repeated on the same scan area which cover only 4 of the 12 drift cells as shown in fig.5.32 . Signals from 4 anode strips, the relative non collecting grids and 8 (of 10) cathode strips were collected for each events, resulting in about 15 thousands recorded events for each position of the scan.

x-y scans illumination in PTF configuration

In the first experiment, the synchrotron beam impinged on the lateral surface of the detector, with anode strips perpendicular to it as represented in fig.5.33 . It's worth repeating that all the scans for different energies were repeated on the same scan area which cover only 4 of the 12

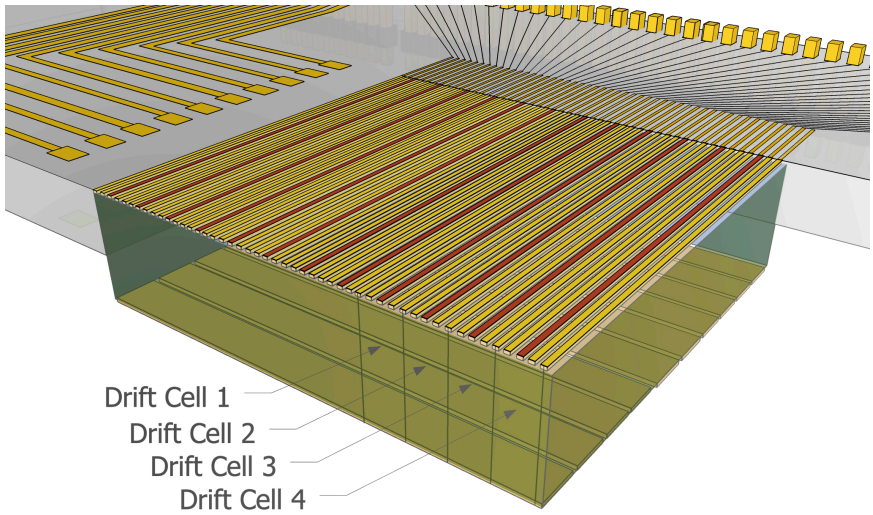

Figure 5.32: *The four drift cells used for all the measurments at ESRF.*

drift cells, on x-y plane with 25 steps of 200 μm along x direction and 28 steps of 200 μm along y direction, covering 5.0 mm x 5.6 mm scan area.
One 2D scan approximately takes a total time of about 2 hours. Overhead time is the fixed time for the software developed by DTU to save the recorded data in a file and move the beam to a new position and start the recording again.

z-y scans illumination in PTF configuration

In the second experiment, the synchrotron beam impinged on the lateral surface of the detector, with cathode strips perpendicular to it as represented in Fig.5.34. All the scan for different energies were repeated on the same scan area in the z-y plane with 40 steps of 600 μm along z direction and 5 steps of 800 μm along y direction, totally covering 24 mm x 4 mm scan area.

Energy scans

In order to investigate position resolution function of energy in 3D, we have performed energy scans with beam illumination on same position on the detector in x-y plane and z-x plane. Beam energies used for both planes are:150 keV, 200 keV, 225 keV, 250 keV, 275 keV, 300 keV, 350 keV, 400 keV, 450 keV, 500 keV, 550 keV and 600 keV.

5.10.4 Results and discussion

In the following sections 3D position capabilities, spectral performance and amount of charge sharing will be achieved from the ESRF acquired data.

5.10.5 3D position capabilities

It's worth repeating that not only the drift strip readout technique provide an improved energy resolution for CZT detectors, but it also yields information about the interaction depth of the

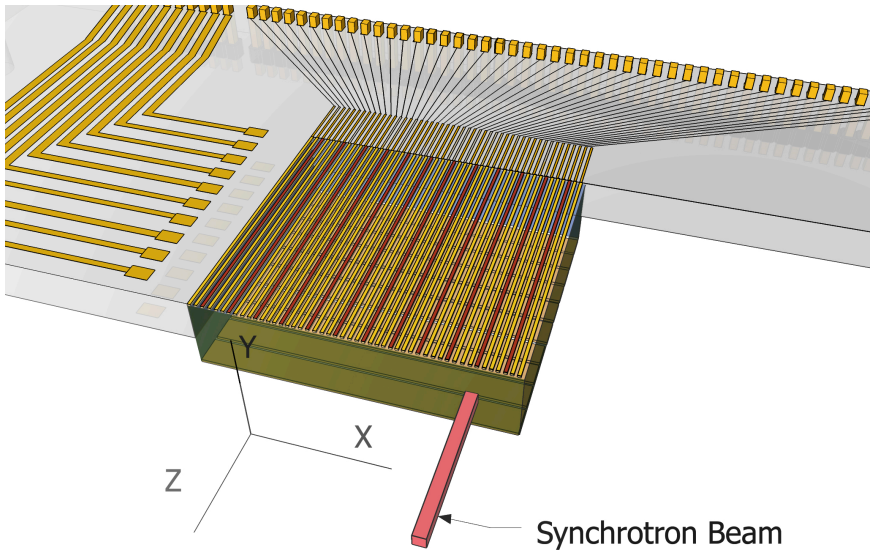

Figure 5.33: *Geometry of the x-y scan experiment.*

detected photon.

Resolution along Y direction

First of all the problem of the resolution along Y direction will be considered. This parameter can be determined using the set of data from the first experiment (2D scan data in x-y plane). The so-called depth information (depth sensing) in the Y-direction can be derived in this case, at a given energy, for each event, from the ratio:

$$Y_{pos} = \frac{\sum_{n=1}^{8} SC_n}{SA_m}$$

where SC_n is the signal related to n-cathode and SA_m is the signal relative to the anode that showed a signal different from zero so, in other terms, the signal from the drift cell in which the event occur. In the case that more than one anode shows a signal different from zero (charge sharing effects), the signal from the two quantities are summed.
The quantity Y_{pos} is almost linearly dependent on the photon interaction depth, with a value close to unit for interaction close to the cathode and a value close to zero for interaction near the strip electrodes. Real position in Y-direction can be calculated using $Y_{pos} \cdot L_d$ where Ld is the detector thickness.
For each beam position, the centroid of the distribution of the events (Gaussian) represents the position of the beam along the Y-axis and FWHM of the Gaussian represents the resolution in the Y-direction.
The value Y_{pos} linearly depends on the beam position along the Y-axis as shown in fig.5.35, with a value close to unity for interactions close to cathode and a value close to zero for interaction near strip electrodes. This demonstrates that the value of Y_{pos} can be used for the absolute determination of the beam position along the Y axis. In this plot, data points shown for 2D scan

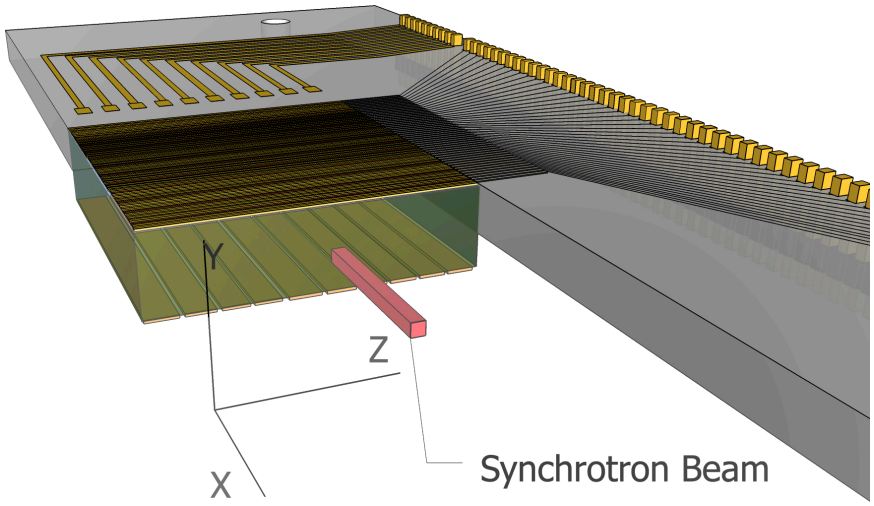

Figure 5.34: *Geometry of the z-y scan experiment.*

point in the anode A11 section at x=10, y=0...24 for all energies. Measured beam positions are the peak centroids after the fitting procedures described above. There is an offset shift between data for different energies caused by the different scan start positions (around ± 0.2 mm). As pointed above, the measured position resolution in the Y direction is dependent and affected by the finite beam size, electronic noise and the dimension of the electronic cloud generated by the absorption event.

Fig.5.36 shows position resolution in Y-direction as function of energy. The plot indicates a strong photon energy dependency for the position resolution and it has a minimum at ∼0.2 mm FWHM at 400 keV. At higher energies (> 500 keV), the detector position resolution decreases with increase of the dimension of the electronic cloud generated in the detector material. The photoelectron absorption length increases together with its kinetic energy thus it creates larger electron cloud size. At low energies, position determination is mainly dominated by signals uncorrelated electronic noises. Therefore, a better electronic noise performance in the system will provide an improved position resolution at low energies. On the contrary, only the material properties can determine the photoelectron absorption length and the resolution at high energies.

Resolution along X direction

Also in the case of resolution determination in X direction, data from the first experiment (x-y scans, illumination in PTF configuration) were exploited. For each scanning point, at fixed energy, the drift cell of interest must be determined. Details on the position determination in X-direction are object of the patent EP13194445 deposited by DTU Space and cannot be revealed yet.

For XY positions, the measured beam position linearly depends on the real beam position along the Y-direction but for the X-direction, the measured beam position dependency is non-linear and depends on the Y-position.

In any case it is possible to calibrate and perform position correction for the detector using 2D scan data. This requires performing a 2D scan with fine collimated beam and fine steps in both

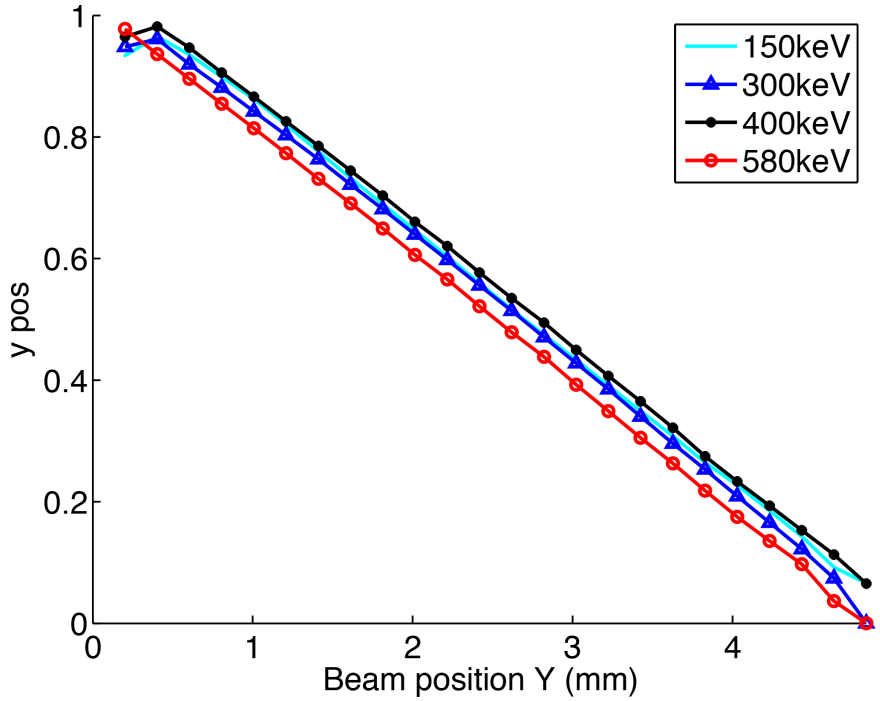

Figure 5.35: *The measured and derived Y_{pos} value versus depth for energies 150 keV, 300 keV, 400 keV, and 580 keV.*

direction. This is demonstrated in this project using ESRF 400 keV x-y scanning data (anode 11 area, shown in fig.5.37). A look-up table was created from correlating measured beam positions (fit results as averaged positions from X and Y direction) and actual beam positions (step of 0.2mm in both directions). Corrected positions (Xc,Yc) are obtained from this look-up table using bi-linear interpolation. The look-up table applied on the ESRF 400 keV x-y scan result is shown in fig.5.37. Here, data from only each second beam positions are shown (0.4 mm distance between beam spots in both directions). Beam is resolved very well with 0.2 mm FWHM in both directions.

Resolution along Z direction

In order to obtain the resolution in the Z direction, 2D scan data in the z-y plane from the second experiment were exploited. For each scanning points at fixed energy, and for every photon interaction, the signals induced on the 8 cathodes are used for finding the centroid position as Z_{pos}.

$$Z_{pos} = \frac{\sum_{n=1}^{8} n \cdot SC_n}{\sum_{n=1}^{8} SC_n}$$

where SC_n is again the cathode strip signals. The histogram of the obtained maxima for all the events recorded at a fixed beam position fitted again with a Gaussian. The width of the obtained Gaussian is the resolution in the Z direction. The Z resolution of the detector can be studied for different positions in the detector and for different energies.

After data processing the position resolution in Z direction is obtained. As an example, the

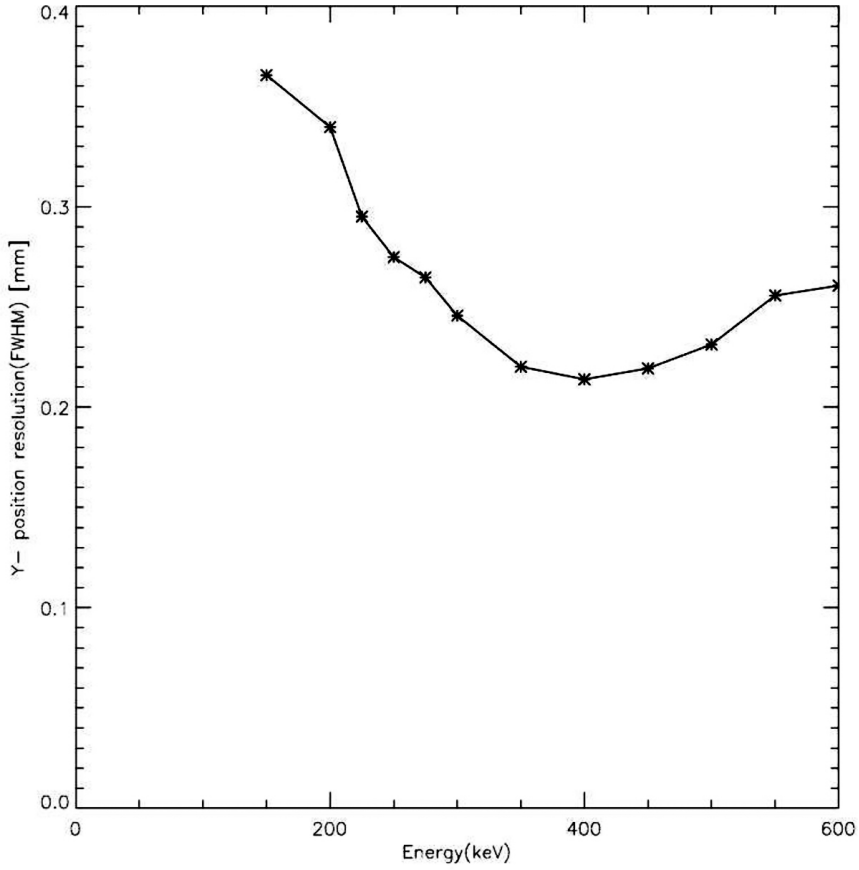

Figure 5.36: *Position resolution along the Y direction as function of energy.*

signal recorded by 8 cathodes, in a single photon event, is reported in fig.5.38 (a), together with the total Gaussian fitting. An average position resolution around 0.6 mm FWHM is measured for (200 ÷ 600) keV energy range, which is ∼1/3 of the cathode strip pitch. The calculated value of Z linearly depends on the beam position along Z axis as shown in fig.5.38 (a). This demonstrates that the value of Z as determined by the described procedure can be used for the absolute determination of the beam position along Z axis. Fig.5.38 (b) shows the detectors measured position resolution as function of energy in Z-direction.

Spectral performance

The ESRF monochromatize synchrotron beam is not 100% mono-energetic. For this reason, spectra of the beam were recorded for selected energies for the 2D scans by using a germanium detector.

In particular at high energy (600 keV), the energy spreading is not negligible (∼7 keV FWHM) and affects the energy resolution of the 3DCZT detector. As above mentioned a second effect that must be taken into account in order to correctly evaluate the detector energy resolution is the electronic noise of the readout chains. In order to determine electronic noise, detector is tested with an external pulser.

Eliminating all the sources of noise, energy resolution of 1.5% at 600 keV can easily be achieved

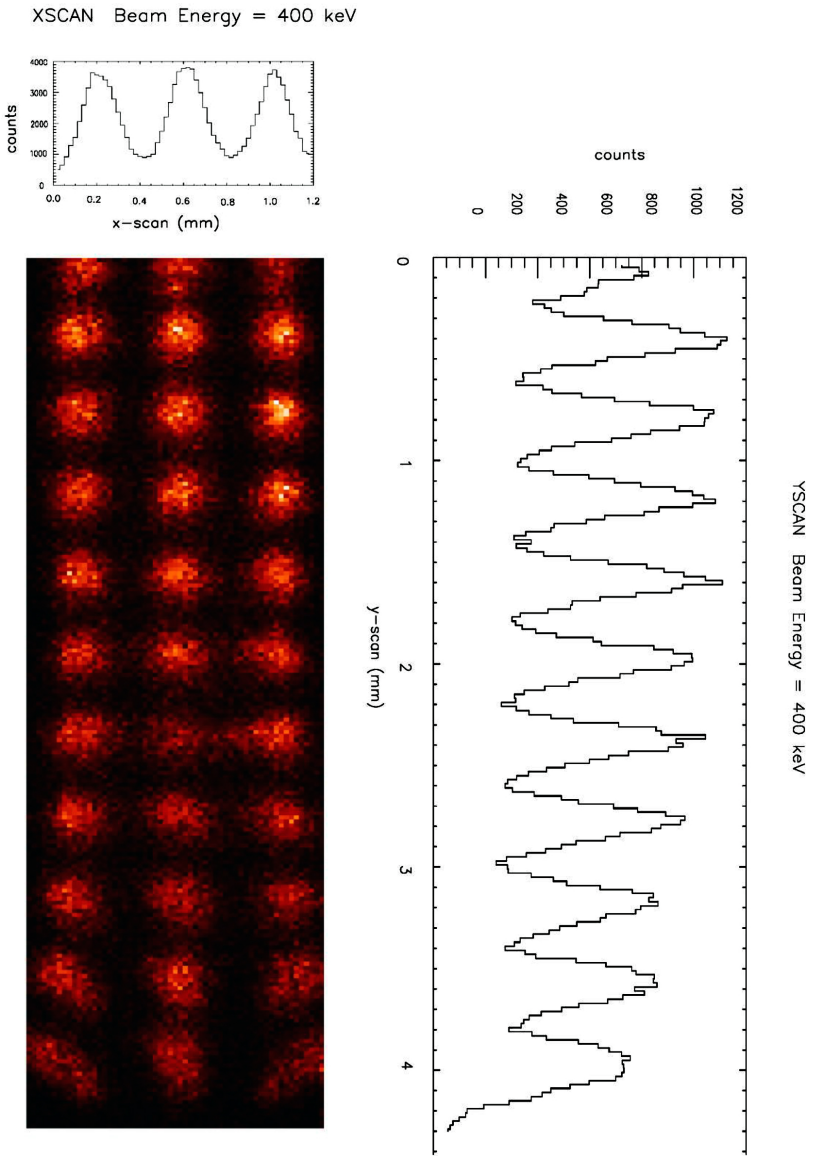

Figure 5.37: *400 keV x-y scanning corrected positions.*

and also improved, if position calibration table (including energy calibration) is adopted.

5.10.6 Charge sharing effect

The so-called "shared events" may occur when the beam is in the region between two adjacent anode strips where more than one anode shows a signal different from zero. In this case, a reconstruction procedure is processed. The anode with maximum signal is reconstructed with the sum of the anode signals involved in the event and the signals for all the other anodes are set to 0. The data analysis will provide statistics for the shared events. It is possible to calculate the percentage of these events where more than one anode shares the detector signal. The shared events are identified and reconstructed in the data analysis for each energy and 2D scans in x-y plane. Results for shared events statistics are shown as 2D map. In fig.5.39 the maps of charge

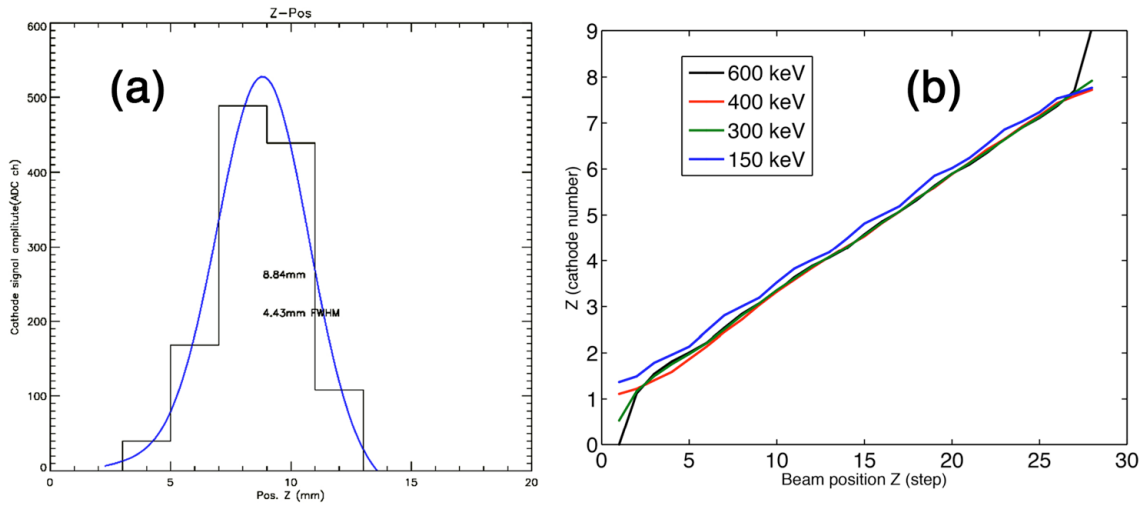

Figure 5.38: *a)Signal recorded by 8 cathodes in a single event, together with the Gaussian fitting. b)The measured beam position dependence of the actual beam position in the Z direction for a given value of Y position (2.0 mm from the cathode side) for all energies.*

sharing for the x-y scanning experiments at different energies is shown. For each point it is given the percentage of events that gave an appreciable signal on more than one anode. The maps clearly show that charge sharing effect is limited to regions between adjacent drift cells. The results show that shared events statistic is around $(5 \div 10)\%$ for energies (150÷600) keV. The energy resolution gets slightly worse for reconstructed shared events due to the sum of the signals with their uncorrelated noises.

5.10.7 Combined position sensing capabilities and energy determination

After an interaction of photon within the CZT detector, time coincident signals from all electrodes were recorded. Analyzing the data will provide energy, time and 3D position information for each event. 3D position information will be determined:

- Y-direction: ratio between anode signal and sum of all coincident cathode signals will provide the interaction position in y-direction.
- X-direction: triggered anode signal will provide the interaction position in x-direction and signal ratio between drift strip signals of the left side and right side of the triggered anode will provide the fine position.
- Z-direction: coincident signal amplitudes from 8 cathode strips will provide the interaction position in z-direction.

Fig.[5.40-5.41] show an example using above described procedure for x=10 and y=8 of 2D scans data for beam energies of 400 and 580 keV respectively. Plots show demonstration of 2D position capability of the detector when illuminated with the ID15A beam. Lower right plots show the spectral performance of the detector for different energies.
Upper left plots show 2D image of the D15A beam (50 μm x 50 μm). Upper right plots show

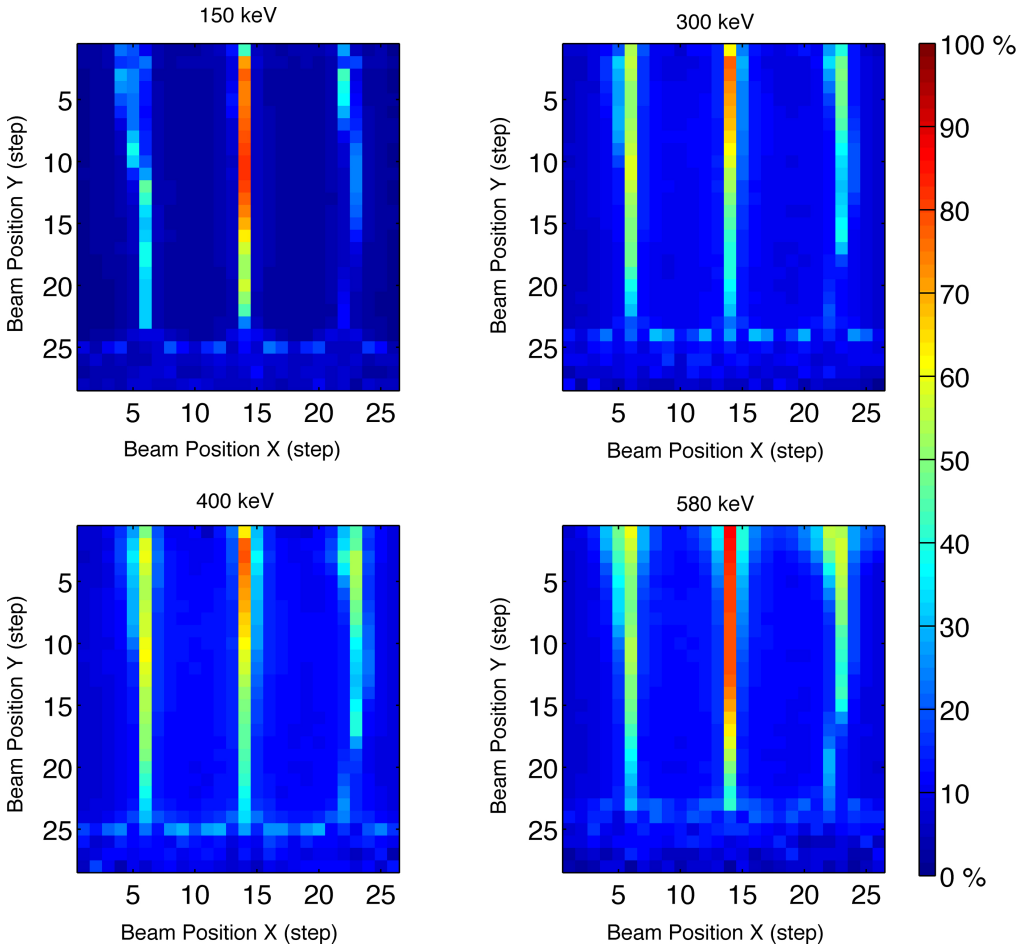

Figure 5.39: *Maps of charge sharing for the X-Y scanning experiments at different energies. For each point it is given the percentage of events that gave an appreciable signal on more than one anode.*

histograms of the measured Ypos values. Fitting this peak with Gaussian provides the measured beam position and the beam width as the peak centroid and its FWHM, respectively in Y-direction. Lower left plots show histograms of the measured Xpos values. Again here, we fit the peak with Gaussian and get the X-position and its FWHM. Each scan and for each beam position, this procedure is applied for all ESRF data.

5.10.8 Conclusion

3D position capability of the prototype detector has been demonstrated for X, Y and Z direction. Summary is shown in fig.5.42 for the X, Y, Z position resolution achieved by interpolation method. The result show that detector position resolution is mainly dominated by electronic noise of the readout chains at low energies (<200 keV). That means better position resolution can be achieved by improving the noise performance of the readout electronics. The measured detector spectral performance showed that the energy resolution is mainly dominated by energy spreading of the synchrotron beam. As discussed before the monochromatized synchrotron beam is not 100% mono-energetic and, at high energies (>400 keV), the energy spreading is not negligible (∼7 keV

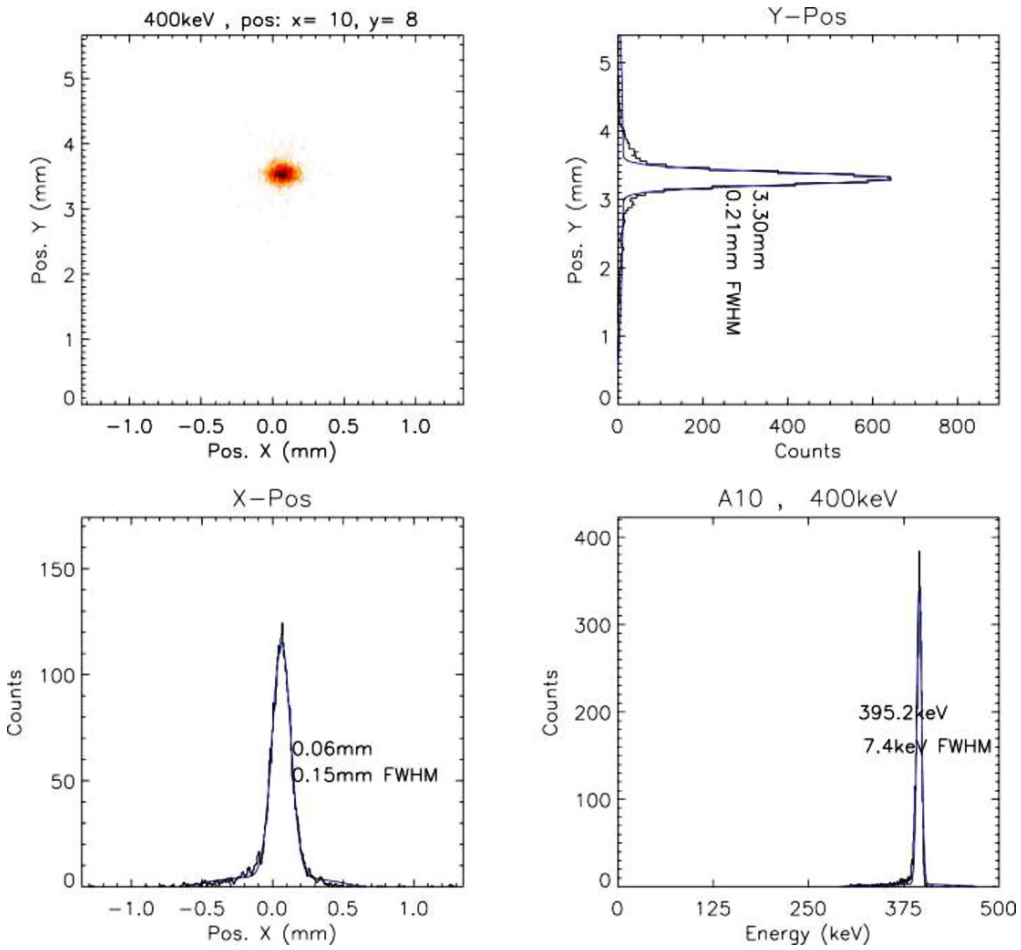

Figure 5.40: *Result for x=10 and y=8 of 2D scans data for 400 keV beam energy.*

FWHM) affecting the energy resolution of the 3DCZT detector. A second effect is the electronic noise of the readout chains. The measured and achievable energy resolution of the detector is also shown in fig.5.42 . These performance can be further improved by calibration using position information with known energies.

As we can see about charge sharing, the effect is limited into regions between two adjacent drift cells. Electron charge cloud from such events in the region collected by two anodes. Shared event rate increases with increasing energy since high energies create larger electron clouds. In this case, a reconstruction procedure is processed. The shared event rate is around $(5 \div 7)\%$ at 150 keV and $(10 \div 12)\%$ at 580 keV.

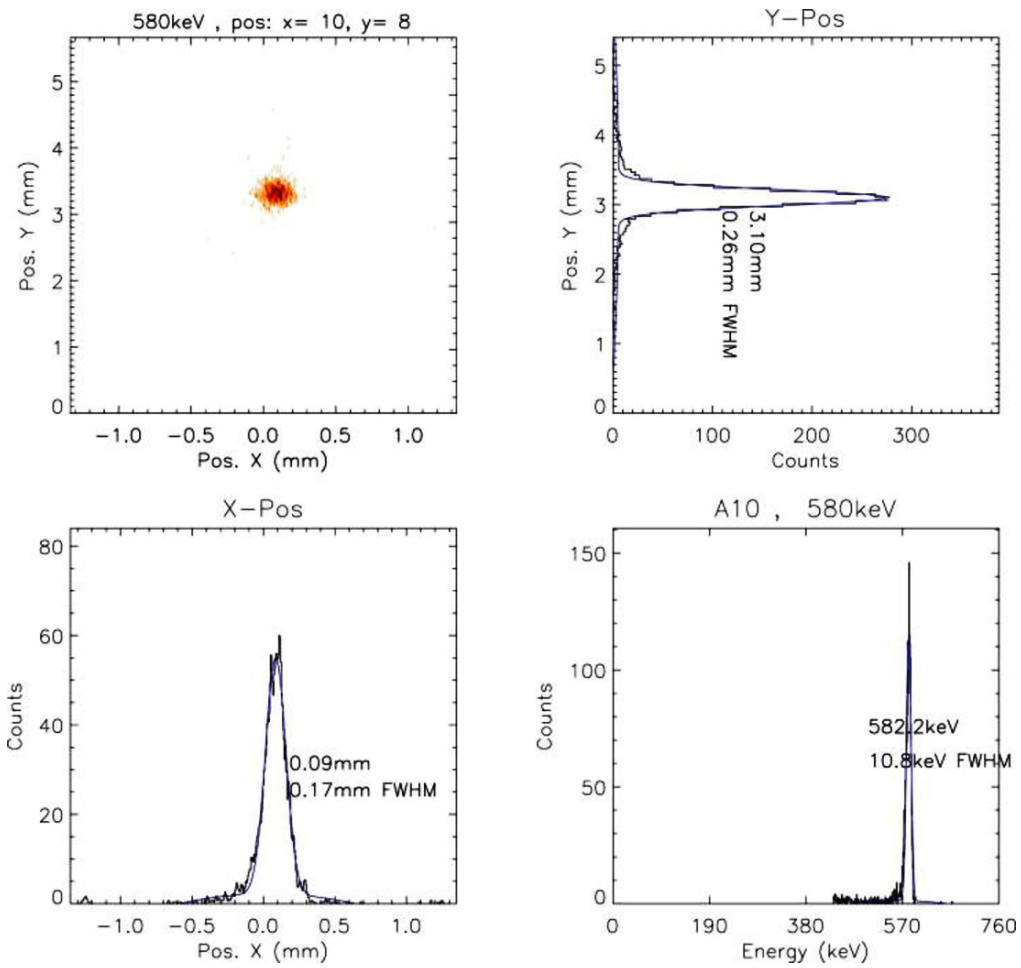

Figure 5.41: *Result for x=10 and y=8 of 2D scans data for 580 keV beam energy.*

	Energy resolution	**Position resolution**		
Beam Energy (keV)	Energy resolution FWHM (keV)	x-direction (μm)	y-direction (μm)	z-direction (μm)
150	1.91	420	380	300
300	4.50	210	240	700
400	5.58	180	210	660
580	7.63	170	260	600

Figure 5.42: *Summary of the measured position resolution in 3D.*

Chapter 6

Conclusions

β-PbO Polycrystalline films

Lead oxide films were grown by the vapor phase starting from metallic lead and oxygen. We were able to obtain films where only orthorhombic phase was formed, whilst in the past polymorphic films were typically reported. Film thickness up to 20 microns was reached up to now. Even if this is enough to efficiently stop x-ray radiation exploited by a large part of med-ical applications, the film thickness should be increased to about 100 microns. The films were oriented along the c axis and showed a few micrometer grain dimension that is compatible with the realization of a pixel structure in the order of 100 μm. Films showed very high resistivity, thanks to the higher energy band gap of orthorhombic phase with respect to tetragonal phase. The good film crystallinity was also demonstrated by an intense PL emission. Both PC and PL spectra showed the presence of a broad deep level band. Films showed a clear increase in current as a consequence of X-ray irradiation with no pile up or memory effects. No transport properties can be extracted from the XBIC measurement confirming the poor transport properties of polycrystalline films as measured by Schottmiller.[21]
Finally the XBIC proved to be a very interesting technique for studying the transport properties of high resistive semiconductor materials. This technique can be further developed in order to obtain more information such as the role of de-trapping in CZT crystals.

β-PbO Nano-Ribbons

Single crystalline nanostructures of β-PbO were grown by vapor phase using the same setup used for films. This crystals are in form of nano-ribbons with an extremely high thick-to-length ratio (10000/1): the width and length are respectively in the range 10÷50 μm and 50÷500 μm and the thickness is typically 50-100 nm. TEM diffraction confirms that these nano-ribbons are single crystals with orthorhombic phase. Single nano-ribbon could be manipulated and put on special substrates and electrically contacted. PL response of single crystal was very similar to those of the film. On the contrary, PC spectra showed a shift in the main response peak in comparison to that of the film. This shift can be explained considering the difference between surface/bulk absorption and recombination in films and in nano-ribbons.
With XBIC technique for the first time the saturation in the x-ray induced current was ob-

served.By fitting the measurements a $\mu\tau$ value of $2 \cdot 10^{-5}\ cm^2/V$ was obtained when all the sample was irradiated. This value can be attributed to electrons considering the band structure of β-PbO. In any case this value is considerably higher than the value found by Schottmiller ($1 \cdot 10^{-9}\, cm^2/V$)[21] and it is much more similar to the value inferred by Keezer ($4 \cdot 10^{-4}\, cm^2/V$) [22].
The single carrier transport properties were measured by shielding the main part of the active channel of the device. In this configuration and changing the polarity of electrodes, two different saturations in the induced currents were observed.
The obtained values of $\mu_e\tau_e$ and $\mu_h\tau_h$ are not fully reliable and the measurement should be repeated under more controlled conditions. In order to measure $\mu_e\tau_e$ and $\mu_h\tau_h$ a very collimated source would be required, such as the one available in a synchrotron facility, where very small X-ray beam size can be achieved.

CZT Detectors

Several ingots grown at IMEM-CNR by Boron Encaplsulated Vertical Brigman technique were tested and material quality was studied. The ingots typically show large single crystal parts and several 1 mm x 1 mm x 5mm detectors could be prepared. Using B2O3 as encapsulant there is no interaction between the ampoule and the ingot during growth and very smooth side surfaces are obtained. As demonstrated by PICTS measurements, this can also reduce the contamination of the material due to the interaction with ampoule and the sealing procedure. A possible drawback of B2O3 is the contamination of B atoms inside the CZT, but the PICTS measurements showed that B atoms are not electrically active and do not affect the transport properties of the material.The transport properties of electrons in CZT grown with EVB technique are good and in agreement with the values reported in literature. In particular value of $\mu_e\tau_e = (1 \div 3) \cdot 10^{-3} cm^2/V$ is normally measured. On the contrary the $\mu_h\tau_h$ for holes is very low and no signal contribution can be recorded in a typical measurement.
As shown in fig.5.11 the spectroscopic response of detectors is very good with ^{241}Am source and a resolution of 6% is normally measured for CZT grown at IMEM-CNR. At higher energy the effect of trapping in the planar detector starts to be dominant and the response of detectors is strongly limited. To overcome this problem, single polarity charge sensing devices must be used if high-energy resolution has to be achieved.

3D CZT Detectors

At IMEM-CNR a new process for 3D detectors fabrication was developed during this work, exploiting commercial material, in the frame of a project leaded by DTU Space and founded by ESA. These detectors represent state of the art devices for 3D photons reconstruction with an extremely high energy resolution. For these high-performance detectors, fabrication process involves several steps and each step was developed in order to achieve the best quality and reproducibility. In order to decrease the surface leakage currents also a new passivation process was developed. This process involves the deposition of 150 nm alumina layer on CZT with PED deposition technique at room temperature.

Thanks to improvements in all fabrication steps high performance detectors were fabricated. The characterization at synchrotron facility in Grenoble showed that high spatial resolution in 3 dimensions can be achieved in these devices. Moreover the energy resolution resulted very high, energy resolution of 1.5% was measured for 600 KeV energy.
The characterization showed also that the spatial uniformity of detector response does not depend on the detector fabrication process but mainly depends on the electrodes configurations used in this drift stripe detectors. In conclusion it is possible to state that at IMEM-CNR institute we have all the facilities and know-how for 3D detectors preparation.
The future work will be to integrate the 3D detector technology with CZT grown at IMEM-CNR in order to test the quality of our material with improved contact geometry. In fact, the developed 3D detectors are single charge detectors and, therefore, a good response of CZT material grown at IMEM-CNR with 3D detector technology is expected.

Future Plans

In the last three years, my work on radiation detection concerned several topics: crystal growth, material characterization, and radiation detectors preparation. In particular, during this time, I developed many skills on PbO and CZT growth and on CZT device preparation. Moreover, in collaboration with Nicola Zambelli, I developed a process for the realization of 3D high performance CZT based detectors. In the world few other research centres have this technology for fabricating such type of detectors. We also realized, during 3D detectors project, that also few companies in the world can make these high performance custom 3D detectors. Therefore, driven by the results obtained in the frame of this project, on January 9 2014 we started, in collaboration with other colleagues of IMEM-CNR, a company for CZT detector realization called Due2Lab s.r.l.. Several companies have already shown their interest in our company and in our CZT detector technology. This represents a personal goal but also a recognition of the quality of my PHD work.

Publications

Some of the results of this work have been published in different papers and conference proceedings as shown in the list of publications at the beginning of the thesis

Bibliography

[1] P.J. Van Heerden, The crystal counter, Dissertation, Utrecht University, (1945)

[2] A. Owens and A. Peacock, Nuclear Instruments and Methods in Physics Research A, 531, (2004)

[3] Radiation Detection and measurement, Glenn F. Knoll, Wiley

[4] wikipedia, http://en.wikipedia.org/wiki/File:Al-gamma-xs.svg

[5] T. Jing et al., IEEE Trans. on Nucl. Sci. 41, 4 (1994)

[6] Martin Nikl, Meas. Sci. Technol. 17, R37 (2006).

[7] S. O. Kasap and J. A. Rowlands, IEE Pmc.-Circuit.y Devices Sy.st. 149, 2 (2002).

[8] Semiconductor Radiation Detectors, Gerhard Lutz, Springer

[9] C.A. Klein, J. Applied Physics 39, 2029 (1968)

[10] E. Kalemci, et al., Nuclear Instruments and Methods in Physics Research Section A: Accelerators, Spectrometers, Detectors and Associated Equipment, 478(3), 527 (2002)

[11] K. Hecht, Zeitschrift für Physik 77.3-4 (1932)

[12] W. Shockley, J. Appl. Phys. 9, 635 (1938)

[13] S. Ramo, Proceed- ings of the I.R.E., 584 (1939)

[14] G. Cavalleri, et al., Nuclear Instruments and Methods 92.1 (1971)

[15] Z. He, Nuclear Instruments and Methods in Physics Research A 463 (2001)

[16] H Barrett et al., Phys. Rev. Lett. 75 (1995)

[17] P.N. Luke, Appl. Phys. Lett. 65 (22), (1994)

[18] P.N. Luke, IEEE Transactions on nuclear science, 42,V. 4, (1995)

[19] S. Del Sordo, et al. Sensors 9.5 (2009)

[20] D. Risold et al., J. Of Phase Equilibria, vol. 19 No. 3, (1998)

[21] J. C. Schottmiller, J. of Appl. Phys. 37(9), 3505 (1966)

[22] R. C. Keezer, et al., J. of Appl. Phys. 39(4), 2062 (1968)

[23] M. Simon, et al., IEEE Trans. on Nucl. Sci., V. 52, N. 5, (2005)

[24] J. R. Clarke et al., Thin Solid Films, 66 , (1980)

[25] R. Hill, Acta Crystallographica, Section C , 41, (1985)

[26] H. J. Terpstra, et al, Physical Review B 52(16), 11690 (1995)

[27] G. Trinquier, et. al, The Journal of Physical Chemistry, 88(26), 6697 (1984)

[28] http://webmineral.com/data/

[29] D. Calestani, et al., J. Crystal Growth 275, E2083 (2005).

[30] D. Calestani, et al. , Chemical Physics Letters 445, 251 (2007).

[31] M. Zha, et al., Nanotechnology 19, 325603 (2008).

[32] H. J. Terpstra, et al., Phys. Rev. B 52, 16 (1995).

[33] Semiconductor opto-electronics, t.s. moss, london butterworths

[34] M. C. Veale, et al., Nuclear Instruments and Methods in Physics Research Section A: Accelerators, Spectrometers, Detectors and Associated Equipment 576.1 (2007)

[35] Watts, B., et al., Journal of Physics: Conference Series. Vol. 186. No. 1. IOP (2009).

[36] Calestani, D., et al., Sensors and Actuators B: Chemical 144.2 (2010)

[37] D. Olega, J. Faurie, S. Sivananthan, P. Raccah, App. Phys. Lett.47(1985).

[38] A.W. Webb, et al., J. Appl. Phys. 61, 2492, (1987).

[39] J.F. Butler, C.L. Lingren, F.P. Doty, IEEE Trans. Nucl. Sci. NS39 (1992).

[40] R. Triboulet and P. Siffert, CdTe and Related Compounds; Part 2, Cristal Growth, Surfaces and Applications, Elsevier (2010)

[41] A. Zappettini, et al., Journal of Crystal Growth, 307, 283 (2007)

[42] M. Zha, et al., Journal of Crystal Growth, 237, 1720 (2002)

[43] A .Zappettini, et al., Journal of Crystal Growth, 307, 283 (2007)

[44] A. M. Mancini et al., Journal of Applied Physics 53, 5785 (1982)

[45] Musa, A., et al. , Journal of Applied Physics 54.6 (1983)

[46] M. Prokesch, C. Szeles, J. Appl. Phys. 100, 014503 (2006)

[47] A. Cavallini, et al., Nuclear Science, IEEE Transactions, V.60 , 4, (2013)

[48] Ayoub, M., et al., Materials Science and Engineering: B 83.1 (2001)

[49] Kuvvetli, Irfan, et al., Radiation Physics and Chemistry 61.3 (2001)

[50] Gostilo, V., et al., Nuclear Science Symposium Conference Record, 2001 IEEE. Vol. 4. IEEE, (2001).

[51] E. Gatti and P. Rehak., Proceedings of 1983 DPF Workshop on Collider Detectors, (1983).

[52] M.A.J. van Pamelen and C. Budtz-Jorgensen. boh. Nucl. Instr. and Meth., 403:390, (1998).

[53] Jung, I., et al., Nuclear Science Symposium Conference Record, IEEE., 1, (2005).

[54] JUNG, I., et al., Optics & Photonics, SPIE 631910 (8), (2006)

[55] Rampino, S., et al., Applied Physics Letters 101.13 (2012)

[56] A. Many, Journal of Physics and Chemistry of Solids, 26.3 (1965).